PEDRO MIGUEL DA SILVA BRAGANÇA

Graduate degree in Biochemistry

Incorporation of Mo in a Rubredoxin-Type Centre of *a de Novo* Designed α_3-DIV-L21C Three Helix Bundle Peptide

Dissertation to obtain a Master Degree in Biochemistry

Supervisor: Doutora Marta S. P. Carepo, Investigadora, Faculdade de Ciências e Tecnologias da Universidade Nova de Lisboa

Co-supervisor: Professor Doutor José J. G. Moura, Professor Catedrático Aposentado, Faculdade de Ciências e Tecnologias da Universidade Nova de Lisboa

Júri:

Presidente: Professora Maria Alice Santos Pereira

Arguente: Professor José Ricardo Ramos Franco Tavares

October, 2019

FACULDADE DE CIÊNCIAS E TECNOLOGIA
UNIVERSIDADE NOVA DE LISBOA

PEDRO MIGUEL DA SILVA BRAGANÇA

Graduate degree in Biochemistry

Incorporation of Mo in a Rubredoxin-Type Centre of *a de Novo* Designed α_3-DIV-L21C Three Helix Bundle Peptide

Dissertation to obtain a Master Degree in Biochemistry

Supervisor: Doutora Marta S. P. Carepo, Investigadora, Faculdade de Ciências e Tecnologias da Universidade Nova de Lisboa

Co-supervisor: Professor Doutor José J. G. Moura, Professor Catedrático Aposentado, Faculdade de Ciências e Tecnologias da Universidade Nova de Lisboa

Júri:

Presidente: Professora Maria Alice Santos Pereira

Arguente: Professor José Ricardo Ramos Franco Tavares

October, 2019

Incorporation of a Mo in a Rubredoxin-Type Centre of *a de Novo* Designed α_3-DIV-L21C Three Helix Bundle Peptide

Copyright © Pedro Miguel da Silva Bragança, Faculdade de Ciências e Tecnologia, Universidade Nova de Lisboa.

A Faculdade de Ciências e Tecnologia e a Universidade Nova de Lisboa têm o direito, perpétuo e sem limites geográficos, de arquivar e publicar esta dissertação através de exemplares impressos reproduzidos em papel ou de forma digital, ou por qualquer outro meio conhecido ou que venha a ser inventado, e de a divulgar através de repositórios científicos e de admitir a sua cópia e distribuição com objetivos educacionais ou de investigação, não comerciais, desde que seja dado crédito ao autor e editor.

Acknowledgments

Um afetuoso agradecimento à Doutora Marta S. P. Carepo por todo o apoio, pela boa-disposição diária, pelos excelentes conselhos e por expandir os meus conhecimentos nas mais diversas áreas.

Um profundo agradecimento ao Professor Doutor José J. G. Moura e Professora Doutora Isabel Moura por me receberem tão amavelmente no seu grupo de investigação e por ampliarem o meu interesse no ramo da química bioinorgânica.

Um agradecimento à Doutora Cristina M. Cordas por aprofundar os meus conhecimentos na área da eletroquímica e pela sua perseverança mesmo quando o misterioso ruído de final de tarde visitava.

Um agradecimento à Doutora Sofia Pauleta, ao Doutor Alejandro Samhan-Arias, à Doutora Luísa Maia e à Doutora Maria João Nunes pela carinhosa receção no grupo e permanente boa-disposição.

Um agradecimento a todos os restantes colegas de grupo pela partilha de ideias e pelos momentos de descontração.

Un ringraziamento a Maddalena Elia per l'ottimo lavoro svolto in precedenza nel gruppo.

Quero agradecer à minha família por todo o apoio ao longo destes 5 anos e por me proporcionar esta oportunidade para expandir os minhas capacidades.

Quero agradecer a todos os meus amigos (VdB) pelo suporte e companheirismo ao longo destes anos. Alguns foram mais difíceis, outros menos e outros mais ou menos.

Um agradecimento especial à Asiyah Esmail pelo amor, pelo carinho, pelo suporte e pelo apoio desde que nos conhecemos. Obrigado por me aturares quando não estou nos meus dias (são quase todos).

Um agradecimento à Faculdade de Ciência e Tecnologia da Universidade Nova de Lisboa.

Um agradecimento à FCT/MCTES pelo financiamento (UID/QUI/50006/2019).

Abstract

Approximately one-third of all proteins and enzymes require one or more metal atoms to perform their catalytic functions. Presently, the rational design and engineer of small, simple and stable peptides scaffolds to mimic catalytic metal-centres of complex proteins is an important goal in the area of protein design and search for centres with environmental, biotechnological and basic research impact. In this work, *a de novo* designed α_3DIV-L21C peptide that possesses a rubredoxin-type centre as the metal-binding site was used to incorporate a Mo atom to mimic, specifically, the tetrathiolate environment found in the active-site of molybdenum-*bis* pyranopterin guanosine dinucleotide-containing enzyme (Mo-*bis* PGD). The Mo-α_3DIV-L21C peptide reconstitution was acceded by ICP-AES to optimize the reconstitution conditions tested and a 1:1 peptide/metal ratio was obtained using a 1:10 peptide/metal ratio for reconstitution. Using UV-vis spectroscopy, the emergence of two broad bands, with a maximum absorption between 310-330 nm (ε_{320nm} = 7400 $M^{-1}.cm^{-1}$) and 460-475 nm (ε_{470nm} = 2000 $M^{-1}.cm^{-1}$), confirm the metal incorporation within the tetracysteinyl environment. Circular dichroism (CD) studies, in the visible region, further confirmed the metal incorporation through the appearance of a positive band with a maximum at 394 nm. Furthermore, secondary structure profile and tertiary structure fingerprint were examined, under TCEP-induced reducing and non-reducing conditions, as well as thermal stability studies in both far-UV and visible regions. Differential Scanning Calorimetry (DSC) was used to perform a thermal denaturation analysis and define thermodynamic parameters for Mo-α_3DIVL21C peptide. Thermogram fitted well to a reversible monomeric two-state model, with a T_m value of 66 ºC, a ΔH_{cal} value of 846.4 $kJ.mol^{-1}$ and a ΔH_{vH} value of 920.03 $kJ.mol^{-1}$. Preliminary electrochemical results through the use of cyclic voltammetry (in a thin-layer regime) suggest an initial oxidation state of Mo(VI), within the metal-binding site, and formal potential ($E^{0'}$) of -406 mV vs. NHE with a capability to undergo one-electron transfer process (Mo(VI)/Mo(V)). Moreover, reducing tests attained with different reducing agents and followed by spectroscopy seems in agreement with this assumption.

Keywords: *a de novo* protein design, molybdenum, DMSOR family, rubredoxin

Resumo

Aproximadamente um terço de todas as proteínas e enzimas requerem um ou mais átomos metálicos para efetuarem as suas funções catalíticas. Atualmente, o *design* racional e construção de esqueletos peptídicos pequenos, simples e estáveis para mimetizarem centros-metálicos catalíticos de proteínas complexas é uma meta importante na área de *design* de proteínas e na descoberta de centros com importância ambiental, biotecnológica e académica. Neste trabalho, o péptido a de novo designed α_3DIV-L21C que possuí um centro do tipo rubredoxina, como local de coordenação de metais, foi usado para incorporar um átomo de Mo para mimetizar, especificamente, o ambiente tetratiolado encontrado no centro-ativo das enzimas que contêm o cofator molibdénio-*bis* piranopterino (Mo-*bis* PGD). A confirmação da reconstituição do péptido Mo-α_3DIV-L21C foi efetuada por ICP-AES e o 1:1 rácio de péptido/metal foi obtido, utilizando um rácio de 1:10 de péptido/metal para a reconstituição. Utilizando espectroscopia de UV-vis, a emersão de duas bandas largas, com um máximo de absorção entre 310-330 nm (ε_{320nm} = 7400 $M^{-1}.cm^{-1}$) e 460-475 nm (ε_{470nm} = 2000 $M^{-1}.cm^{-1}$), confirma a incorporação do metal no ambiente tetracisteinílico. Estudos de dicroísmo circular (CD), na região do visível, confirmam a incorporação do metal através do aparecimento de uma banda positiva com um máximo a 394 nm. Adicionalmente, o perfil da estrutura secundária e o "impressão digital" da estrutura terciária foram examinados, sob condições redutoras induzidas por TCEP e não redutoras, bem como estudos de estabilidade térmica em ambas as regiões do far-UV e do visível. Foi utilizada calorimetria de varrimento diferencial (DSC) para efetuar uma análise de desnaturação térmica e definir parâmetros termodinâmicos para o péptido Mo-α_3DIVL21C. Os termogramas ajustaram devidamente a um modelo monomérico reversível de dois-estados, com um valor de T_m de 66 ºC, um valor de ΔH_{cal} de 846.4 $kJ.mol^{-1}$ e um valor de ΔH_{vH} de 920.03 $kJ.mol^{-1}$. Estudo eletroquímicos preliminares através de voltametria cíclica (em regime de camada fina) sugerem um estado de oxidação inicial de Mo(VI), no sítio de coordenação metálico, e um potencial formal ($E^{0'}$) de -406 mV vs. NHE com a possibilidade da transferência de um eletrão Mo(VI)/Mo(V). Adicionalmente, testes de redução realizados com diferentes agentes redutores e seguidos por espetroscopia parecem estar de acordo com esta suposição.

Palavras-chave: a de novo *design* de proteínas, molibdénio, família DMSOR, rubredoxina

Preamble

The 2019 Periodic Table of the Chemical Elements contains 118 elements organized and related by their intrinsic physical-chemical properties to their neighbours (rows and columns). Of these 118 elements, slightly more than 30 are believed to have a biological role in all forms of life on Earth **(Fig.1)**, from eukaryotic organisms to prokaryotic organisms, but only 12 of these 30 elements occur in all known kingdoms of life [1,2]. Of all the elements currently used in biological systems, transition metals may have been the fundamental elements that boosted the evolution of life and differentiation to superior organisms [3,4]. The introduction of metals in proteins and enzymes, in addition to the geological role in the ecosystems, connect the environment and life, creating an unbreakable link between inorganic and biologic chemistry [5–7]. This relationship was so strictly necessary that it has been estimated that one-half to one-third of the functions and structural features require the presence of a metal ion [8]. The metal active-sites allows the protein to perform several of the most complex and essential reactions in nature and can be divided into four basic functional types, (I) structural, (II) storage, (III) electron transfer processes and (IV) catalytic [9]. The cooperation between functional complexity with regulatory roles, such as sensors and on regulatory processes, placed some metalloenzymes as mediators of essential biological processes, such as cellular respiration, photosynthesis and nitrogen fixation. Due to these abilities, the reproducibility and mimicking of their functions are one of the main goals in bioinorganic chemistry. In the present work, our attention will be oriented to the only biological-active metal from the second transition row, the molybdenum atom.

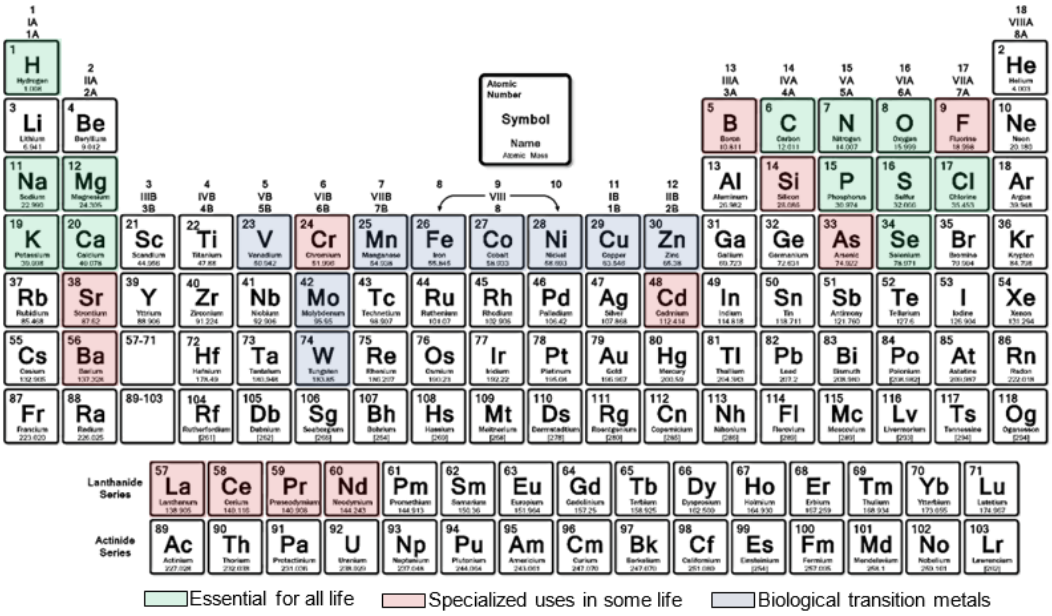

Figure 0.1. Chemical elements used by living organisms in biological processes. Edited from [1].

Table of Contents

List of Figures

List of Tables

List of abbreviations

BSA	Bovine Serum Albumin
CD	Circular Dichroism spectroscopy
CE	Counter-Electrode
CV	Cyclic Voltammetry
D. gigas	*Desulfovibrio gigas*
DMF	N, N-dimethylformamide compound
DMSOR	Dimethylsulfoxide Reductase family
DPV	Differential Pulse Voltammetry
DSC	Differential Scanning Calorimetry
DTT	Dithiothreitol compound
$E^{0'}$	Formal potential
E_{oc}	Open circuit potential
E_{pa}	Anodic peak potential
E_{pc}	Cathodic peak potential
EPR	Electron Paramagnetic Resonance spectroscopy
ET	Electron Transfer rate
GPES	General Purpose Electrochemical System
GMQE	Global Model Quality Estimation
ICP-AES	Inductively Coupled Plasma Atomic Emission spectroscopy
I_{pa}	Current intensity
MCDv	Molybdopterin Cytosine Dinucleotide variant
MCD	Magnetic Circular Dichroism spectroscopy
MGD	Molybdopterin Guanosine Dinucleotide variant
Mo-*bis* PGD	Molybdenum-*bis* Pyranopterin Guanosine Dinucleotide
MorP	Molybdenum response Protein
MPT	Molybdopterin moiety
NHE	Normal Hydrogen Electrode

NMR	Nuclear Magnetic Resonance spectroscopy
ORP	Orange Protein
PB	Poisson-Boltzmann
PDB	Protein Data Bank
PG	Pyrolytic Graphite
QMEAN	Qualitative Model Energy ANalysis
Rd	Rubredoxin
RE	Reference Electrode
RR	Resonance Raman spectroscopy
SCE	Saturated Calomel Electrode
SO	Sulphite Oxidase family
SRB	Sulphate-Reducing Bacteria
SWV	Square-Wave Voltammetry
TCEP	Tris(2-carboxyethyl)phosphine compound
TFET	2,2,2-tri-fluoroethanethiol compound
TLCV	Thin Layer Cyclic Voltammetry
T_m	Melting temperature
TTM	Tetrathiomolybdate compound
UV-vis	Ultraviolet-Visible spectroscopy
WE	Working Electrode
XO	Xanthine Oxidase family
ΔCp	Change in heat capacity
ΔH	Enthalpy of folding
ΔH_{cal}	Calorimetric enthalpy
ΔH_{VH}	Van't Hoff enthalpy
ΔS	Change in entropy

1

Chapter 1. Introduction

1. Rational Protein Design: Artificial enzymes

Over the past 30 years, the field of protein design has been increasing significantly in the areas of fundamental research (biochemistry and biotechnology), of clinical applications and applied (industrial) areas such as in energy production and production of added value products [10,11]. This field comprehends several techniques in which new or existing proteins are enhanced or novel biological functions are created (artificial enzymes [12–14]), and an important spin-off is the understanding of protein structure-function relationship [15]. Nature, with the help of evolution and millions of years of trial and error, has been in the vanguard of this field, creating new structural detailed scaffolds with high efficiency and selectivity.

Protein engineering has a multitude of applications and can resolve current underlying problems, such as the structure and folding prediction to achieve desired protein functions. Such systems are an important tool to understand the fundamental rules that govern the structure-function relationship in proteins. Nevertheless, the creation of unusual structures with novel specificities and proprieties appear to encounter a prevailing problem in current structure prediction studies, the “protein folding problem” [16]. The protein folding is a complex process that involves the transformation of the information encoded by the primary sequence of a protein in a functional and stable tertiary structure. To master this folding process, additional intrinsic thermodynamic and kinetic information are required.

The thermodynamic and kinetic parameters play important roles in the creation of a stable protein scaffold. These parameters have to balance the unfavourable entropy created by the folding process and the favourable enthalpy of the system. Furthermore, the fundamental interactions, such as hydrophobic, electrostatic, Van der Waals and hydrogen bond interactions also determine the stability of the protein structure. Each interaction has particular proprieties that are exploited in order to build a stable protein construct, like the building of salt bridges by

electrostatic interactions, generation of hydrogen bonds to create secondary structures and the use of hydrophobic interactions as a driving force for folding processes.

Additionally, the incorporation of a metal-binding complicates the strategies of protein design. In some reported cases, the metal ion is responsible for the folding process and it is the major force to overcome the unfavourable entropy. Nonetheless, other requirements such as ligand recognition, metal specificity and, ultimately, substrate specificity, impacts this folding process. Even though creating functional designed metalloprotein systems is a difficult process, considering the biological essential roles that some of the native metalloenzymes have in Nature, this is one of the most attractive areas in the field of protein design. [17,18]

Metalloproteins design aims to create efficient catalysts that perform biological functions with the same selectivity and high efficiency under mild conditions. Besides, the construction of novel metal-binding sites in designed or native scaffolds can unravel the structural and catalytic roles imposed by the metal ions [19]. Moreover, intrinsic chemical proprieties of metals, such as magnetic proprieties imposed by different redox states, makes the metal active-sites the perfect target for protein design, since each metal-ligand interaction and each metal redox state have specific spectroscopic features that can be followed by classical spectroscopic techniques [20]. Furthermore, the biological functions of metalloenzymes can be divided into three types: structural, catalytic and electron transfer processes [9]. Each one of these types has been extensively reviewed over the years. [21–23]

Rational protein (metalloprotein) design of artificial enzymes can be addressed with two approaches: the protein redesign, by the use of native proteins templates, and *a de novo* protein design, by the creation of peptide templates from scratch [24]. We can consider these two approaches by which we can understand how a certain structure, at which is related a specific function, can influence the performance of a protein. The classical top-down approach exploits any kind of perturbation (e.g. site direct mutagenesis) in an existing scaffold to determine their contribution to the protein's functions, but the bottom-up approach or rational protein design [24] uses specific structural features and proprieties that are integrated or to an existing system (redesign) or a construct built up from "scratch" (*a de novo* design). Both of these latter methods are important from a coordination and biochemistry point-of-view and for the mimicking of crucial metalloenzymes [24]. In the next sections, we will explore in-depth these two approaches.

1.1. Protein Redesign: "native" proteins templates

Data from a structural classification method reveals that only 1,200 different scaffolds are used as structural domains in more than 38,000 protein crystal structures deposited in Protein Data Bank (PDB). This data suggests that Nature, with a limited number of scaffolds, have achieved highly functional protein variability [25]. Subsequently, over years of evolution, each protein active-site was tuned to be unique, selective and specific to a certain biological function. [18]

Protein redesign applies this same concept used by Nature, through the design and engineer of new metal-binding sites into existing native proteins, instead of creating novel scaffolds. This strategy aims to improve or generate novel properties in well-known proteins (e.g. in rubredoxins) to achieve new activities, modify stereoselectivities or improve substrate specificity. Such modifications help us clarify the structure-function relationship in native proteins and allow us to construct new proteins for biomedical and pharmaceutical applications.

Specifically, the redesign of metalloenzymes coincides with the redesign of the metal active-site inside a native protein scaffold. Such natural scaffolds make the engineering of metal-binding sites more achievable since they are more stable and more resistant to chemical modifications. Moreover, native proteins normally can catalyse more than one chemical transformation in their single active-site, which allows a wider range of chemical transformations to occur within existing scaffolds. In addition, the efficiency of the catalytic activity in some metalloenzymes is not optimal, which leaves some chemical freedom to achieve improved activities and/or specificities. [24]

Metalloprotein redesign strategy seems to be the most effective approach since native metalloproteins already have a specific metal-binding site and can adapt easily to environmental changes. The redesign also allows incorporation of only those features that are thought to influence the reactivity and can shed light on the most relevant residues that affect the reaction catalysed by the enzyme. Furthermore, by applying a minimal number of modifications, the fundamental requirements for a certain function can be studied without the stabilities and symmetries problems associated with *a de novo* design of scaffolds. [22]

Usually, such new functional features can be attained by playing with the metal ions chemistry. Such modifications can be achieved by changing exclusively the metal ion in the metal-binding site or by altering the type and/or the number of ligand coordination arrangements (amino acid mutations). Nevertheless, in the present work, we will focus solely on the metal-substitution approach, which exploits the metal-switching affinity, or metal-binding promiscuity, of some proteins for the construction of artificial metalloenzymes. [26]

The metal-substitution approach exploits the catalytic promiscuity of some enzymes [27]. This modifications in the metal binding specificity can lead to the creation of an artificial metalloenzyme with novel proprieties. To perform this strategy two experimental steps are crucial: the extraction of the “native” metal to obtain an apo-protein form, and the reconstitution of this apo-form with the incorporation of the desired new metal [28]. The incorporation of distinct metal atoms within the same metal-binding site offers the opportunity to compare different metal active-sites within the same protein scaffold. [20]

1.1.1. Rubredoxins: “native” protein template for Protein Redesign

One outstanding model metalloprotein used for protein redesign is Rubredoxin (Rd). This simple iron-sulphur bacterial protein (≈6 kDa) participates in electron transfer processes in biological systems and contains a single Fe ion coordinated by four cysteinate sulphurs {Fe(S-Cys)$_4$}, arranged in a distorted tetrahedral environment. The distinct mononuclear tetrahedral tetrathiolate metal-binding site can cycle between the high spin Fe(II) and high spin Fe(III) oxidation states. [29]

Structurally, Rd exhibits a specific “rubredoxin-like” fold that represents a superfamily by themselves. Its polypeptide chain is composed of two or three helical turns and a comparatively short three-stranded antiparallel β-sheet. The Fe ion is connected by two cysteines provided by the N-terminal, whereas the last two cysteines are in a hydrogen-bonded turn in the C-terminus. Is the protein-specific consensus sequence that recognizes the metal ion and causes the folding of the protein in a particular conformation, originating a –CX_2C–Xn–CX_2C– motif. [30]

Rubredoxins exhibited reduction potentials close to 0 Volts, with a spread of ≈ 100 mV for both negative and positive sides. This discrepancy is influenced by hydrogen bonding interactions between cysteine sulphurs and vicinal amide protons [31,32]. Due to this particular chemistry, Rd drives a great interest in metal substitutions since provides a cysteinyl potential coordination environment, similar to others sulphur-rich environments such as zinc enzymes [33,34], bacterial [NiFe] hydrogenase [35,36], Cu-chaperones [37,38], cupredoxins [39,40] and molybdenum-containing proteins [41].

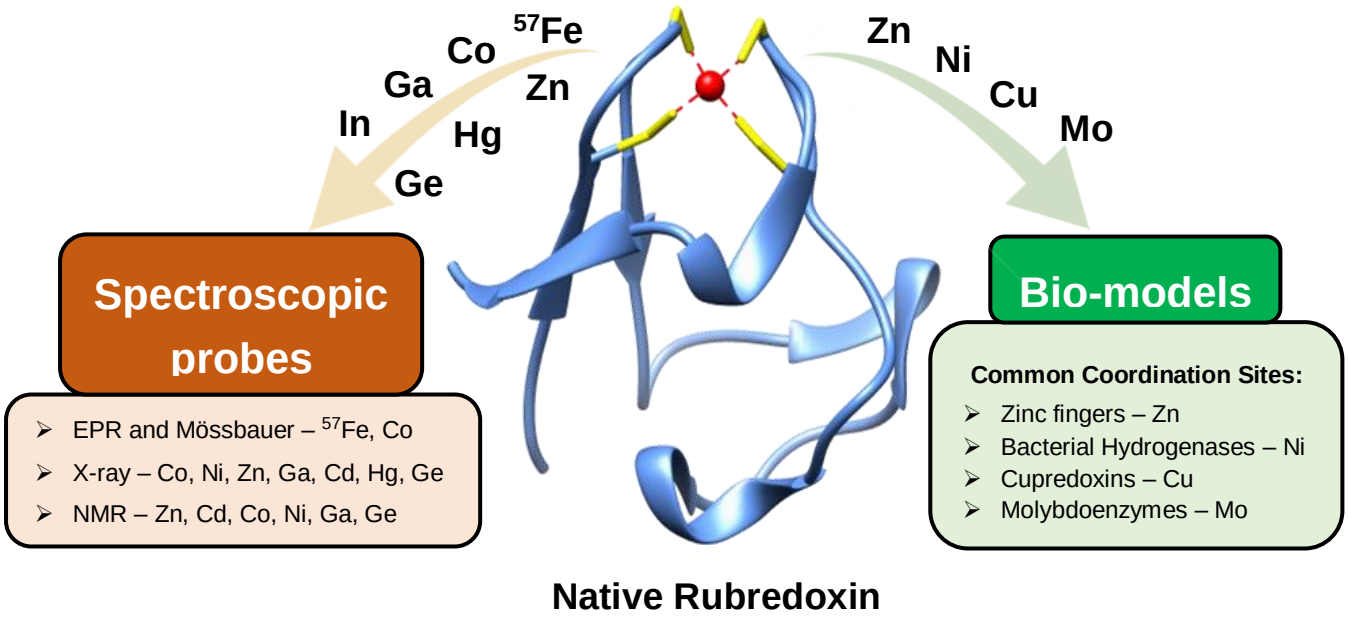

Figure 1.1. Protein redesign using metal-substituted derivatives of rubredoxin.

The Rd derivatives are an important tool to elucidate structural and functional aspects of metal sites involving coordination spheres rich in sulphur atoms. The metal-substituted Rds can be used as structural probes to elucidate the structure-function relationship and as bio-models to model complex active-sites of native enzymes. The tetracysteinyl metal coordination site of Rds has the ability to incorporate a wide variety of metal ions, and until now several metal-substituted Rds containing ^{57}Fe(II) [42], Co(II) [43], Ni(II) [44,45], Cu(I) [46,47], Zn(II) [48,49], Cd(II) [43], Hg(II) [43], Ga(III) [43], In(III) [50], Ge(IV) [51] and Mo(VI, V, IV) [52] have been prepared and characterized. **(Fig.1.1)**

1.1.1.1. Mo-substituted Rd: a model for Mo-containing proteins

Mo-substituted rubredoxin (Mo-Rd) from the species *Desulfovibrio gigas* (*D. gigas*) has been successfully obtained, through a dialysis process in acidic conditions [52]. The aim was to mimic the mononuclear molybdenum-*bis* pyranopterin centre encountered in the DMSOR family, by coordination of the Mo atom with the four cysteinate sulphurs and by exogenous ligands, such as oxygen and sulphur atom, forming a Mo(VI)-(S-Cys)$_4$(=O)(X) complex (X = –OH or –SR).

UV-vis spectral characterization confirms the incorporation of the molybdenum atom in the tetracysteinyl metal-binding site of rubredoxin. Besides a maximum absorption band at 278 nm (ε = 17.77 mM^{-1}.cm^{-1}), the two unresolved shoulders at 314 and 450 nm (ε = 8.01 and 1.02 mM^{-1}.cm^{-1}, respectively) can be assigned to molybdenum-thiolate charge-transfer bands. Raman spectroscopy further revealed Mo-S bending and stretching vibrational modes, and suggest that the Mo-centre entails in a Mo=O(=O…H–protein) or Mo=O(–OH) type of coordination sphere, similar to the one observed in the oxidized form of arsenite oxidase [53].

EPR studies show that the Mo-centre stabilizes the metal atom in a +6 oxidation state and can be reduced to Mo(IV) via Mo(V) by a reducing agent, like sodium dithionite ($E^{0'}$ = -660 mV vs. NHE). Additional spectroscopic studies show that dithiothreitol (DTT) cannot reduce the molybdenum atom ($E^{0'}$ = -330 mV vs. NHE), but can coordinate with the metal-centre as an exogenous thiol ligand. [52]

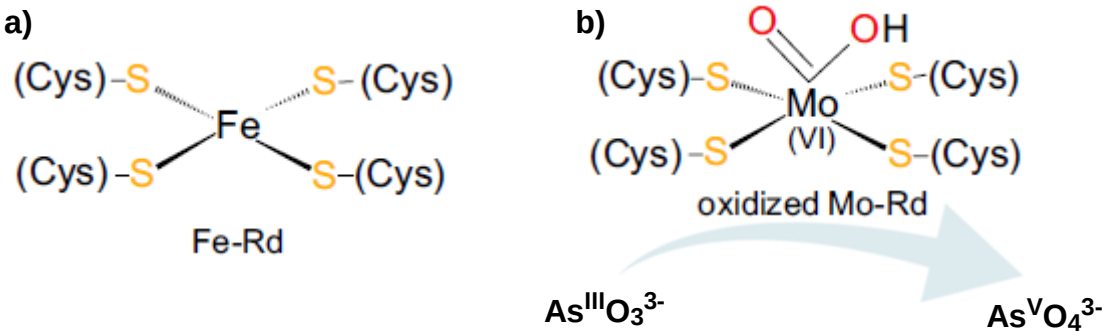

Figure 1.2. Comparison of the metal-binding site coordination geometry in (a) native rubredoxin and (b) molybdenum-substituted Rd. Edited from [52].

Furthermore, activity studies suggest the ability to catalyse oxo transfer reactions similar to the native mononuclear molybdenum-containing enzymes. Such reaction involves oxidation of arsenite ($As^{III}O_3^{3-}$) to arsenate ($As^{V}O_4^{3-}$), like as seen in the native arsenite oxidase [52]. This study demonstrates that the incorporation of a molybdenum atom into an Rd scaffold can reproduce a system with the same coordination sphere chemistry, spectroscopic features and catalytical functions that in native Mo-containing enzymes. Is safe to conclude that this redesign Rd is a structural and functional analogue to the Mo-*bis* PGD family (DMSOR family). **(Fig.1.2)**

1.1.1.2. Molybdenum in Biology

When we outlook the elements that are essential for life on Earth, molybdenum is hardly ever considered. Nevertheless, its biological history is almost as old as life on Earth.

Molybdenum is a transition metal from the 6th group and the second transition series of the Periodic Table of Elements. Its electronic configuration, [Kr] $4d^5$ $5s^1$, provide rich and versatile redox chemistry with several valence states, from +II to +VI. Nonetheless, under physiological conditions, the oxidation states just vary between +IV a +VI, with exception of nitrogenase enzyme that holds a +III oxidation state. With this oxidation states versatility, Mo-containing enzymes can catalyse either one-electron, Mo(VI) ↔ Mo(V); Mo(V) ↔ Mo(IV), or two-electron, Mo(VI) ↔ Mo(IV), oxidation-reduction reactions. [54]

Although it is an essential trace metal that is present in all domains of life, from archaea, bacteria and eukarya [55,56], is biological demand is low when compared with other essential biological trace metals, such as Fe and Cu [57]. Despite this, Mo continues to be the building block of several cofactors used by more than 60 enzymes present in the nitrogen, carbon and sulphur biogeochemical cycles [58,59]. As a result of the versatility of Mo first coordination sphere, the formation of oxides and sulphides highly enhance the Mo involvement in biological processes.

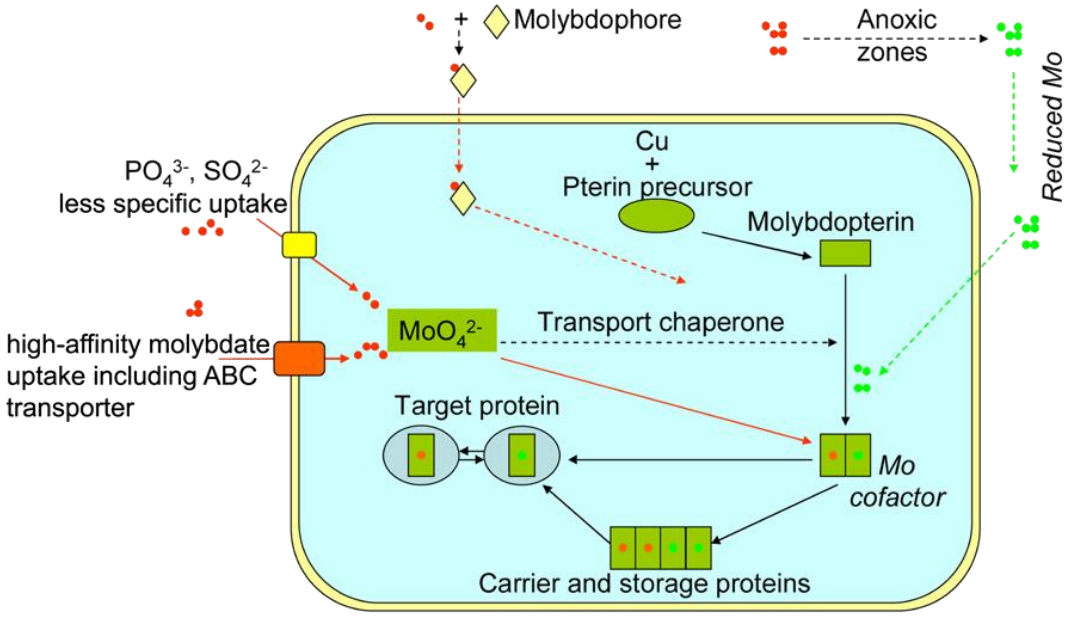

Figure 1.3. Schematic representation of Mo uptake and storage in prokaryotes (dashed lines) and in eukaryotes (solid lines). The red dots are the oxidized form and the green dots are the reduced form of molybdenum. Retrieved from **[57].**

Furthermore, the specific “atom exchanger” ability, in particular on “oxygen atom transfer“, present in molybdenum complexes is balanced by the tendency of Mo to bind oxo groups and its capacity to simply lose a single oxygen atom. Due to this adaptable chemistry, many enzymes took advantage and start to catalyse several different atom-transfer reactions, like oxygen, proton and sulphur atom insertion and abstraction redox reactions, or even non-redox hydration reactions. [60,61]

Since the molybdenum atom has such rich chemistry, its intracellular concentration has to be highly regulated by uptake systems, to protect it from the cell’s oxidising environment and avoid unwanted atom-transfer and electron-transfer reactions [62]. Such regulation is made by the synthesis of specific cofactors that are carried by transport proteins to be inserted in apo-enzymes, generating a mature and functional metalloenzyme **(Fig.1.3)**. The Mo intracellular transport in prokaryotes is performed by a high-affinity molybdate transporter from the ABC family (ModA, ModB and ModC) [63]. In contrast, the molybdate uptake systems in eukaryotes are still being discovered [64]. In anoxic conditions, due to the extremely low oxygen concentration, the intracellular molybdate anion (MoO_4^{2-}), in sulphate-reducing bacteria, is converted to tetrathiomolybdate (MoS_4^{2-}) by oxygen-sulphur exchange.[65]

1.1.1.3. Molybdenum-containing Proteins

Molybdoproteins are proteins that harbour a molybdenum atom in their active-site. This class contains, until now, more than 60 enzymes that can perform a panoply of reactions, extending from the oxygen-, proton- and sulphur-transfer redox reactions, to non-redox hydration reactions. The Mo active-site can perform one or two-electron oxidation and reduction reactions, so the molybdenum atom can cycle between Mo(VI), Mo(V) and Mo(IV) oxidation states. The ability to change the oxidation state allows this class of metalloproteins to catalyse several metabolic reactions in the carbon, nitrogen and sulphur biogeochemical cycles. [66,67]

The Mo-containing proteins can be distinguished in two types depending on the interaction between the cofactor and the metal ion. The first typology is found when the Mo atom is in the enzyme’s active-site as a mononuclear form, coordinated by one or two pyranopterin cofactor molecules, and the second is found in unique heteronuclear cofactors present in the Nitrogenase enzyme [68,69], the orange protein (ORP) [70,71] and the molybdenum response protein (MorP) [72]. In the first typology, the Mo-dependent enzymes can be classified into three large families: xanthine oxidase (XO), sulphite oxidase (SO) and dimethylsulfoxide reductase (DMSOR) families, depending on the number of pyranopterin cofactors and type of additional ligands (oxygen, sulphur and selenium) are coordinated with the Mo centre [41,73]. **(Fig.1.4)**

In these three mononuclear families, one Mo atom is coordinated with one or two pyranopterin cofactor molecules, through the *cis*-dithiolene (–S–C=C–S–) group, to create molybdopterin (MPT) moiety. Additionally, to increase the variability, addition of a second nucleotide after Moco

formation (Mo-MPT), such as cytosine or guanine, to the Mo-MPT structure led to the development of MCD (molybdopterin cytosine dinucleotide) and MGD (molybdopterin guanosine dinucleotide) variants. [74] **(Fig.1.5)**

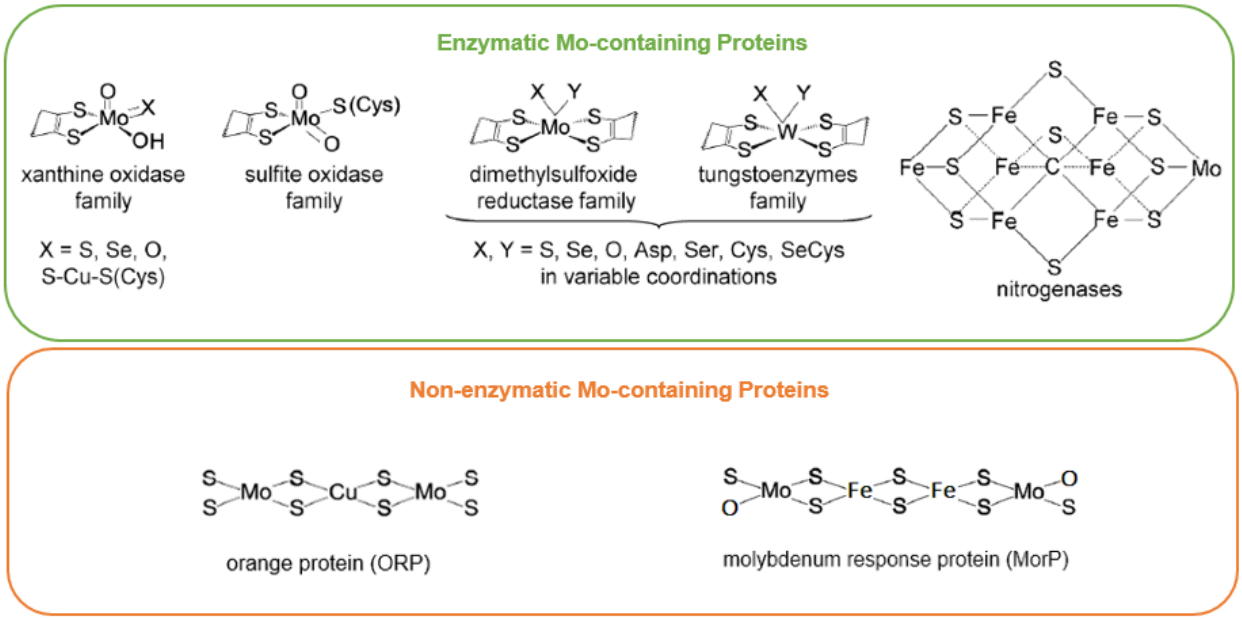

Figure 1.4. Active-site structure of the enzymatic molybdenum-containing proteins and the non-enzymatic proteins. Only the *cis*-dithiolene group of the pyranopterin cofactor, in the XO, SO and DMSOR families, is represented. Edited from [41].

The pterin cofactor not only affects the structural arrangement of the metal, by enabling a correct position of Mo in the active-site but also controls the redox activity of the metal centre. Several studies have suggested that the catalytic ability is shaped by "environment" of the metal first and second coordination spheres, and so on by the pterin cofactor. This cofactor acts like a "wire" that conduct the electrons to and from the molybdenum atom, consequently facilitating the intramolecular electron transfer processes. Furthermore, to tune the metal oxidation state, each enzyme holds a binding pocket that controls the pyranopterin cofactor conformation and selectively controls the pterin structural isoforms. [75–77]

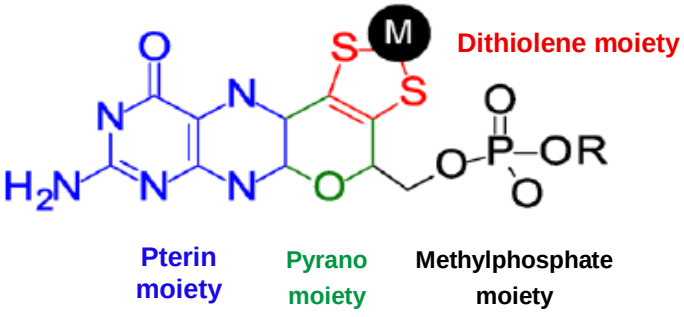

Figure 1.5. Moieties in the molybdopyranopterin cofactor. Edited from [41].

Moreover, the metal reactivity is also influenced by the other atoms (O, S and Se) in the metal coordination sphere. The modulation of the reduction potential of the Mo centre is a consequence of changing the energy levels of the metal ground state d_{xy} orbital [78–80]. The ligand-coordination geometry is imposed by the polypeptide chain to produce an entatic state able to stabilize and facilitate the oxo- and sulphur-groups association and/or dissociation. This influence is observed when we compared a Mo atom coordinated with two pyranopterin cofactors (Mo-containing enzyme) to a synthetic model compound. The first displays a trigonal prismatic coordination geometry and the latter an octahedral geometry. [81,82]

In this work, we are mainly interested in the tetrathiolate environment in the DMSOR family since the Mo atom is coordinated by two pyranopterin guanosine dinucleotide (also named Mo-*bis* PGD enzymes) (**Fig.1.6)**. This family have more structural and functional variability among the three large families. The active-site holds a molybdenum atom coordinated with four sulphurs in a trigonal prismatic geometry ([Mo(VI)O(MPT)$_2$(X)], with additional ligands (Y and X groups), such as terminal oxygen, sulphur and selenium atoms, and/or the O and S atoms from Asp, Ser, Cys and SeCys residues. [41,83]

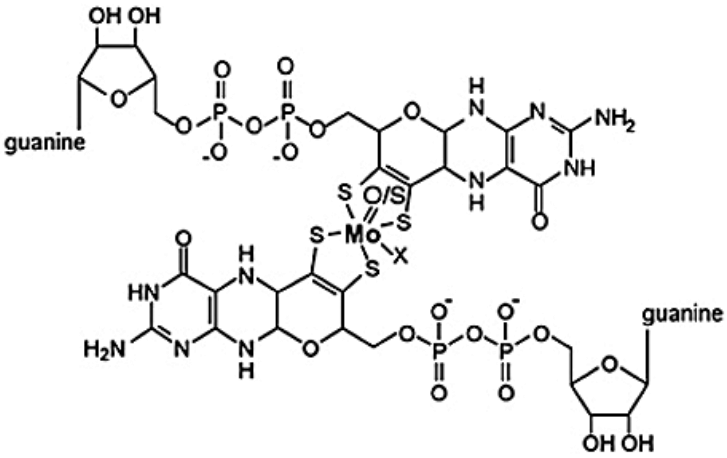

Figure 1.6. Complete structure of the active-site of the DMSOR or Mo-*bis* pyranopterin guanosine dinucleotide (PGD) family. Retrieved from **[67].**

The high biological-variability of the DMSOR family probably derives from the replacing of the oxygens with sulphur atoms that, ultimately, increase the reduction potential. Additionally, the electron transfer rate (ET) and the metal-dithiolene fold-angle also increases. The interaction between the metal in-plane and the sulphur-π orbitals are stabilized by large fold-angles and this effect is important in the regeneration of the Mo active-site during catalysis and for electron transfer processes.[84,85]

1.1.1.4. Mo-heteronuclear non-enzymatic centres

Heteronuclear centres in Mo-containing proteins are unusual. These centres are characterised by the coordination of a molybdenum atom with one or more different metals in the active-site, bridge by sulphur atoms. The two heteronuclear centres recognized in the non-enzymatic Mo-containing proteins are the [$S_2MoS_2CuS_2MoS_2$] cluster in the Orange protein [70,71] and the most recently discovered molybdenum response associated protein (MorP), in *Desulfovibrio alaskensis*, that contains a novel [MoS_2-[Fe_2-S_2]-S_2-Mo] heterometallic cluster [72].

The biosynthesis of these heteronuclear clusters is a challenge because of the different coordination geometries that the molybdenum atom can acquire and the lack of tetrathiomolybdate complexes (MoS_4^{2-}) that are aqueous-soluble and stable. Although such synthesis is challenging, several Mo-containing heteronuclear clusters were successfully synthesized, using the tetrathiomolybdate (TTM) compound, by protein-assisted syntheses, like the heterometallic cluster in the Orange Protein (ORP) [86].

The Orange Protein is a small monomeric protein of ≈12 kDa, of currently unknown physiological function, isolated from sulphate-reducing bacteria (SRB). The ORP harbours a unique molybdenum-cooper heterometallic centre in a linear mixed-metal sulphide cluster – [$S_2MoS_2CuS_2MoS_2$]. This cluster is non-covalently bound to the protein scaffold, but it is stabilized by hydrophobic and electrostatic interactions. [86,87]

In the literature is reported the Mo-Cu cluster reconstitution, for both *D. gigas* apo-ORP and *D. alaskensis G20* apo-ORPs, by protein metal cluster-assisted synthesis using the tetrathiomolybdate compound as the synthetic precursor. The formation of the Mo-Cu cluster was achieved by reacting this extremely redox-active synthetic compound (TTM) with copper chloride in the presence of the apo-protein. TTM and copper chloride are able to react in the absence of protein generating several polynuclear clusters in which one Mo atom is bound to several Cu ions. In the presence of apo-ORP and with 2Mo:1Cu metal stoichiometry it is possible to synthesize a Mo-Cu cluster similar to the one discovered in the ORP. [86,87]

Furthermore, the protein-assisted synthesis of novel heterometallic derivatives in which the molybdenum-sulphur cluster is coordinated in an S_2MoS_2−M−S_2MoS_2 system (M = Fe, Co, Ni or Cd), is also described in the literature. These syntheses were promoted by the Orange Protein using the TTM compound as a synthetic precursor. [88]

The relevance for synthesizing these sulphur-coordinated transition-metal complexes emerge due to their rich redox chemistry that is exhaustively explored by nature and in the industry. Such successful syntheses only were achieved due to the use of tetrathiomolybdate compound as a precursor. It is clear that the TTM compound is a remarkable “building block” for the synthesis of biological-important polynuclear complexes and a molybdenum atom-providing compound for protein redesign and *a de novo* protein design.

1.1.1.5. Tetrathiomolybdate: a model synthetic compound

Thiometallate anions, $MO_xS_{4-x}^{n-}$, are well-known compounds recognised by their strong colours that arise from low energy S → M charge transfer transitions. Usually, the transition metal (M) is in a high oxidation state which offers an unusual redox property and can be used as a ligand to synthesize several heterometal complexes. [89]

We will focus only in the thiometallate anions of the molybdenum (VI), $MoO_xS_{4-x}^{n-}$, more specifically in the tetrathiomolybdate (TTM) compound – MoS_4^{2-}, since among all thiomolybdates compounds, this has been used as a Mo-containing synthetic compound. Furthermore, TTM is one of the studied thiomolybdate compounds due to their ease preparation, thermal and hydrolytic stability and biological roles.

Tetrathiomolybdate synthesis consists of sequential substitutions of the oxygen atoms from a molybdate anion – MoO_4^{2-} [90]. The latter form is colourless, however by substituting the oxygens by sulphur atoms, charge transitions from S → Mo give rise to the characteristic intense colours of the thiometallate anions, such yellow in MoO_3S^{2-}, orange in $MoO_2S_2^{2-}$, orange-red in $MoOS_3^{2-}$, and strong-red in MoS_4^{2-} form. Each one of these forms has specific charge transitions in the UV-visible region and, therefore, whole absorb and interact with light at particular wavelengths [89]. **(Fig.1.7) (Table.1.1)**

Table 1.1. UV-visible characteristic bands and Molar Extinction Coefficients for each thiomolybdate anions. Retrieved from **[89].**

Thiomolybdates	UV/Vis λ/nm (ε $dm^3.mol^{-1}.cm^{-1}$)
MoO_3S^{2-}	288 (–), 390 (–)
$MoO_2S_2^{2-}$	288 (0.39), 320 (0.64), 394 (0.29)
$MoOS_3^{2-}$	315 (0.84), 398 (0.81), 465 (0.14)
MoS_4^{2-}	316 (1.76), 465 (1.24)

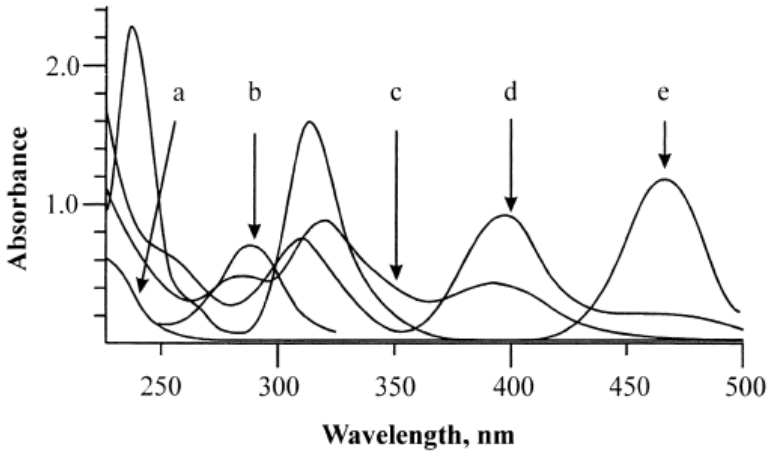

Figure 1.7. UV-Visible spectra of molybdate and thiomolybdates: (a) MoO_4^{2-}, (b) MoO_3S^{2-}, (c) $MoO_2S_2^{2-}$, (d) $MoOS_3^{2-}$ and (e) MoS_4^{2-}. Retrieved from **[92]**.

Additionally, the ability to form linear and complex clusters by bridging sulphide ions between different metals are and have been widely studied, such as Cu- and Fe-heterometal complexes [91,92]. The synthesis of these inorganic complexes normally converges in the mimicking of active-sites of some metalloproteins, like for instances the Mo-Cu active-site of the Orange Protein. Furthermore, TTM-heterometal compounds have also been used in clinical applications, such a chelating-agent for Cu atoms in the treatment of Wilson's disease (a genetic disorder that leads to Cu accumulation in the body) [93], or even in kidney cancer-related treatments by the use of TTM in association with antiangiogenic therapies [94].

1.2. *A De Novo* Protein Design

Over the last decade, the field of *a de novo* protein design expanded in a panoply of applications and these advances have been extensively reviewed over the years [80–85]. Challenging as protein redesign strategies, *a de novo* or "from scratch" design offers us the possibility to disentangle fundamental structure-function relationships while exploiting novel proprieties and functions in peptides and proteins, without the existence of necessary relation to native protein sequences [100]. Contrarily to protein redesign, *a de novo* design postulates that the primary amino acid sequence determines the protein's three-dimensional structure.

In order to design such scaffolds, the construction of stable native-like frameworks by exploring fundamental interactions that contribute to the folding and topology of protein constructs, such as hydrophobic, hydrogen bonding, salt-bridges and Van der Waals contacts, are crucial to avoid the restrains produced by protein's domains and motifs, allostery or multiple metal-binding sites [22,101]. Although this concept is based on minimal design, the intent is to keep a minimum of structural and functional complexity to accomplish protein-like catalytic activities. [102,103]

Early developments in this field begin with the assembled of stable and common secondary structures using hydrophobic interactions as a driving force for folding, and salt-bridges and Van der Walls contacts to guide the topology of the construct. Recently, rather than designing new scaffolds from scratch, previous constructs can be used to design, for instances, metalloproteins, once the existing ones cover the most common structural motifs found in nature. [104,105]

A de novo metalloprotein design is a novel area that has begun to emerge in this field. This area aims to incorporate a metal cofactor-binding site into stable *a de novo* scaffolds without affecting its stability, to mimic native protein active-sites and, ultimately, their catalytic functions. Several successful examples have been reported, in which similar structural and functional characteristics of their native analogues have been acquired, and even new functions have been achieved by non-biological metal complexes with high selectivity. [24]

Such multidisciplinary field has many advantages, like the functionalization of synthetic peptide's active-site in order to accomplish natural and unnatural reactions found in biological systems and the creation of novel sable scaffolds with enzyme-like selectivity's.

1.2.1. Four-helix bundle scaffolds: α_2D family

The lack of long-range interactions and the time-consuming synthesis of peptides and proteins scaffolds are one of the major drawbacks of rational *a de novo* design. Due to this, it is usual that the synthesis of simple and stable complexes, such as four-helix bundle scaffolds, were the starting-point to adapt and define the fold of other *a de novo* α-helix bundles proteins and peptides. [101] **(Table.1.2)**

Table 1.2. α_2 peptides family sequences [99]. Modifications in the primary sequences are highlighted at blue and green letters.

α_2 family	Primary Sequence
α_2B	Ac-GELEELLKKLKELLK-GPTTG-ELEELLKKLKELLKG-NH_2
α_2C	Ac-GE**V**EELLKK**F**KEL**W**K-GPTTG-E**I**EEL**F**KK**F**KEL**I**KG-NH_2
α_2D	Ac-GE**V**EEL**E**KK**F**KEL**W**K-GPTTG-E**I**EEL**H**KK**F**H**E**L**I**KG-NH_2

The helix-loop-helix dimer α_2D is a model example in which single amphiphilic helices aggregate spontaneously. Such folding process is a consequence of the binding energies of hydrophobic interactions that are enough to drive the thermodynamic equilibrium to an energetic-favourable folded state [106–110]. This α_2D dimer is the result of several specific amino acid modifications in primordial helix-bundle α_2-scaffolds, like the α_2B and the α_2C scaffolds that initially adopted a molten globule-like state [111]. **(Fig.1.8)**

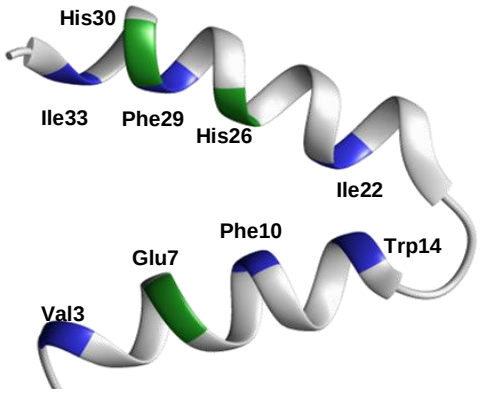

Figure 1.8. Structure of the α_2D scaffold (PDB entry: 1QP6) [108]. The aminoacid modifications are highlighted as in the Table 2. The image was visualized in Chimera1.11.

1.2.2. Three-helix bundle scaffolds: α_3D family

The basic principles that govern the four-helix bundle scaffolds design are also valid for the construction of three-helix bundle scaffolds, such as the α_3D native-like peptide [101,112] **(Fig.1.9)**. The single polypeptide chain preassembles in an antiparallel three-helix bundle in a clockwise or counter-clockwise configuration. Both topologies have been already successfully designed, the counter-clockwise conformation was constructed by DeGrado group [113] and the clockwise configuration was design by Johansson *et al* [114]. However, favourable interhelical interactions only occur in the DeGrado design peptide, which is a typical outcome of a negative design.

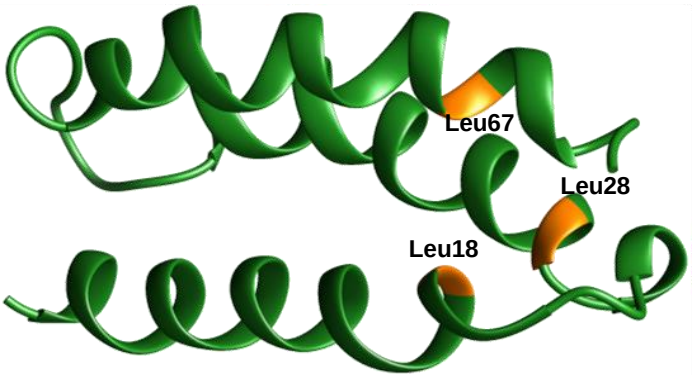

Figure 1.9. Structure of the α_3D scaffold (PDB: 2A3D) **[112]**. The image was visualised in Chimera1.11.

The α_3D scaffold was constructed using a hierarchic approach, in which hydrophobic, electrostatic and helix-capping interactions were enhanced in order to promote a stable packed core [17]. Thereafter, Tebo and Pecoraro reported a metalloenzyme-design study where they replace three apolar residues by three histidine's residues to create a metal-binding site (α_3DH3). They successfully incorporate two different first-row transition metals in the tris(histidine) motif, Zn(II) and Cu(I/II), and obtained two different catalytic activities, the hydration of CO_2 (Zn^{II}) and reduction of nitrite ($Cu^{I/II}$). [115,116]

Such results highlight the potential of *a de novo* metalloenzymes design. Although these catalytic activities are far from enzyme-like efficiencies, this study demonstrates how the evolutionary pressure sculptured the surrounding protein environment in order to tune their biological functions.

1.2.3. α_3D Framework Functionalization: tris(cysteine) environment

The functionalization of the α_3D scaffold by the incorporation of a tris(cysteine) was also achieved by Pecoraro group. The construction of this variant aimed to create a thiol-rich coordination environment found in native metalloregulatory proteins, such as in the MerR, ArsR/SmtB and CadC/CmtR proteins.[117]

The incorporation of a tris(cysteine) symmetric metal-binding site in the α_3D system promoted the binding of several metals, like Co(II), Zn(II), Cd(II),Hg(II) and As(III), resulting in the develop of a novel α-helical bundle metalloprotein – α_3DIV – that can sequester toxic heavy metals [118,119]. Furthermore, the amino acid substitution (3Leu → 3Cys) increased the α-helical content of the α_3D scaffold and promoted additional stabilizing packing interactions, resulting in a more compacted core. [112] **(Fig.1.10)**

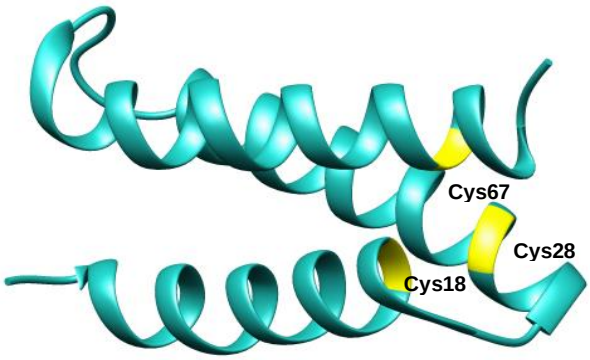

Figure 1.10. Structure of the α_3DIV scaffold (PDB: 2MTQ) **[117].**
The image was visualised in Chimera1.11.

Both variants, α_3D and α_3DIV, present the same counterclockwise topology, but in the α_3DIV scaffold the sequestering of the transition metals Cd(II), Hg(II), and Pb(II) induced further stability and do not introduce any relevant conformational changes [120]. Therefore, this novel synthetic peptide presents a stable framework for forthcoming design metallopeptides that could perform new catalytic reactions, in the same manner that was exploited in this work.

1.2.4. α_3D Framework Functionalization: tetra(cysteine) environment

Iron-sulphur proteins are among the earliest biological metalloredox centres and include a broad range of mononuclear and mixed-clusters structures. The simplest and one of the most carefully studied iron-sulphur protein is the electron-transfer 1-centre rubredoxin – $Fe(Cys)_4$. Rubredoxin is an ideal target for clarifying structure-function relationships in metalloproteins, once

its single-iron active-site only relies on the protein-derived thiolates for assembly and not on external inorganic sulphides.

In fact, there are several studies reported in the literature that exploit the design of the rubredoxin-like active-sites and its specific rubredoxin-like fold [121–123]. Nevertheless, the Rd electron transfer nature difficult its reproducibility, since the designed scaffold has to coordinate and stabilise both Fe(II) and Fe(III) oxidation states.

The first reported example of *a de novo* design scaffold with a rubredoxin-like active-site in a novel and unrelated native fold is the synthetic peptide α_3DIV-L21C [124] **(Fig.1.11)**. This construct was obtained through functionalization of the three-helix bundle scaffold α_3DIV, with the creation of a tetrathiolate metal-binding site by amino acid substitution of a Leu residue by a Cys. Their objective was to mimic the tetracysteinyl environment observed in Cd(II)-binding proteins active-site. [125]

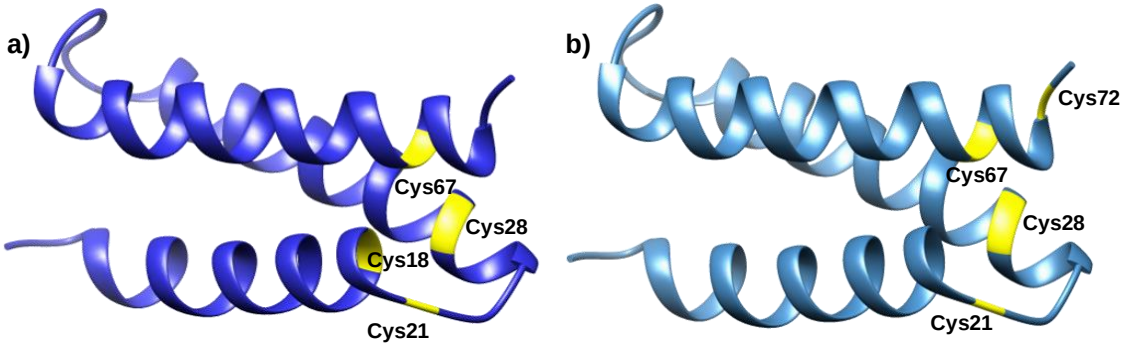

Figure 1.11. 3D structures of the a) α_3DIV-L21C scaffold and b) α_3DIV-H72C scaffold. The structures were modelled in the SWISS MODEL Workspace - ExPASy using the α_3DIV scaffold (PDB: 2MTQ) as template. The images were visualised in Chimera1.11.

The fourth cysteine residue was designed in two different locations (both in loop regions) in the sequence to compare the coordination capability of the two novel variants, the α_3DIV-H72C and α_3DIV-L21C peptides **(Fig.1.11)**. As expected, the arrangement of the coordination environment was different in the two variants. The α_3DIV-H72C peptide exhibited a CdS_3O arrangement, while the α_3DIV-L21C construct displayed a CdS_4 first-sphere coordination environment due to the incorporation of a canonical $C_{18}XXC_{21}$ binding motif. [124]

The CdS_4 coordination environment generated a redox inert species. Therefore, the Fe(II) and Fe(III) ions were rationally chosen to assess the possibility of creating a stable and redox active-site, that is similar to the rubredoxin-like active-site with the same redox potentials of native rubredoxins. In fact, this Fe(Cys_4)–α_3DIV-L21C system have similar spectroscopic features and reduction potentials of its native counterpart [124]. Such results reveal that is possible to design a rigid α-helical synthetic framework with a functional rubredoxin active-site instead of the flexible β-loop region found in natural rubredoxins. [123]

The Fe-α_3DIV-L21C peptide was anaerobically reconstituted in a glove box using ferrous ammonium sulphate as an iron source. This procedure generated the reduced form of this peptide, the Fe(II)-α_3DIV-L21C variant, that was oxidised to the Fe(III)-α_3DIV-L21C form when exposed at the air. Both reduced and oxidised absorption spectrums were similar to the natural system in terms of S → Fe charge-transfer transitions, but the molar extinction coefficient values were three times smaller than in the native rubredoxin, meaning that the peptide structure have some influence in the intensity of these transitions. Additional magnetic circular dichroism spectroscopic studies revealed that the relative energies and polarizations of the thiolate → Fe(III) charge-transfer transitions were also similar to the native counterpart. Furthermore, the iron ion also contributes to the overall stabilization of the peptide structure. [124]

Such results showed that achievement of native-like metalloredox centres in non-natural folds, such in the present case of a CXXC motif embedded in an α-helical bundle, is possible and that the overall fold is not crucial for specific spectroscopic features. Rather, certain architectural features and precise ligand spatial coordination may be favoured over specific folds. Ultimately, incorporation of different biologically active metals into a generalized scaffold could tune these sites for alternative natural and non-natural catalytic functions.

2. Aims

2.1. General aims

This thesis aims to incorporate a molybdenum atom within the rubredoxin-type metal-binding site of *a de novo* designed three-helix bundle peptide – apo-α_3DIV-L21C. The tetracysteinyl active-site in a Mo-substituted synthetic peptide can mimic the tetrathiolate environment of the molybdenum-*bis* pyranopterin-guanosine dinucleotide-containing enzymes catalytic active-site in terms of ligand nature in the Mo first coordination sphere and spectroscopic features.

Ultimately, this model system may be considered a structural and functional analogue for some Mo-*bis* PGD enzymes that have several biological roles and perform important metabolic reactions in the biogeochemical carbon, nitrogen and sulphur cycles. Such diversity in catalytic functions can be accomplished by the coordination of a wide range of ligands, such terminal oxo- or sulphur-atoms derived from exogenous ligands (e.g. =O, –OH, –OH_2, =S, –SH) and/or from the protein's polypeptide residues (e.g. serine, aspartate, cysteine, or selenocysteine).

2.2. Specific aims

In order to consider this *a de novo* designed Mo-α_3DIV-L21C peptide a structural and functional scaffold for some Mo-*bis* PGD enzyme, spectroscopic characterizations, thermal-induced denaturation studies, bioelectrochemical studies and oxidation-reduction tests were performed.

Spectroscopic studies included UV-vis spectroscopy, inductively coupled plasma atomic emission spectroscopy (ICP-AES) and circular dichroism (CD) spectroscopy. Such techniques allow a structural characterization and confirmation of the incorporation of a molybdenum atom within the rubredoxin-like metal-binding site of the α_3DIV-L21C scaffold. Furthermore, through CD analysis we can inquiry about the secondary structure composition and rearrangement upon metal coordination, and speculate about modifications in the fingerprint of the tertiary structure.

Thermal-induced characterization studies, like differential scanning calorimetry (DSC), estimate the specific thermodynamic parameters related to the unfolding process and examine the unfolding models that best described the α_3DIV-L21C system. Electrochemical and reduction studies inquest about the oxidation state of the molybdenum atom, within the α_3DIV-L21C scaffold, and analyse possible redox processes related with the metal physical-chemical proprieties.

Ultimately, a comparison between the apo- and Mo-α_3DIV-L21C peptides, in TCEP-induced reduction conditions and in a non-reducing environment, elucidate the crucial role of the tetracysteinyl environment in the peptide overall stability and in the metal incorporation.

2

Chapter 2. Materials and Methods

2.1. Design of the apo-α_3DIV-L21C peptide

This project is a collaboration with Professor Vincent L. Pecoraro and co-workers from "*De Novo* Designing Coiled-Coil Peptide" laboratory group of the Department of Chemistry and Biophysics of the University of Michigan.

The apo-α_3DIV-L21C peptide was provided in the lyophilized form as a white powder. The production, purification and characterization of this synthetic peptide have been formerly described [124]. The peptide primary sequence is "MGSWAEFKQRLAAIKTRCQACGGSEAE CAAFEKEIAAFESELQAYKGKGNPEVEALRKEAAAIRDECQAYRHN". The calculated molecular mass and molar extinction coefficient of the apo-form is 8209.108 $g.mol^{-1}$ and 8460 $M^{-1}.cm^{-1}$ (ε_{280nm}), respectively.

2.2. Modelling the tetracysteinyl active-site in the α_3DIV scaffold

The three-dimensional structure of the apo-α_3DIV-L21C peptide possessing a tetracysteinyl environment, as the metal-binding site, was obtained through homology modelling using the SWISS MODEL Workspace from ExPASy – SIB Bioinformatics Resource Portal. The input target sequence is described in the previous subsection (2.1.) and the template used for modelling was the PDB file – 2MTQ, which corresponds to the apo-α_3DIV synthetic peptide.

2.3. Molybdenum reconstitution: refolding in the absence of metal

Note: The reconstitution procedure described below was done under aerobic and anaerobic conditions (MBraun UNIlab glovebox). Both conditions gave the same results.

The molybdenum reconstitution of the α_3DIV-L21C scaffold has achieved using the ammonium tetrathiomolybdate (TTM) compound was the precursor (Sigma-Aldrich, CAS Number 15060-55-6, 99.97%). The TTM compound is a black-reddish powder that when solubilize gives rise to a strong-red colour specific of S → Mo charge-transfer transitions associated with the MoS_4^{2-} form.

The reconstitution procedure started with the preparation of a 250 µM solution of apo-α_3DIV-L21C in 50 mM Tris-HCl pH 7.6 buffer, containing 500 µM of the reducing agent TCEP (3,3′,3″-phosphanetriyltripropanoic acid) from Sigma-Aldrich (CAS Number 51805-45-9). A 10 mM TTM solution (metal solution) was prepared in 50 mM Tris-HCl pH 7.6 buffer, containing 20% v/v DMF (N, N-dimethylformamide), from Sigma-Aldrich (CAS Number 68-12-2, 99.8%), to help the metal solubilisation. The metal solution was stirred gently for 20 minutes.

To optimize the reconstitution procedure several solutions of 250 µM of apo-peptide were incubated with different peptide: metal ratios to a final volume of 500 µL. The α_3DIV-L21C:Mo ratios studied were 1:4, 1:6, 1:8, 1:9, 1:10 and 1:15. Two experimental sets were tested: five reaction mixtures were incubated at room temperature and other five at 50 ºC, in a dry hot air oven, for 2 hours, after the addition of the metal solution.

Finished the incubation time, the samples were centrifuged, in a microcentrifuge from WVR™ International, for 10 minutes at 4500 g to remove any precipitate before loading the samples in a Sephadex™ G-25 PD-10 desalting column, from GE Healthcare Life Sciences, that was previously equilibrated with 25 mL of 50 mM Tris-HCl pH 7.6 buffer without TCEP (equilibration buffer). The PD-10 column was used to remove any interfering compounds used in the reconstitution procedure, such as the TTM and TCEP compounds. Each 500 µL samples were loaded into the column and eluted with 25 mL of the equilibration buffer. The Mo-reconstituted peptide elutes in volumes between 1.5 – 3 mL of equilibration buffer. The collected samples with the same UV-vis absorption profile were added to the same tube. The novel Mo-α_3DIV-L21C peptide presents a yellowish colour.

2.4. Metal quantification: ICP-AES analysis

To obtain the molybdenum concentration, in reconstituted Mo-α_3DIV-L21C peptide, elemental analysis was performed. An aqueous solution of 1 mL of Mo-peptide (final colour: yellowish-white) was analysed by Inductively Coupled Plasma – Atomic Emission Spectroscopy (ICP-AES), in an ICP Horiba Jobin-Yvon (Ultima) spectrometer, using the standard solution Reagecon 23 multi-elements in a concentration range of 0.05 – 3 ppm.

2.5. Protein quantification: Lowry protein assay protocol

To determine the peptide concentration a colourimetric Lowry protein assay was performed, using the bovine serum albumin (BSA) as a standard liquid solution (Sigma-Aldrich, CAS Number 9048-46-8, 2 mg protein/mL). The Lowry quantification method employs two colourimetric reactions. The first one occurs when the Cu(II) atoms present in the Biuret reagent reacts with the peptide bonds, in alkaline conditions, resulting in the reduction of Cu(II) to Cu(I). The second reaction takes place when the phosphomolybdotungstate complex, present in the Folin-Ciocaltaeu reagent, is reduced to heteropolymolybdenum blue due to the oxidation of aromatic residues catalysed by copper. The concentration of the reduced Folin-reagent is proportional to the protein concentration. **(Fig. 2.1)**

The standard samples were made in duplicate and in a concentration range of 0 to 400 $\mu g.mL^{-1}$ of BSA. A standard curve of absorbance was plotted as a function of BSA concentration to determine the unknown peptide concentration. The colourimetric measures were done using a Shimadzu UV-1800 double-beam UV-VIS spectrophotometer at 750 nm **(Table 2.1)**.

Table 2.1. Absorbance measurements for each BSA concentration, at 750 nm.

[BSA] ($\mu g.mL^{-1}$)	Measured absorbance at 750 nm *	Corrected absorbance at 750 nm *
0	0.070	0
100	0.113	0.044
150	0.132	0.063
200	0.148	0.079
250	0.170	0.101
300	0.186	0.116
400	0.217	0.148

* Average absorbance values.

The protocol initiates by adding 100 µL of each protein samples to a 15 mL falcon tube and addition of 400 µL of Biuret reagent (10 minute incubation time). Subsequently, 3.5 mL of 2.3% m/v sodium carbonate (Na_2CO_3) (Sigma Aldrich, CAS Number 497-19-8, 99.999%) and 100 µL of Folin-Ciocalteu´s phenol reagent (Sigma Aldrich, MDL Number MFCD00132625) were added to the 15 mL tube and the samples were gently mixed, in a vortex, and incubated for 30 minutes. Completed the incubation time, the absorbance of each standard and unknown samples was measured at 750 nm. [126]

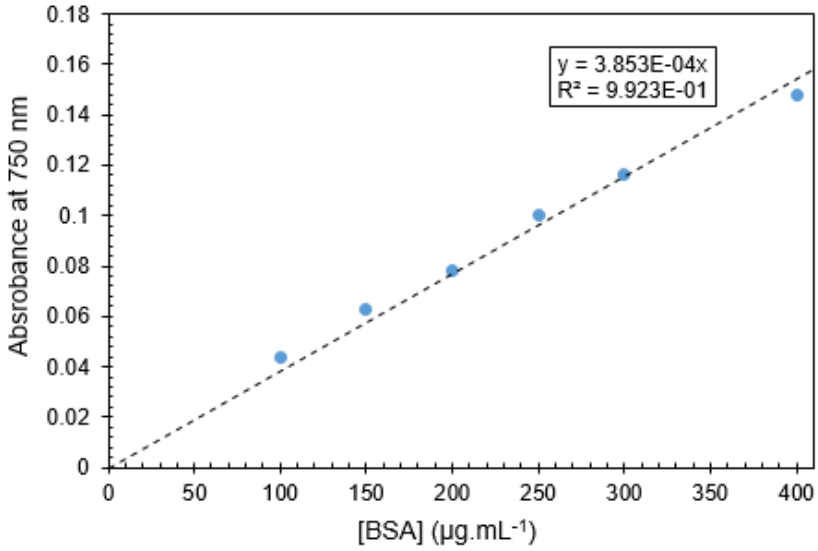

Figure 2.1. Standard calibration curve. At blue are the experimental Abs values. The dotted black line is the linear fit of the absorbance as a function of [BSA].

2.6. Spectroscopic characterisation

2.6.1. Absorption spectroscopy

The Ultraviolet-Visible spectroscopy was performed on a Shimadzu UV-1800 double-beam UV-VIS spectrophotometer and the spectra were visualised through an UVProve software. The spectra were recorded in 1 cm quartz cuvettes at slow speed and room temperature, with a scan pitch of 0.5 nm and a scan range from 250 to 800 nm.

2.6.2. Circular dichroism (CD) Spectroscopy

Circular dichroism characterization was performed on an Applied Photophysics Chirascan™ qCD spectrometer. The CD data is either reported in millidegrees (mdeg) of ellipticity (θ) as a function of wavelength or is represented in mean residue ellipticity ($[\theta]_{MRE}$) as a function of wavelength [127–129]. The $[\theta]_{MRE}$ is the CD raw data corrected for the sample concentration **(Equation 2.1)**:

(Eq. 2.1)

$$[\theta]\left(\frac{\text{deg.cm}^2}{\text{dmol}}\right) = \frac{\theta\ (\text{deg}) * \text{MRW}}{10 * \text{L} * \text{C}}$$

MRW (Mean Residue Weight) = M / (N-1) (g/mol)
M = protein molecular mass (g/mol)
N = protein residues number
L = cell path length (cm)
C = protein concentration (g/mL)

To obtain information about the secondary structure composition, spectra for both apo- and Mo-α_3DIV-L21C forms were recorded in the Far-UV region (190 – 260 nm) [130]. For the Far-UV studies, the final samples of apo- and Mo-peptide forms were prepared in 10 mM Tris-HCl pH 7.6 buffer with 0.5 mM of TCEP. The measurements were performed in a 1 mm path length cuvette with a total volume of 300 µL. The CD spectra presented are an average of three spectral acquisitions at 25 ºC, before and after the temperature cycle, with bandwidth and a step-size of 1 nm. The temperature-dependent Far-UV CD spectra were performed in a temperature range of 10 ºC to 94 ºC, with a stepped ramp mode of 0.4 seconds per point, a temperature increment of 2 ºC for each measurement and a stabilization period of 1 second in each temperature, to estimate the midpoint of the unfolding process or melting temperature (T_m) in the Far-UV region [131].

Furthermore, information about the tertiary structure fingerprint (aromatic amino acids and disulphide bonds) [132] and metal-ligand interactions (L → M charge-transfer transitions or metal d–d transitions) were also studied, exclusively, for the Mo-α_3DIV-L21C form. These data were obtained by studying the near-UV region (260 – 320 nm) of the CD spectra and the visible region (320 – 600 nm) [133,134]. For these studies, a sample of Mo-peptide form, with a concentration of 70 µM, was prepared in 10 mM Tris-HCl pH 7.6 buffer with TCEP. The measurements were performed in a 10 mm path length quartz cuvette with a total volume of 2 mL. The CD spectra presented are an average of three spectral acquisitions at 25 ºC, before and after the temperature cycle, with bandwidth and a step-size of 1 nm. The temperature-dependent near-UV/visible CD spectra were performed in a temperature range of 19 ºC to 94 ºC, with a stepped ramp mode of 0.3 seconds per point, a temperature increment of 3 ºC for each measurement and a stabilization period of 1 second in each temperature , to estimate the melting temperature (T_m) in the visible region.

2.7. Differential Scanning Calorimetry (DSC)

Differential scanning calorimetry characterization was performed in a TA™ Nano DSC apparatus. DSC technique was used to characterize the stability and the folding process of the apo- and Mo-α_3DIV-L21C forms [135–137]. The thermodynamic parameters and melting temperature were obtained by fitting the thermograms in a NanoAnalyze™ v3.10.0 Data Analysis software (TA Instruments).

Normally, since proteins in solution are in equilibrium between folded (native) and unfolded (denatured) states, by heating the sample in a constant rate and, subsequently, measuring the heat change associated with intrinsic thermal denaturation processes, we can determine the calorimetric enthalpy (ΔH_{cal}) and the change in heat capacity (ΔCp) of the unfolding process [138]. Besides these thermodynamic proprieties, the DSC data also provides the T_m of the sample (maximum value). The T_m value correlates with the temperature at which the protein's unfolded and folded states are in equal concentrations and is an indicator of the protein thermal stability.

Furthermore, the van't Hoff enthalpy (ΔH_{VH}) and the change in entropy (ΔS) are also indirectly provided by the DSC analysis, by analysing the shape of the thermogram [138]. The ΔH_{VH} measure the cooperativity of the transition, assuming a reversible two-state transition. In addition, the comparison of the ΔH_{cal} with the ΔH_{VH} is a method to verify the assumed two-state model used in the van't Hoff calculations ($\Delta H_{VH}/\Delta H_{cal} = 1$). $\Delta H_{VH}/\Delta H_{cal}$ ratios above 1 (one) may be an indication of self-association processes and ratios below 1 (one) is indicative of an unfolding process via one or more intermediate states. [138,139]

For these studies, the final samples of apo- and Mo-peptides were prepared in 50 mM phosphate buffer at pH 7.6 with 0.1 mM of TCEP. For these measurements were used 700 µL of each sample in concentrations of 0.4 mg/mL for the Mo-form and 0.5 mg/mL for the apo-form. The temperature range was -10 ºC to 130 ºC and the data were collected in an anaerobic Coy box atmosphere.

2.8. Reducing tests

Incubation studies were performed to speculate about the molybdenum oxidation state in the Mo-α_3DIV-L21C scaffold. The reduction of the Mo atom, Mo(VI) → Mo(V)/Mo(IV), was tested by incubation with three reducing agents: 1,4-dithiothreitol (DTT) (Sigma Aldrich, CAS Number 3483-12-3), sodium hydrosulphite (dithionite) (Sigma Aldrich, CAS Number 7775-14-6) and sodium ascorbate (Sigma Aldrich, CAS Number 134-03-2, ≥98%).

The Mo-peptide was incubated with ascorbate and, consequently, purified in a PD-10 desalting column, to remove the excess of ascorbate in solution since it absorbs in the visible region [140]. Once DTT and dithionite mainly absorb in the ultraviolet region is not necessary to purify the samples in PD-10 column. All spectra were recorded on a Shimadzu UV-1800 double-beam UV-VIS spectrophotometer and visualized through an UVProve software.

To initiate the incubation experiment with DTT and dithionite, firstly, the Mo-α_3DIV-L21C peptide (175 µM) was added to a 1 cm quartz cuvette. Solutions of the two reducing compounds, with a final concentration of 35 mM, were prepared to ensure a 1:1 stoichiometry using 5 µL of the solution. A total of 2 µL of DTT (0.4 equivalents) and 1 µL of dithionite (0.2 equivalents) was added to the cuvette and, in each addition, the solution was left incubate 5 min with a constant stir. The DTT test was performed aerobically and the dithionite test anaerobically, by partially degassing with N_2 in a Schlenk line.

In the incubation test with ascorbate, 116 µM of Mo-α_3DIV-L21C peptide was added to a 1 mL eppendorf (Vf_{inal} = 280 µL). A solution of ascorbate, with a final concentration of 580 µM, was prepared aerobically to achieve a 1:5 stoichiometry when 25 µL of the solution was added to the eppendorf (V_{final} = 280 µL). The solution was left incubate for 15 minutes and then passed in a PD-10 desalting column, equilibrated with 50 mM phosphate buffer at pH 7.6, to remove the excess of ascorbate. Fractions of 250 µL were collected in 1 mL eppendorfs, and the ones with the same absorption profile were combined.

2.9. Electrochemical characterization

Electrochemistry is a technique that examines the interaction of electricity and a detectable chemical change by considering the movement of electric charges between an electrolyte and electrodes. This technique can be applied in biomolecules (e.g. enzymes) that can perform electrophysiological reactions to study their oxidation-reduction (redox) reactions. [141–145]

The electrochemical behaviour, of the apo- and Mo-α_3DIV-L21C systems, was studied with a Potentiostat/Galvanostat Type III, using one compartment electrochemical cell. The experimental setup was performed in a GPES (General Purpose Electrochemical System) software. All the components are from Metrohm Autolab.

To characterize the intrinsic electrocatalytic properties, thin layer cyclic voltammetry (TLCV) was performed in both apo- and Mo-peptides. The assays were performed inside a Faraday cage using a three electrode's configuration in a single compartment electrochemical cell. The electrodes used were pyrolytic graphite (PG) as working electrode (4 mm), platine wire as counter-electrode and saturated calomel electrode (SCE) as a reference electrode. The potential values were obtained in SCE values, but the reported values are in the normal hydrogen electrode (NHE) reference **(Eq. 2.2)**:

$$\mathrm{E/V\ (vs.\ NHE)} = \mathrm{E/V\ (vs.\ SCE)} + 0.241 \quad \text{(Eq. 2.2)}$$

Before each experiment, the PG electrode was previously polished with 0.3 and 1 µm micropolish alumina powder, from BUEHLER (Item Numbers: 40-10077 and 40-10079, respectively), then immersed in an ultra-sound bath (Millipore water) for 3 minutes and lastly thoroughly cleaned with Millipore water.

For each experiment, 15 µL of apo-α_3DIV-L21C (200 – 250 µM) or 15 µL Mo-α_3DIV-L21C (50 – 150 µM) were placed on the working electrode (WE). To enhance the electrochemical signal, 4 µL of neomycin sulphate (2 mM) (Sigma Aldrich, CAS Number 1405-10-3) was also added to the WE. After coating the electrode, a solvent casting technique, at room temperature, was applied until it reached half of the initial volume. Consequently, a thin layer cellulose membrane with a 3.5 kDa cut-off was positioned above the WE and immobilized with parafilm to entrap the peptide. The electrolyte solution (25 mL), prepared on the single electrochemical cell, consisted in 50 mM Tris-HCl buffer at pH 7.6 with 100 mM of NaCl, 20 mM neomycin sulphate and 500 µM of TCEP. Several scan rates, from 5 mV/s to 100 mV/s, were tested. The electrochemical measurements were performed in an anaerobic environment, provided by a glovebox ($[O_2]_{max}$ = 3.5 ppm), and all the solutions (except the peptide solutions) were degassed with a continuous flow of argon, at least by 30 min, before were introduce in the anaerobic chamber.

Besides the assay above, several conditions were tested to ensure a optimize result. Such conditions involved different pH's (acetate buffer at pH 5.5; Tris-HCl buffer at pH 7.6; Tris-HCl

buffer at pH 8.5), reducing or non-reducing conditions (with or without TCEP) and aerobic or anaerobic environments. Furthermore, three blanks were also tested “in solution” approach under anaerobic conditions. The blanks tested were: (I) 50 mM Tris-HCl buffer at pH 7.6 with 100 mM of NaCl, 20 mM neomycin sulphate and 500 µM of TCEP; (II) 50 mM Tris-HCl buffer at pH 7.6 with 100 mM of NaCl, 20 mM neomycin sulphate and 150 µM of TTM compound and (III) 50 mM Tris-HCl buffer at pH 7.6 with 100 mM of NaCl and 20 mM neomycin sulphate. In these latter assays, the working electrode was coated with only 4 µL of neomycin sulphate (2 mM) and covered with a thin layer cellulose membrane (3.5 kDa cut-off). In this report, only the preliminary optimized result for the apo- and Mo-α_3DIV-L21C peptides is revealed.

3

Chapter 3. Results and Discussion

3.1. Modelling the structure of the apo-α$_3$DIVL21C scaffold

The three-dimensional structure of the apo-α$_3$DIV-L21C peptide was modelled, with the SWISS MODEL Workspace, using as structural template the three-helix bundle α$_3$DIV scaffold (PDB: 2MTQ). The primary sequence was modified through amino-acid substitution of a leucine residue by a cysteine in position 21 (L21C) **(Table 3.1)**. This substitution led to the creation of a canonical rubredoxin-like CXXC motif with a tetracysteinyl environment as a metal-binding site.

Table 3.1. Primary sequences of α$_3$DIV and α$_3$DIV-L21C scaffolds. Cysteine residues are highlighted at blue. Amino acid substitution (L21C) is highlighted at red.

Peptide scaffold	Primary Sequence
α_3DIV	MGSWAEFKQRLAAIKTRCQALGGSEAECAAFEKEIAAFESEL-QAYKGKGNPEVEALRKEAAAIRDECQAYRHN
α_3DIV-L21C	MGSWAEFKQRLAAIKTRCQACGGSEAECAAFEKEIAAFESEL-QAYKGKGNPEVEALRKEAAAIRDECQAYRHN

The model built presents a sequence identity of 98.63 % and a sequence similarity of 0.60 to the model template used. Besides, the model has a GMQE (Global Model Quality Estimation) of 0.99 which indicates a high homology accuracy between the template and the model built (0 < GMQE < 1) [146]. Furthermore, a QMEAN (Qualitative Model Energy ANalysis) of -0.85 demonstrates a good agreement between the model and experimental structures of similar size (QMEAN close to zero) [147].

Since the only primary-sequence difference, between the α_3DIV-L21C and α_3DIV scaffolds, is a single mutation in position 21 and the SWISS MODEL scores obtain for the model quality evaluation are good, it seems that the amino acid substitution does not affect the overall peptide's fold. **(Fig. 3.1)**

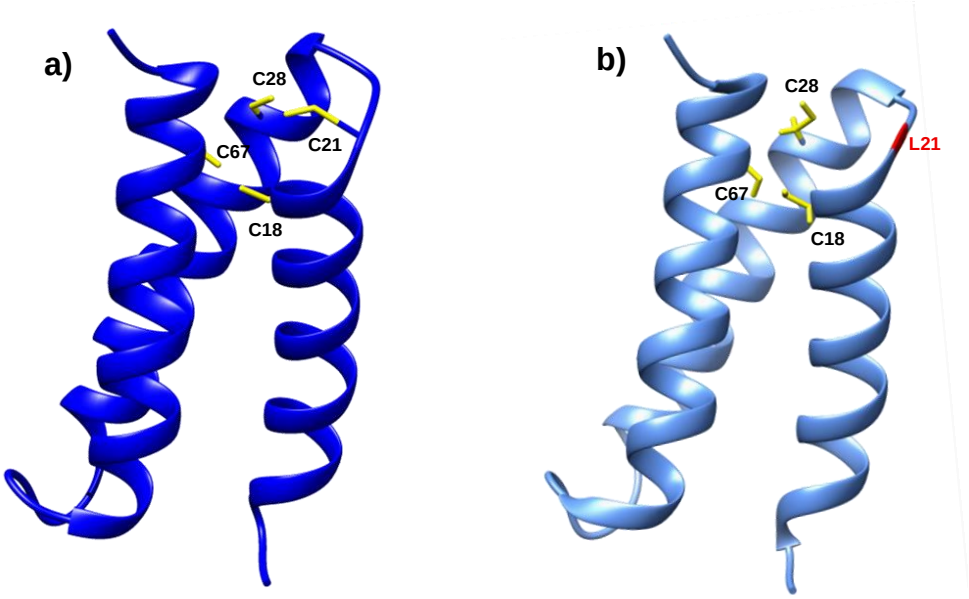

Figure 3.1. Three-dimensional structures of the **a)** α_3DIV-L21C and **b)** α_3DIV scaffolds. The α_3DIV-L21C was modelled in the SWISS MODEL Workspace from ExPASy, using the PDB entry: 2MTQ as template. The structures were edited in Chimera 1.11.

Nevertheless, some differences appear in the distance values between the cysteine residues in the metal-binding site. The amino acid substitution (L21C), in the α_3DIV scaffold, entails a decrease in the Cys18-Cys67, Cys28-Cys67 and Cys18-Cys28 distance values. Conversely, the distances between the Cys18-Cys21 and Cys21-Cys28 appear to increase, when are compared with the Cys18-Leu21 and Leu21-Cys28. The increase of the distance between the Cys18-Cys21 and Cys21-Cys28 residues is explained by the residues side-chain size. Leucine residues create a greater spatial hindrance because of the larger side-chain (isobutyl group) that cysteines thiol side-chain. **(Fig. 3.2) (Table 3.2)**

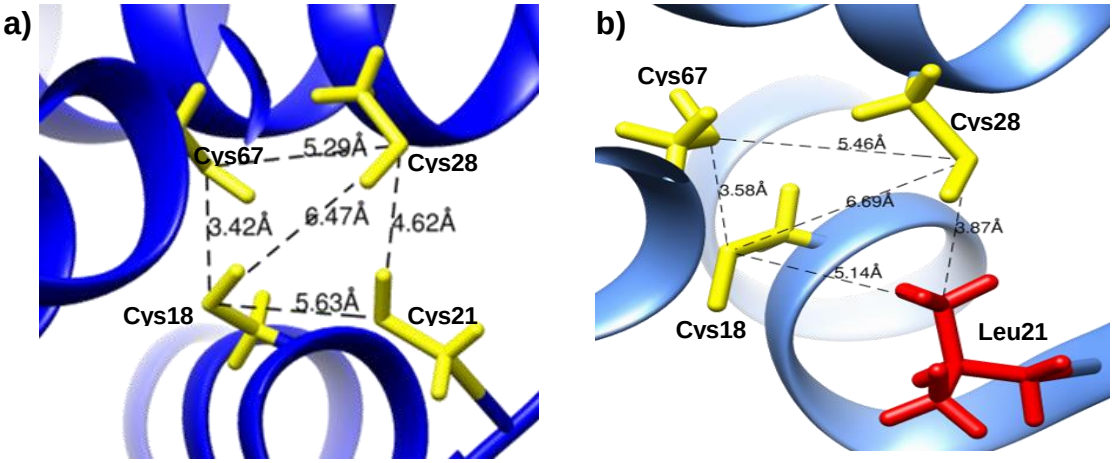

Figure 3.2. Enlarged view of the apo-peptides metal-binding sites: (a) tetracysteinyl environment in the α_3DIV-L21C peptide and (b) triscysteinyl environment in the α_3DIV scaffold (PDB entry: 2MTQ). The residue distances were calculated and visualized in Chimera 1.11.

Table 3.2. Residue pairs distance presented in the cysteinyl metal-binding site of the α_3DIV and α_3DIV-L21C scaffolds.

Residue pairs	Residue distances (Å) α_3DIV scaffold	Residue distances (Å) α_3DIV-L21C scaffold	
Cys18-Cys67	3.58	3.42	↓
Cys28-Cys67	5.46	5.29	↓
Cys21-Cys28	–	4.62	↑
Leu21-Cys28	3.67	–	
Cys18-Cys21	–	5.63	↑
Cys18-Leu21	5.14	–	
Cys18-Cys28	6.69	6.47	↓

The presence of the non-polar aliphatic side chain of leucine entails a slight hydrophobic character to the metal-binding site, which forces hydrophilic residues, such as cysteines, to depart from the binding site **(Fig. 3.3)**. Ultimately, when the Leu was substituted by an amino acid with a polar-side chain (cysteine), the Cys18-Cys28-Cys67 residues can mutually stabilize through disulphide bonds and their spatial distance decreases.

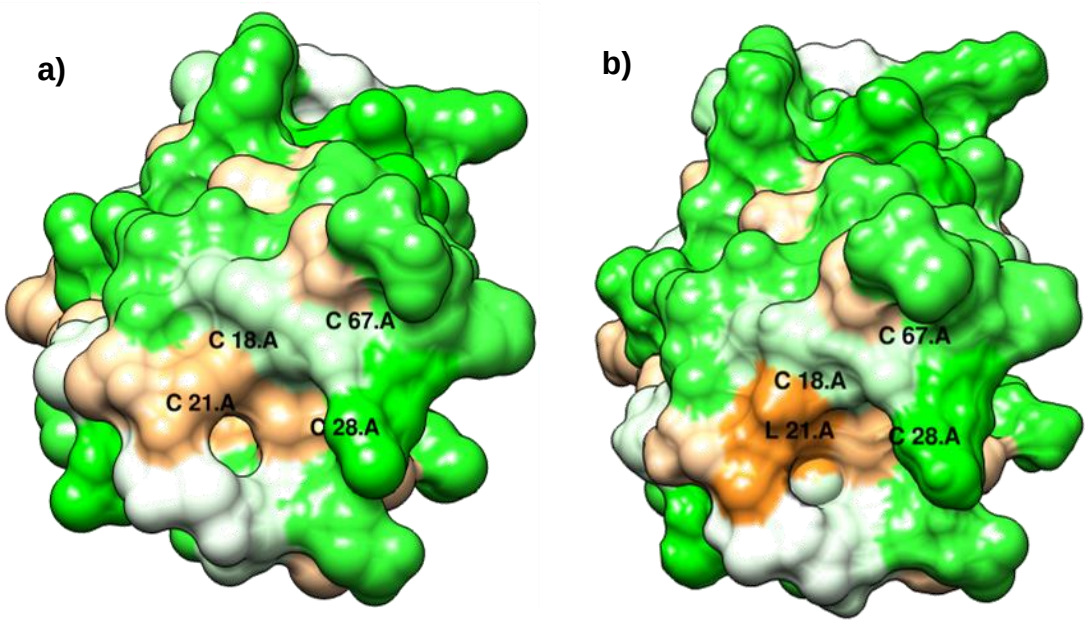

Figure 3.3. Amino acid hydrophobicity in the (a) α_3DIV-L21C and (b) α_3DIV (PDB entry: 2MTQ) scaffolds. Most hydrophilic residues are highlighted at green and the most hydrophobic residues at orange. The molecular surface was coloured using the Kyte-Doolittle scale in Chimera 1.11.

3.2. Molybdenum reconstitution and UV-vis characterization

The refolding of the apo-α_3DIV-L21C peptide was performed in TCEP-induced reducing conditions to prevent the formation of disulphide bonds, by oxidation of cysteine residues, and to enhance the metal incorporation. Subsequently, the peptide incubation with different concentrations of tetrathiomolybdate was accomplish by fixing 6 peptide: metal ratios, 1peptide:4Mo, 1peptide:6Mo, 1peptide:8Mo, 1peptide:9Mo, 1peptide:10Mo and 1peptide:15Mo. The reconstitution procedure was attempted at room temperature and at 50 ºC, with long incubation times and under aerobic and anaerobic conditions. All the experimental sets given the same incorporation results. In **Fig. 3.4** are represented the UV-visible spectra obtain, under aerobic conditions at room temperature, and the spectral development achieved by the interaction of the Mo atom with the tetracysteinyl environment in the metal-binding site.

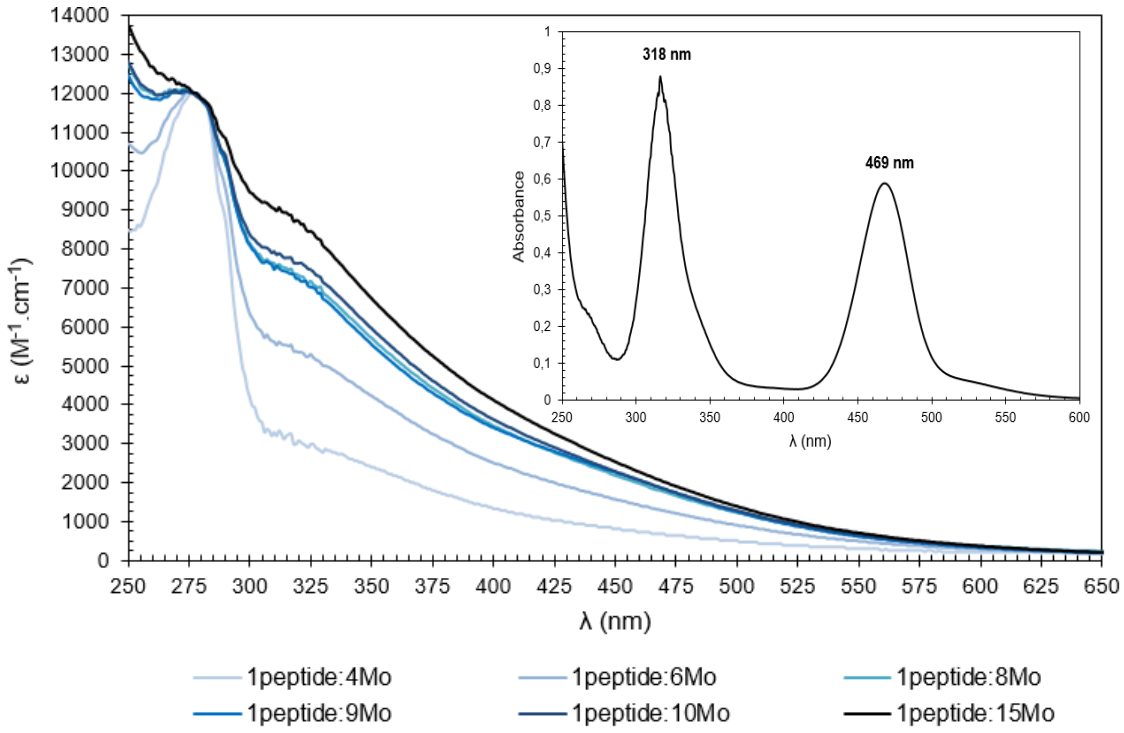

Figure 3.4. UV-visible spectra of the peptide: metal ratio tested. Each reconstitution procedure was carried in 50mM Tris-HCl buffer at pH 7.6 with 0.5 mM TCEP. The experiment was performed at room temperature under aerobic conditions. Spectra were normalised to protein concentration. In inset is the UV-vis spectrum of the TTM compound.

These results demonstrate that increasing the molybdenum concentration enhances the metal incorporation in the apo-α_3DIV-L21C scaffold. The appearance of two unresolved shoulders between 300-330 nm and 450-475 nm, characteristic of thiolate-Mo charge-transfer bands [89,91,92], confirm the Mo incorporation. These transitions are similar to the ones observed in the UV-vis spectrum of the free TTM compound, which has spectral maximums at 318 and 469 nm **(Fig.3.4. inset)**

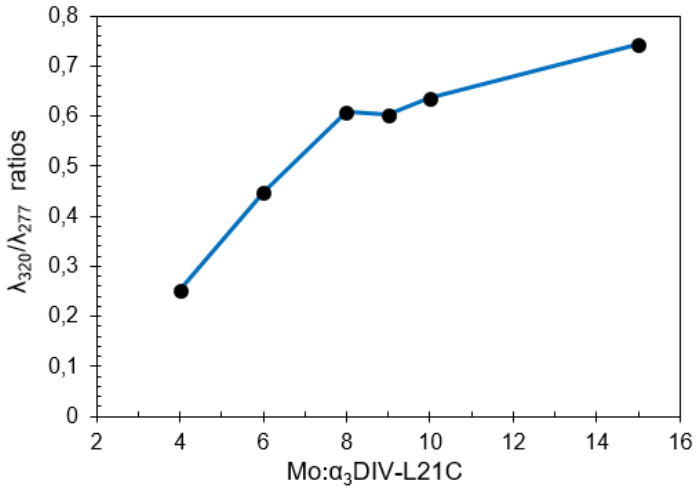

Figure 3.5. Variation of the $\lambda_{320}/\lambda_{277}$ ratio values as a function of the different metal to protein ratios tested.

Furthermore, by observing the spectral development, the system reaches stabilization at 1:8, 1:9 and 1:10 ratios **(Fig.3.5)**. These results are confirmed by the $\lambda_{320}/\lambda_{277}$ absorbance ratios, which also stabilize at 0.608, 0.603, and 0.636 for the 1:8 and 1:9 and 1:10 ratios, respectively. In peptide: metal stoichiometry above 1:10, the absorbance ratio intensely increases, which suggests an unspecific interaction of the metal with the peptide scaffold. These unspecific interactions may arise from electrostatically interactions in the peptide surface instead of coordination with the cysteinyl sulphurs in the metal-binding site. This deduction is further corroborated by the incorporation ratios estimated by Lowry an ICP quantification. **(Table 3.3)**

Table 3.3. Incorporation ratios determine for each reconstitution ratio tested.

Reconstitution ratio peptide:metal	[α3DIV-L21C] by Lowry method (µM)	[Molybdenum] by ICP analysis (µM)	Incorporation ratio [Mo]/[peptide]	$\lambda_{320}/\lambda_{277}$ ratio
1.4	40.6	7.46	0.18	0.252
1:6	46.6	24.1	0.52	0.448
1:8	41.6	44.0	**1.06**	0.608
1:9	33.0	33.6	**1**	0.603
1:10	45.5	61.0	1.32	0.636
1:15	36.9	104.0	2.8	0.743

The reconstituted Mo-α_3DIV-L21C (or holo-α_3DIV-L21C) presents an absorption maximum at 277 nm (ε = 12000 $M^{-1}.cm^{-1}$) and two unresolved shoulders at 320 nm (ε = 7400 $M^{-1}.cm^{-1}$) and 470 nm (ε = 2000 $M^{-1}.cm^{-1}$). These transitions are very similar to the ones obtain in the molybdenum-substituted rubredoxins (Mo-Rd), redesigned by Maiti *et al*. In this case, the Mo-Rd system demonstrated an absorption maxima at 278 nm (ε = 17770 $M^{-1}.cm^{-1}$) and two unresolved shoulders at 314 (ε = 8010 $M^{-1}.cm^{-1}$) and 450 nm (ε = 1020 $M^{-1}.cm^{-1}$) [52]. These results were expected because in both systems (Mo-α_3DIV-L21C and Mo-Rd), the molybdenum atom coordinates in the same tetracysteinyl environment provided by a rubredoxin-like motif and, so, Mo-thiolate charge-transfer bands appear.

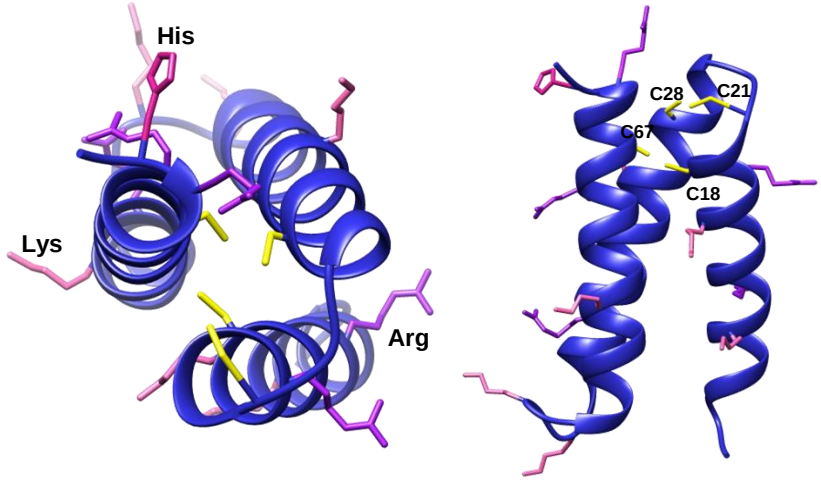

Figure 3.6. Positive charged amino acids in the α_3DIV-L21C scaffold. Side-chains of arginine residues at purple, of histidine residues at magenta and of lysine residues at hot pink. Side-chain of cysteine residues at yellow. Structures were edited in Chimera 1.11.

From these data, we conclude that this is an effective approach to coordinate a Mo atom in the α_3DIV-L21C scaffold. Quantification data reveal a 90% reconstitution efficiency in ratios of 1peptide:8/9Mo atoms and UV-vis spectral analysis confirm the metal coordination in the specifically-designed rubredoxin-like metal-binding site. In ratios above 1peptide:10Mo atoms, unspecific electrostatic interactions of the molybdenum atom with the positive residues, histidine (His), lysine (Lys) and arginine (Arg), in the peptide surface emerge. **(Fig. 3.6)**

Moreover, to achieve the metal incorporation it is necessary excess of molybdenum atoms (8-9x superior) relatively to the peptide concentration. This requirement is explained by the relative position of the rubredoxin-like active-site which, in the α_3DIV-L21C scaffold, is positioned in a rigid three α-helices bundle and, in the rubredoxin structure, is located in a flexible β-loop region [148] that provides more degrees of freedom to the protein structure and, consequently, the metal-binding site. **(Fig. 3.7)**

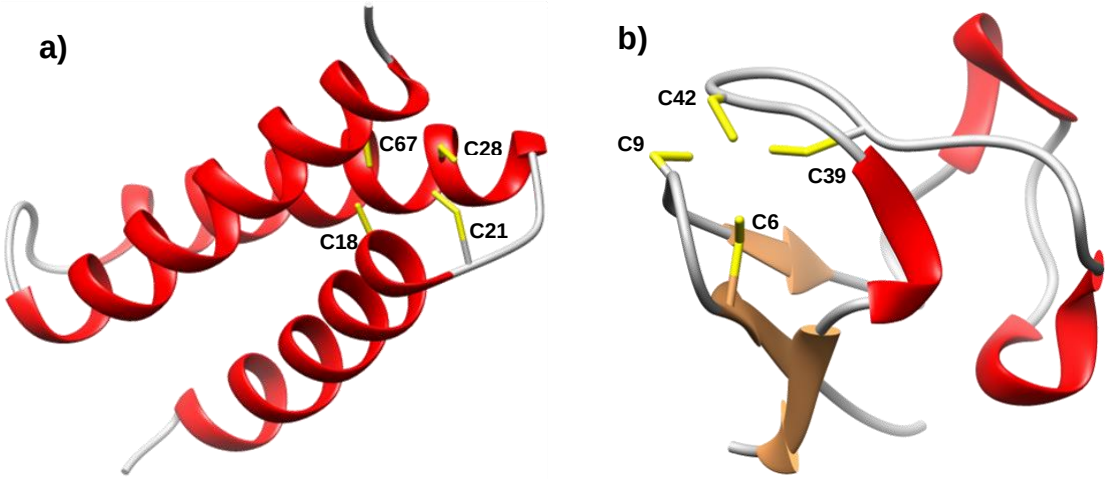

Figure 3.7. Comparison of secondary structures composition between (a) apo-α_3DIV-L21C scaffold and (b) rubredoxin from *D. gigas* (PDB: 2DSX). α-helices highlighted at red; β-sheets at salmon and coiled coils at grey. Structures were edited in Chimera 1.11.

3.3. Circular dichroism (CD) characterization

3.3.1. Far-UV absorption CD characterization

Circular dichroism studies, in the Far-UV region (190 – 260 nm), provide important information about the typology and the content of a protein/peptide secondary structures [127,129]. The far-UV spectra for both apo-α_3DIV-L21C and Mo-α_3DIV-L21C forms confirm the helical structure conformation of the α_3DIV-L21C scaffold. The presence of one broad transition at 222 nm ($n \rightarrow \pi^*$) and one positive maximum at 195 nm ($\pi \rightarrow \pi^*$) indicate a typical α-helical system as expected [130]. Furthermore, the $[\Theta]_{222}/[\Theta]_{208}$ ratios close to 1 (one) support the α-helical character of both forms and reveal that the incorporation of a molybdenum atom within the metal-binding site does not affect the secondary structure profile. **(Fig. 3.8)**

To test the thermal stability of both apo- and holo-systems and, ultimately, estimate the melting temperature, a temperature ramp, from 10 ºC to 90 ºC, was performed. The spectra in each case follow a similar denaturation profile that is, as the temperature increases, the CD signals at 222 and 208 nm approaches to 0 (zero), which indicates a thermally-induced denaturation of the secondary structure **(Fig. 3.9 and 3.10)**.

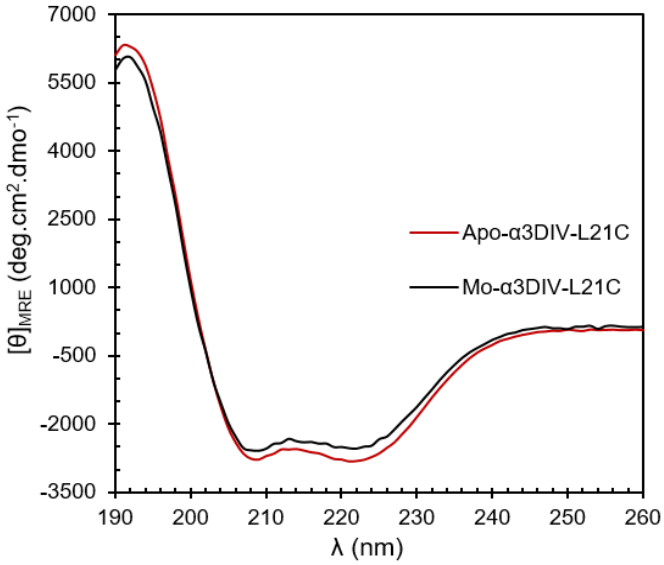

Figure 3.8. CD average spectra, in the far-UV region, of the apo- and Mo-α_3DIV-L21C peptides before the temperature cycles. The spectra were collected in 10 mM Tris-HCl pH 7.6 buffer, with 0.5 mM TCEP, in a 0.1 cm pathlength cuvette at 26 ºC.

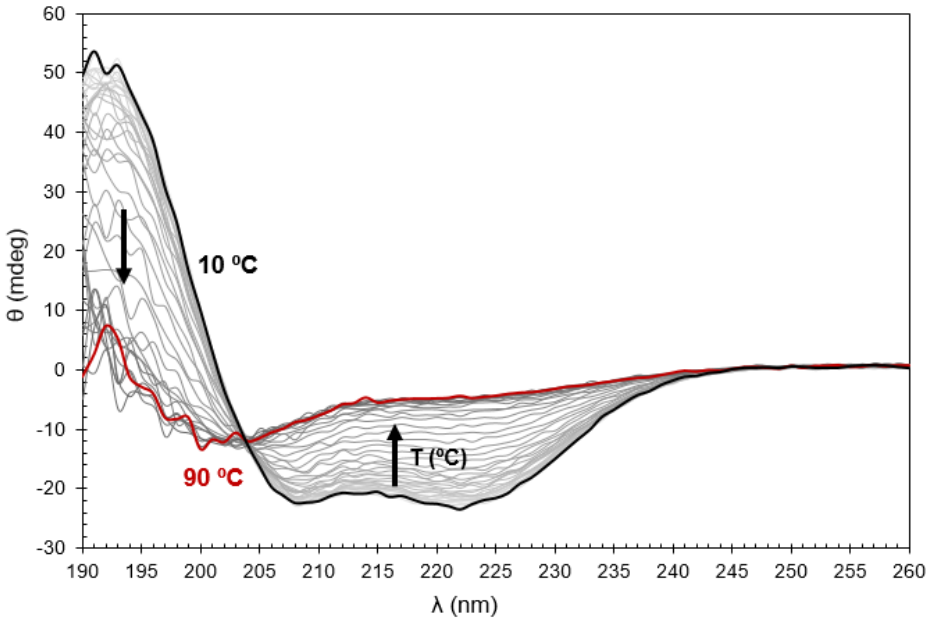

Figure 3.9. Temperature cycles (from 10°C to 90°C) of apo-α_3DIV-L21C peptide in the far-UV region. Spectra were collected in 10 mM Tris-HCl pH 7.6 buffer, with 0.5 mM TCEP, in a 0.1 cm pathlength cuvette with a stepped ramp mode of 0.4 seconds per point. The temperature increment was 2 ºC for each spectra with a stabilization period of 1 second in each temperature.

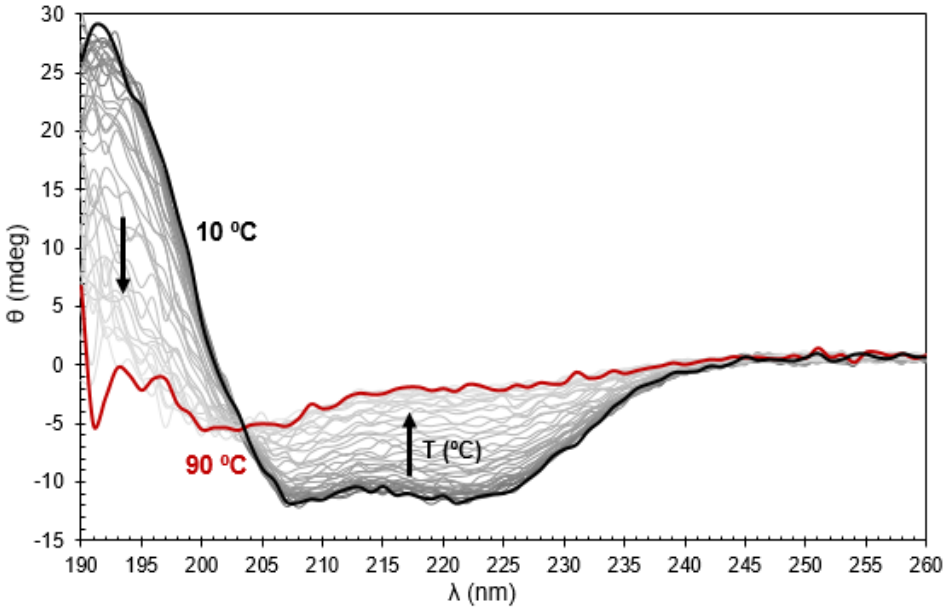

Figure 3.10. Temperature cycles (from 10 °C to 90 °C) of Mo-α$_3$DIV-L21C peptide in the far-UV region. Spectra were collected in 10 mM Tris-HCl pH 7.6 buffer, with 0.5 mM TCEP, in a 0.1 cm pathlength cuvette with a stepped ramp mode of 0.4 seconds per point. The temperature increment was 2 ºC for each spectra with a stabilization period of 1 second in each temperature.

The loss of secondary structure is consistent with the decrease of the $[\Theta]_{222}/[\Theta]_{208}$ ratio values calculated at 90 ºC. Additionally, the CD spectra of both systems after the temperature cycle (at 26 – 30 ºC) displays a regain in the secondary structure profile, with the characteristic CD signals at 208 and 222 nm **(Fig. 3.11)**, and a $[\Theta]_{222}/[\Theta]_{208}$ ratios close to one.

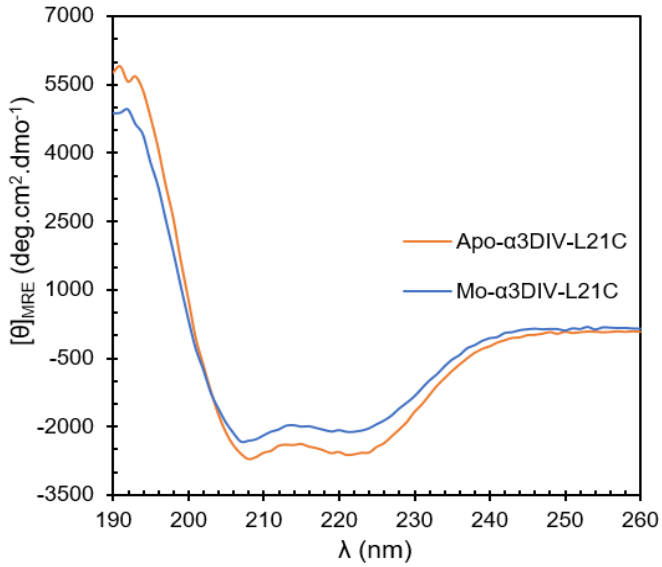

Figure 3.11. CD average spectra, in the far-UV region, of the apo- and Mo-α$_3$DIV-L21C peptides after the temperature cycles. The spectra were collected in 10 mM Tris-HCl pH 7.6 buffer, with 0.5 mM TCEP, in a 0.1 cm pathlength cuvette at 26 °C.

Interestingly, by comparing the $[\Theta]_{222}/[\Theta]_{208}$ ratios of the apo- and Mo-α_3DIV-L21C peptides with and without TCEP, it is possible to conclude that a presence of a reducing agent promotes a more accentuated thermal destabilization in the secondary structure **(Table 3.4)**. This behaviour, in the absence of TCEP, can be explained by the formation of disulphide bridges between the four cysteine residues, in the metal-site after metal losing, which imposes a more thermally robust scaffold even at 90 ºC. In TCEP induced reducing conditions, the cysteines are being reduced, which prevents the formation of SS-bonds and further destabilizes the secondary structure. Furthermore, in each case, the apo-peptide retains more its folded secondary structure, which indicates higher thermal stability.

Table 3.4. Comparison between $[\Theta]_{222}/[\Theta]_{208}$ ratios for apo- and Mo-α_3DIV-L21C at 10 °C, 50 ºC, 90 °C and after the temperature ramp. The ratios in the absence of TCEP were retrieved from [152].

	Sample	$[\Theta]_{222}/[\Theta]_{208}$ 10 ºC	$[\Theta]_{222}/[\Theta]_{208}$ 50 ºC	$[\Theta]_{222}/[\Theta]_{208}$ 90 ºC	$[\Theta]_{222}/[\Theta]_{208}$ 25 ºC *
With TCEP	**Apo-α_3DIV-L21C**	1.05	0.92	0.49	0.96
	Mo-α_3DIV-L21C	0.98	0.91	0.36	0.91
Without TCEP	**Apo-α_3DIV-L21C**	1.00	0.84	0.81	1.00
	Mo-α_3DIV-L21C	0.97	0.82	0.63	0.94

* After temperature ramp.

To determine the thermodynamic parameters, such as the melting temperature (T_m) and the enthalpy of folding (ΔH), the variation in mean residue ellipticity ($[\Theta]_{MRE}$) at 222 nm as a function of temperature was plotted for both apo- and Mo-α_3DIV-L21C forms in the presence of TCEP. The theoretical data was calculated and fitted to the experimental data using the equations for a two-state transition of a monomer from a folded to unfolded state, that assumes an equal heat capacity (ΔCp) for both states **(Equations 3.1, 3.2 and 3.3)**. [131]

$$f = \big((u - l) * y\big) + l \quad (3.1)$$

$$y = \frac{k}{1 + k} \quad (3.2)$$

$$k = e^{\left(\frac{h}{1.987 * t}\right) * \left(\left(\frac{t}{m}\right) - 1\right)} \quad (3.3)$$

k = folding constant at any given temperature	$(cal.mol^{-1}.K^{-1})$
y = fraction folded at any given temperature	
f = ellipticity at any given temperature	$(deg.cm^2.dmol^{-1})$
l = $[\theta]$ of unfolded protein	$(deg.cm^2.dmol^{-1})$
u = $[\theta]$ of 100% folded helical protein	$(deg.cm^2.dmol^{-1})$
h = starting enthalpy	$(cal.mol^{-1})$
t = given temperature	(K)
m = melting temperature	(K)

The melting temperature estimated for both apo- and Mo-α3DIV-L21C forms (in the presence of TCEP), regarding the peptide's secondary structure, were extremely similar, being 60.0 ºC and 60.3 ºC, respectively. Such results reveal that the secondary structure remains in its original fold even if a molybdenum atom is incorporated in the tetracysteinyl metal-binding site. Furthermore, the enthalpy of folding (ΔH) was also estimated for both peptide forms, the apo-peptide have a ΔH of -100.6 kJ.mol^{-1} (-24.0 kcal.mol^{-1}) and the Mo-peptide a ΔH of -80.9 kJ.mol^{-1} (-19.3 kcal.mol^{-1}). **(Fig. 3.12 and 3.13)**

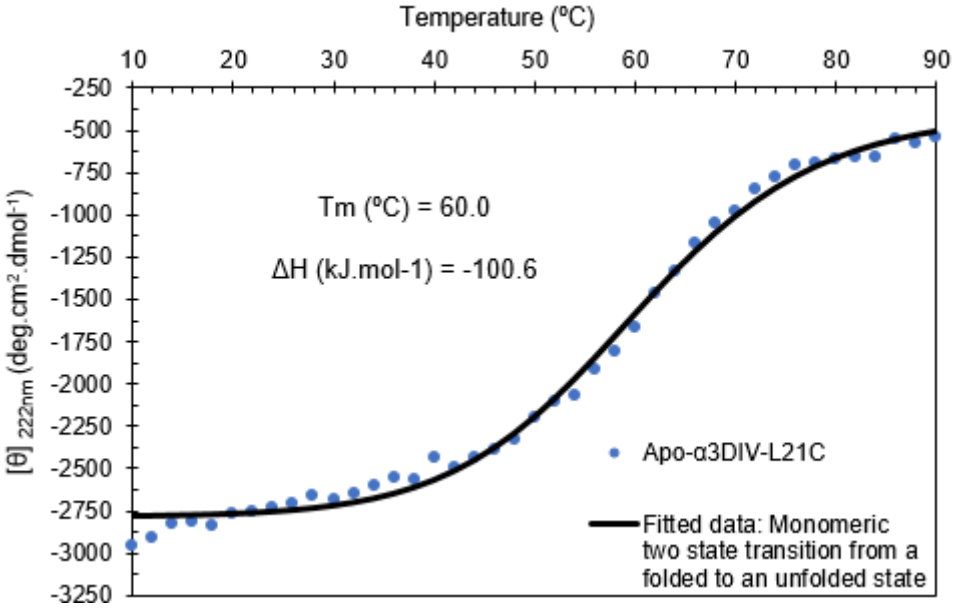

Figure 3.12. Variation of the mean residue ellipticity ($[\Theta]_{MRE}$) at 222 nm as a function of temperature apo-α3DIV-L21C peptide (at blue), in the presence of TCEP. The experimental data were fitted using the equations for a two-state transition (solid black line).

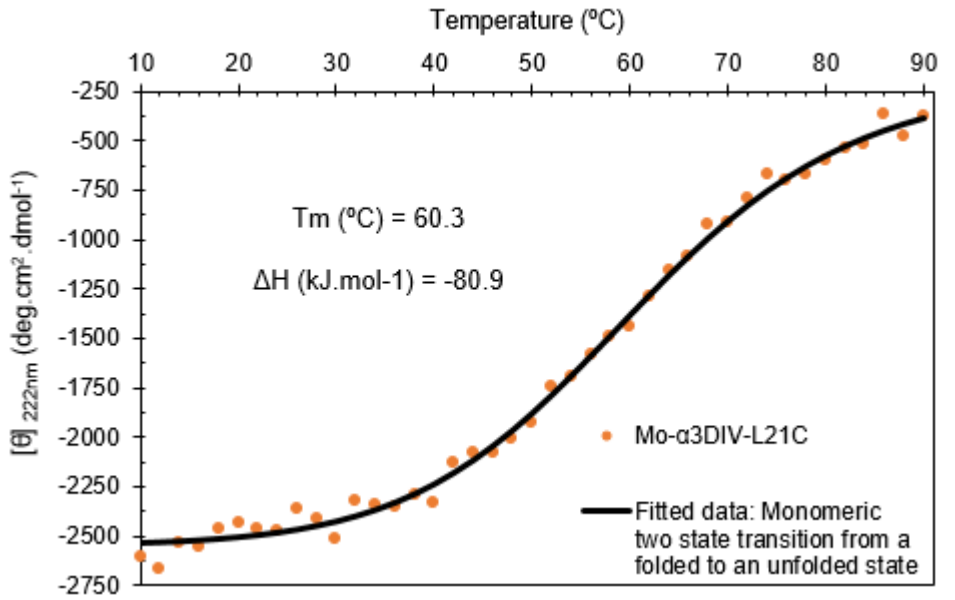

Figure 3.13. Variation of the mean residue ellipticity ($[\Theta]_{MRE}$) at 222 nm as a function of temperature Mo-α3DIV-L21C peptide (at orange), in the presence of TCEP. The experimental data were fitted using the equations for a two-state transition (solid black line).

These results suggest that the α_3DIV-L21C scaffold releases energy in the folding process by the formation of hydrogen bonds, ionic salt bridges and Van der Waals forces. These enthalpic contributions, at lower temperatures, outweigh the entropic contributions provided by the hydrophobic interactions, leading to a spontaneous folding process. Conversely, at higher temperatures, the entropic effects are more prominent, leading to an energetically-favourable unfolding process [149,150]. These results were expected since the α_3DIV scaffold was carefully constructed to spontaneously fold by virtue of hydrophobic interactions [113].

Nevertheless, a ΔH value differentiation of ≈ -20 kJ.mol^{-1} for both apo- and Mo-peptides suggest that the incorporation of a molybdenum atom within the metal-binding promotes a small destabilization in the secondary structure, leading to a slightly less spontaneous folding process. These results diverge from the ones obtain in the incorporation of the iron atom in the α_3DIV-L21C scaffold. In this case, the Fe-coordination in the tetracysteinyl environment does not alter significantly the enthalpy of folding ($\Delta H_{apo\text{-}\alpha3DIV\text{-}L21C}$ = 140.9 kJ.mol^{-1}; $\Delta H_{Fe\text{-}\alpha3DIV\text{-}L21C}$ = 143.7 kJ.mol^{-1}) [124]. The difference observed may be explained by the fact that molybdenum has a higher atomic radius than iron (190 pm for Mo; 156 pm for Fe) and, therefore, for the smaller Fe atom the access and coordination on the metal-binding site are more favourable in terms of intrinsic peptide structural hindrance [151,152].

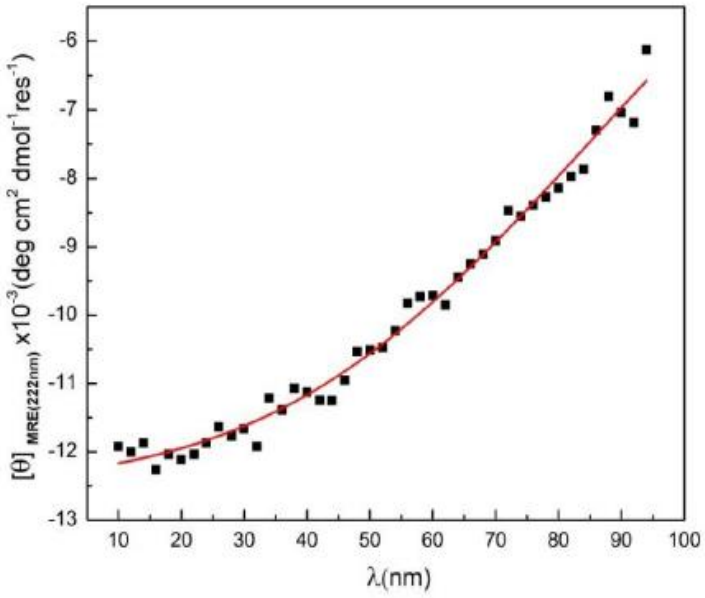

Figure 3.14. Variation of the mean residue ellipticity ($[\Theta]_{MRE}$) at 222 nm as a function of temperature apo-α_3DIV-L21C peptide (at black), in the absence of TCEP. The experimental data were fitted using the equations for a two-state transition of a monomer from a folded to unfolded state, assuming an equal heat capacity for both states (solid red line). Remove from [153].

Preliminary CD studies for T_m and ΔH determination, of both apo- and Mo-α3DIV-L21C forms without TCEP-induced reducing conditions, failed to promote stabilization in the resultant trending curve of the fitted data and, therefore, precluding the determination of the thermodynamic parameters [153] **(Fig.3.14)**. Such results might be explained by the formation of inter-disulphide bonds between several α3DIV-L21C scaffolds, which leads to various structural oligomers. In the presence of TCEP, the formation of S-S bonds is prevented leading to a unique structural conformation of the α3DIV-L21C scaffold.

3.3.2. Near-UV absorption CD characterization

Circular dichroism studies in the near-UV region provide a "fingerprint" of the protein tertiary structure [129]. The contributions in the near-UV region arise from transitions in the environment of each aromatic residue side chain, such as tryptophan, tyrosine and phenylalanine. Besides, contributions from disulphide bonds may also appear but the intensity of the transition is much weaker than the aromatic amino acid contributions. [132,154]

The α3DIV-L21C scaffold contains six aromatic residues in its primary sequence: two tyrosine (Tyr) residues, one in the C-terminal region, and one tryptophan (Trp) residue in the N-terminal region, all exposed to the solvent, and three phenylalanine (Phe) residues embedded in the hydrophobic core **(Fig. 3.15)**.

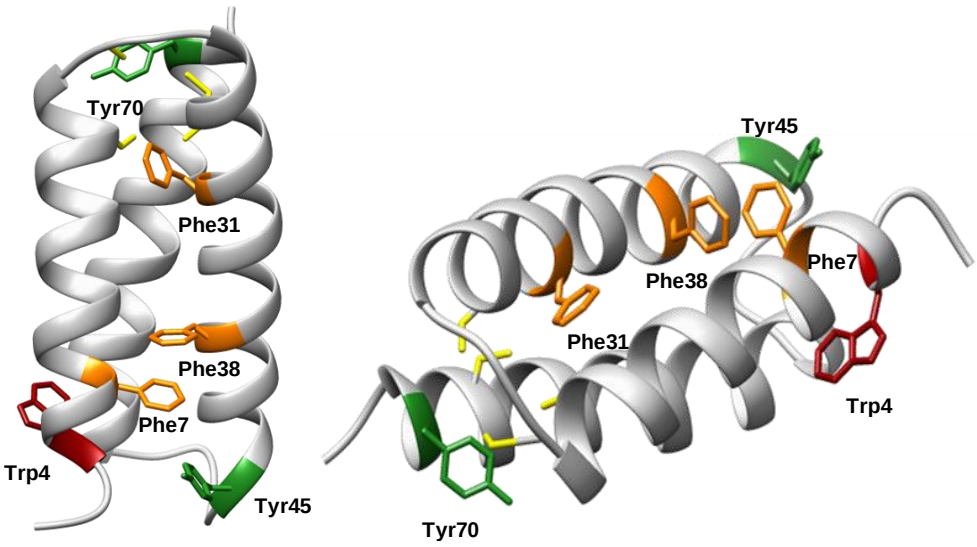

Figure 3.15. Aromatic amino acids in the α3DIV-L21C scaffold. Tryptophan residue at red, tyrosine residues at green and phenylalanine residues at orange. Side-chain of cysteine residues at yellow. Structure was edited in Chimera 1.11.

In **Fig.3.16** is the near-UV spectral comparison of the apo and Mo-α$_3$DIV-L21C peptides in the absence of TCEP. The CD spectra of both forms present some differences related to the sharpening and definition of the peak contributions. In both cases, the negative intensity peaks between 260 – 270 nm could be attributed to the phenylalanine contributions. The tyrosine contributions appear between 275 and 285 nm and the broad positive peak between 290 – 292 nm can be attributed to the unique tryptophan residue. The assignment of sharp intensity peaks with specific aromatic side-chain contributions is not as straightforward as it seems since the contributions of Phe – Tyr and Tyr – Trp may overlap. [129]

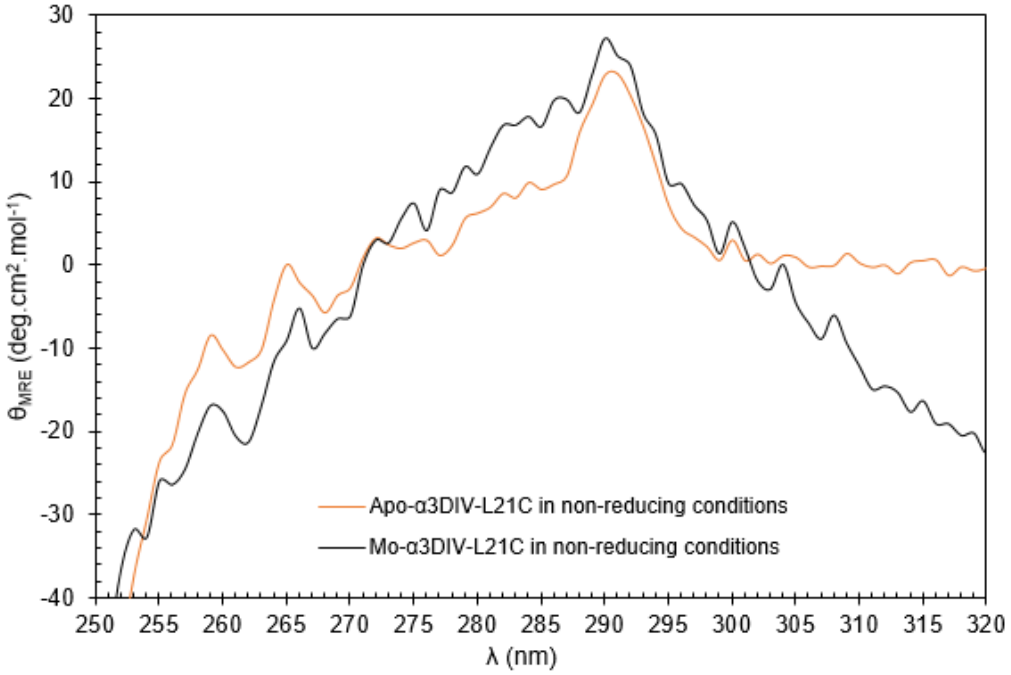

Figure 3.16. CD spectra overlap of apo- and Mo-α$_3$DIV-L21C peptides (70 μM), in non-reducing conditions. Spectra were collected in 10 mM Tris-HCl pH 7.6 buffer in a 10 mm pathlength cuvette at 20 °C.

Nevertheless, a broader near-UV spectral profile, in the apo-peptide, may suggest additional spectral contributions, possibly from a disulphide-bonds formation within the tetracysteinyl environment. Although, the spectrum from the apo-scaffold is less sharp and defined that the Mo-counterpart, the overall peak profile is very similar which indicate some smaller changes in the tertiary structure upon metal-binding.

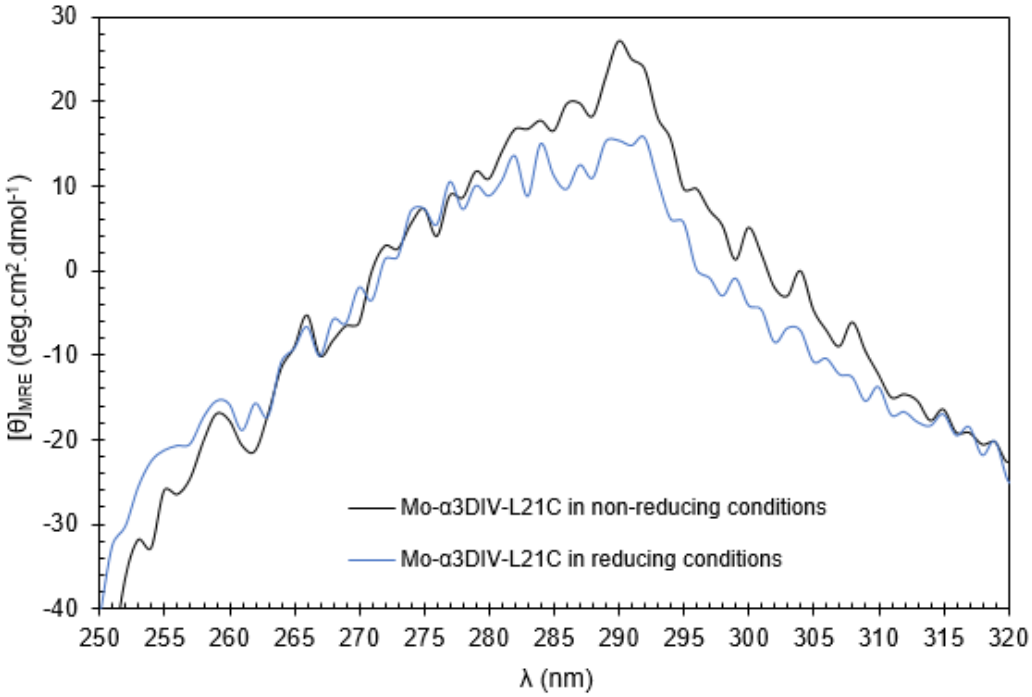

Figure 3.17. CD spectra overlap of Mo-α3DIV-L21C peptide (70 μM), in non-reducing and TCEP-induced reducing conditions. Spectra were collected in 10 mM Tris-HCl pH 7.6 buffer, with or without 0.5 mM of TCEP, in a 10 mm pathlength cuvette at 20 °C.

Furthermore, the near-UV spectra of Mo-α3DIV-L21C peptide in TCEP-induced reducing and non-reducing conditions were also compared **(Fig.3.17)**. Both spectra present a similar peak profile however, in a reducing environment, the aromatic amino-acid contributions appear more sharpened and defined. This behaviour may be explained by changes in the environment of each side chain residues, such as additional hydrogen bonding and electrostatic interactions, and polarizability effects, induced by the reducing agent TCEP [112,114,137,156]. As expected, such interactions seem to have a higher influence in the Tyr – Trp spectral contributions region (275 – 292 nm), since the side chains of this two aromatic residues are exposed to the solvent.

Nonetheless, in non-reducing conditions, the formation of disulphide bridges, within the tetracysteinyl environment, may also account to the spectral broadening. These results suggest the presence of a reducing agent do not promote significant alterations on the overall tertiary structure fingerprint but change the surrounding side-chain environment in some aromatic residues.

3.3.3. Visible absorption CD characterization

Circular dichroism studies in the visible region are useful in systems holding charge-transfer transitions originated from metal-ligand complexes [133,134,157], like in the Mo-α3DIV-L21C scaffold that comprises a molybdenum atom coordinated in a tetracysteinyl environment (Mo-thiolate transitions). This coordination imposes a chiral environment in the metal-binding site with a specific CD signal in the visible region.

The CD data from the Mo-α3DIV-L21C scaffold, in the presence of TCEP, exhibits an intense absorption band with a maximum at 392 nm **(Fig. 3.18)**. This spectral contribution in the visible region and the absence of a CD signal from tetrathiomolybdate supports the successful incorporation of the Mo atom in the rubredoxin-like metal-binding site.

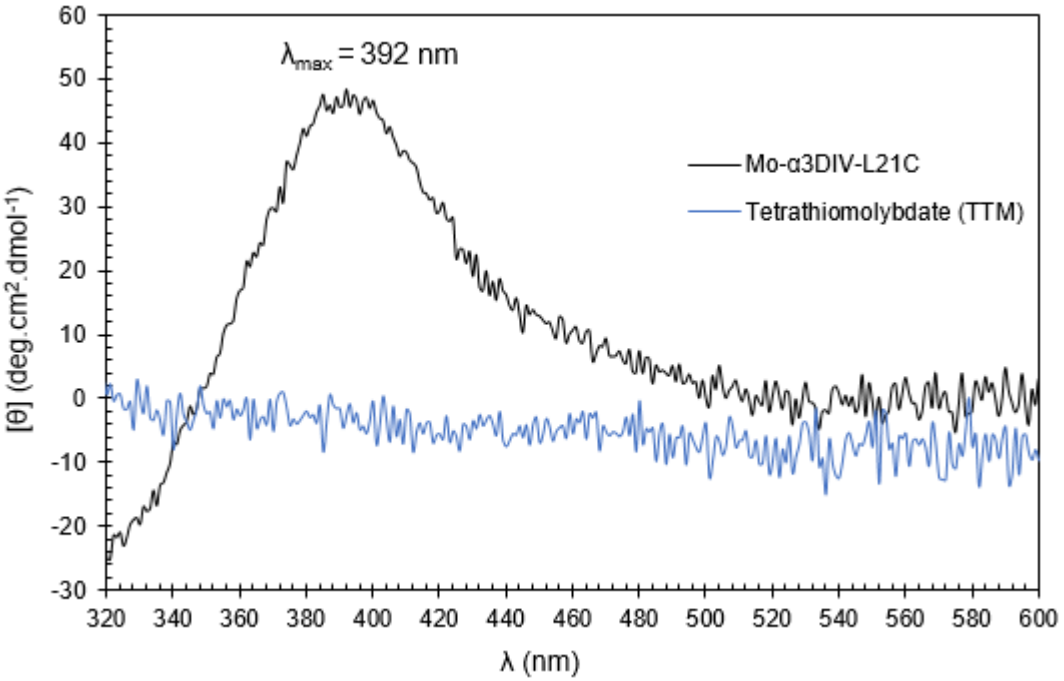

Figure 3.18. CD average spectra, in the visible region, of the Mo-α3DIV-L21C peptide (black solid line) and of the tetrathiomolybdate compound (blue solid line). The spectra were collected in 10 mM Tris-HCl pH 7.6 buffer, with 0.5 mM of TCEP, in a 10 mm pathlength cuvette at 26 ºC.

The thermal stability in the visible region was also evaluated. The spectra exhibit a loss in the characteristic CD signal ([Θ] close to zero) as a consequence of thermal-induced denaturation of the secondary structure **(Fig.3.19)**. The thermodynamic parameters (T_m and ΔH) were also estimated by fitting the experimental data to the equations for a two-state transition of a monomer from a folded to unfolded state used in the previous section **(Eq. 3.1, 3.2 and 3.3)** [131]. The variation in mean residue ellipticity ($[\Theta]_{MRE}$) was followed at 392 nm as a function of temperature. The Mo-α3DIV-L21C peptide has an estimated melting temperature of 73.6 ºC and the enthalpy of the folding of -125.9 kJ.mol^{-1} (-30.1 kcal.mol^{-1}) **(Fig. 3.20)**. The parameters determined, reveals two parallel denaturation behaviours in the α3DIV-L21C scaffold, one in the rubredoxin-like metal-binding site and the second one in the overall secondary structure.

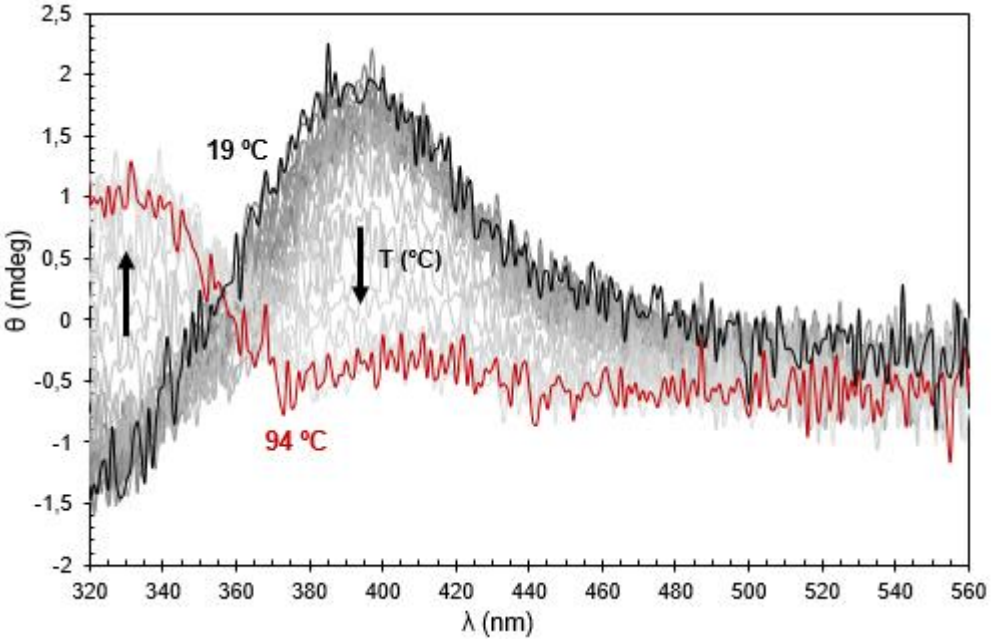

Figure 3.19. Temperature cycles (from 19 °C to 94 °C) of Mo-α$_3$DIV-L21C peptide in the visible region. Spectra were collected in 10 mM Tris-HCl pH 7.6 buffer, with 0.5 mM TCEP, in a 10 mm pathlength cuvette with a stepped ramp mode of 0.3 seconds per point. The temperature increment was 3 ºC for each spectra with a stabilization period of 1 second in each temperature.

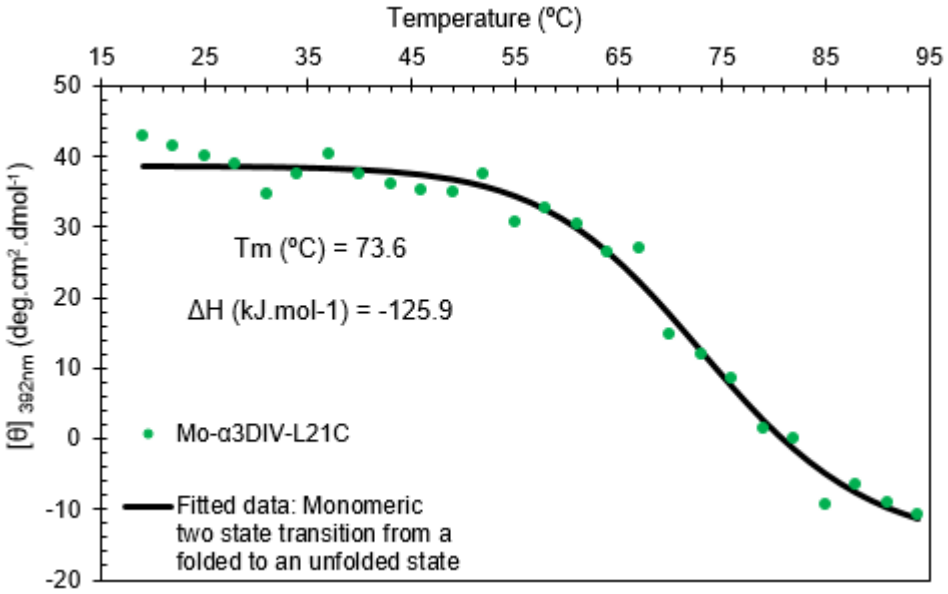

Figure 3.20. Variation of the mean residue ellipticity ($[\Theta]_{MRE}$) at 392 nm as a function of temperature for the Mo-α$_3$DIV-L21C peptide. The experimental data was fitted using the equations for a two-state transition of a monomer from a folded to unfolded state, assuming an equal heat capacity for both states (solid black line).

These results suggest that the secondary structure undergo an initial thermal-induced denaturation (at 60 ºC) prior to the loss of the molybdenum-thiolate coordination complex (at 74 ºC). Such behaviour implies that the rubredoxin-like metal-binding site is more stable to an

increase in temperature than the overall secondary structure and that the [Mo(SCys)$_4$] site does not control the thermal-stability of the native fold of the α$_3$DIV-L21C scaffold [158,159]. Furthermore, an estimated ΔH value of -125.9 kJ.mol^{-1} suggests that the coordination of the molybdenum atom by cysteine residues occurs spontaneously. Nevertheless, the estimation of these thermodynamic parameters is affected by an experimental error from the impossibly of achieving a plateau region at higher temperatures.

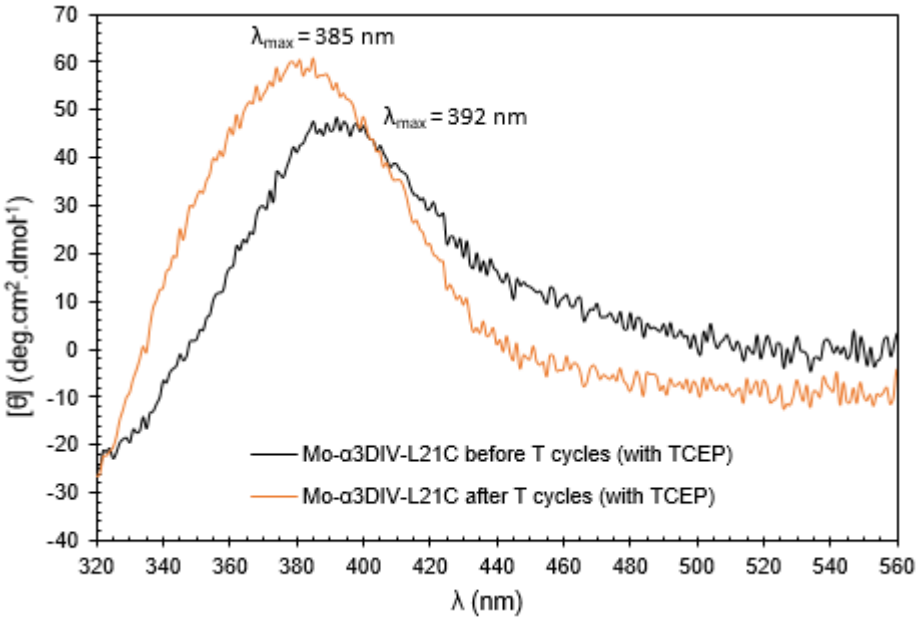

Figure 3.21. CD average spectra, before and after the T cycles, of the Mo-α$_3$DIV-L21C peptide in reducing conditions. The spectra were collected in 10 mM Tris-HCl pH 7.6 buffer with 0.5 mM TCEP, in a 10 mm pathlength cuvette at 26 ºC.

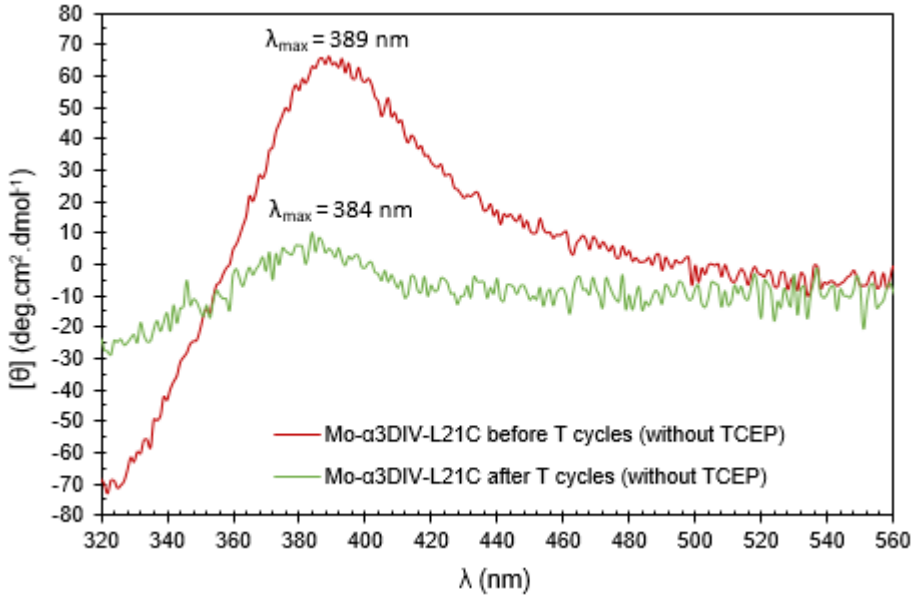

Figure 3.22. CD average spectra, before and after the T cycles, of the Mo-α3DIV-L21C pep-tide in non-reducing conditions. The spectra were collected in 10 mM Tris-HCl pH 7.6 buffer, in a 10 mm pathlength cuvette at 26 ºC.

Subsequently, to the temperature cycles, the CD spectra of the Mo-α$_3$DIV-L21C peptide, in TCEP-induced reducing conditions, was collected again at 26 ºC. The data in the visible region displays a regain of the positive intensity with a maximum at 385 nm **(Fig. 3.21)**. This wavelength is distinct to the one observed before the temperature ramp (392 nm). Such results suggest that the metal coordinates again to the peptide but some differences in the metal coordination may be observed such as the metal being coordinated only by one, two or three cysteine residues before reaching an equilibrium that leads to the coordination in a tetracysteinyl environment. The UV-vis spectra collected before and after the temperature cycles further confirm the formation of other(s) Mo-thiolate specie(s) distinct(s) from the initial MoS_4^{2-} compound **(Fig. 3.23)**. Interestingly, the CD spectra of Mo-α$_3$DIV-L21C form, in non-reducing conditions, do not show a regain of the signal which confirms the role of the reducing agent in preventing the formation of disulphide bridges **(Fig. 3.22)**.

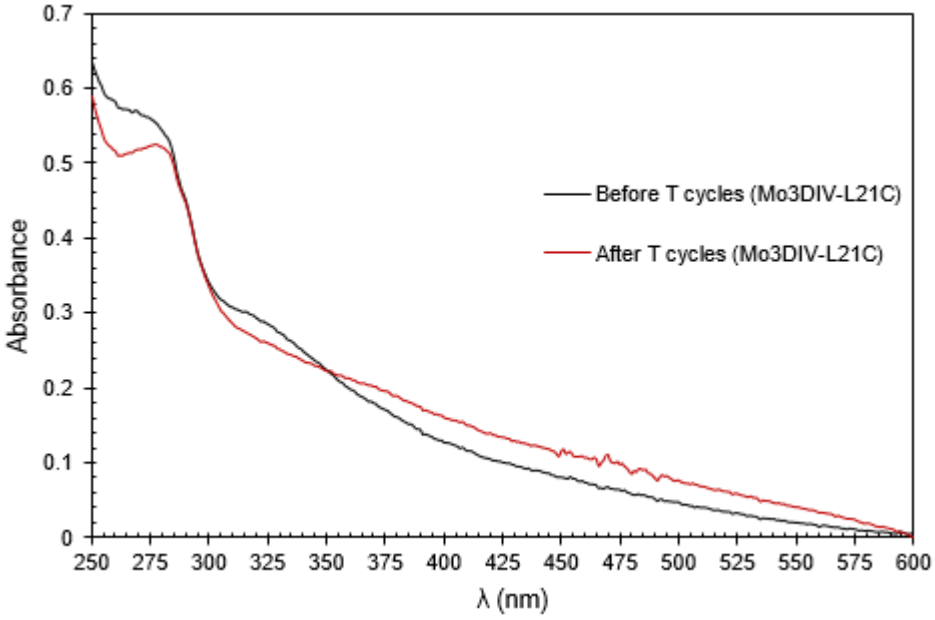

Figure 3.23. UV-vis spectra collected before and after the temperature ramp for the Mo-α$_3$DIV-L21C peptide ([peptide] = 70 μM).

3.4. Differential Scanning Calorimetry (DSC) characterization

DSC studies on the Mo-α$_3$DIV-L21C scaffold, under reducing conditions, was performed to study the peptide thermal stability and determine thermodynamic parameters, such as the melting temperature (T_m), the calorimetric enthalpy (ΔH_{cal}), the Van't Hoff enthalpy (ΔH_{vH}) and the $\Delta H_{van't\ Hoff}/\Delta H_{cal}$ ratio ($\Delta H_{vH}/\Delta H_{cal}$) [138,139,160]. The DSC thermograms of the Mo-peptide fitted well to a reversible monomeric (one-peak) two-state model. [161]

In TCEP-induced reducing conditions, the Mo-α$_3$DIV-L21C peptide exhibit a melting temperature of 66.1 ºC, a ΔH_{cal} value of 846.4 kJ.mol^{-1} (202.2 kcal.mol^{-1}) and a ΔH_{vH} value of 920.0 kJ.mol^{-1} (219.8 kcal.mol^{-1}) **(Fig. 3.24)**. The midpoint transition determined by the DSC technique is distinct from the ones estimated by the CD studies, which estimated a T_m of 60.3 (in the far-UV region) and 73.6 (in the visible region). The Tm value estimated, from DSC analysis, suggests that the tertiary structure starts undergoing an unfolding process in the temperature range from 60 – 70 ºC. Nevertheless, both CD and DSC techniques established a comparable monomeric two-state transition from a folded- to an unfolded-state.

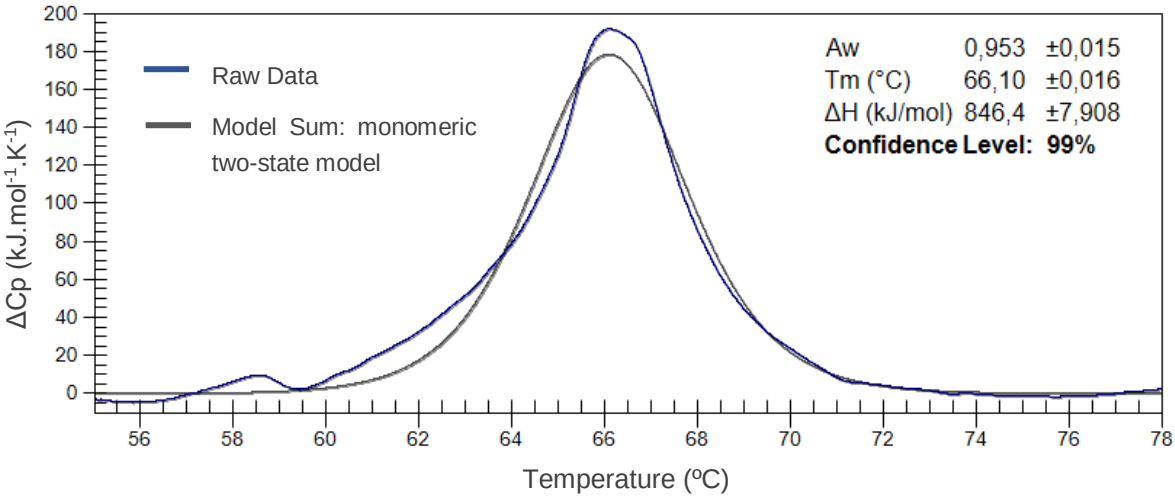

Figure 3.24. DSC thermogram of Mo-α$_3$DIV-L21C peptide (0.4 mg.mL^{-1}) in 50 mM phosphate buffer at pH 7.6, in the presence of 0.1 mM TCEP. The data was fitted, with a reversible one-peak two-state model, and visualised using the NanoAnalyse v3.10.0 software.

Furthermore, a $\Delta H_{van't\ Hoff}/\Delta H_{cal}$ ratio of 1.09 ($\Delta H_{vH}/\Delta H_{cal}$ = 1) further supports the unfolding process via a reversible monomeric two-state transition. However, a $\Delta H_{vH}/\Delta H_{cal}$ value > 1 may reveal or a small self-association upon temperature increasing, through inter-disulphide bridge formation, or an over-estimation of the peptide concentration **(Table. 3.5)** [138,139].

Table 3.5. Thermodynamic parameters estimated for the Mo-α$_3$DIV-L21C peptide in TCEP-induced reducing conditions.

	Sample	Tm (ºC)	ΔHcal (kJ.mol^{-1})	ΔHvH (kJ.mol^{-1})	$\Delta H_{vH}/\Delta H_{cal}$ ratio
With TCEP	**Mo-α$_3$DIV-L21C**	66.10	846.4	920.04	1.09

Unfortunately a DSC thermogram of the apo-α_3DIV-L21C scaffold, in the presence of reducing agent, was not obtained. The collect thermogram shows a large multiplicity of signals which preclude correct data fitting and, consequently, the determination of thermodynamic parameters **(Fig.3.25)**. This behaviour confirms that the tetracysteinyl environment has an important role in determining the arrangement of the tertiary structure. This obstacle may be sorted out by a titration test with different concentrations of the TCEP compound, in order to define the correct peptide: reducing agent stoichiometry without introducing experimental errors related with the contribution of the TCEP to the overall analysis of the thermodynamic parameters or with cross-reactions of the reducing agent with the phosphate buffer [162].

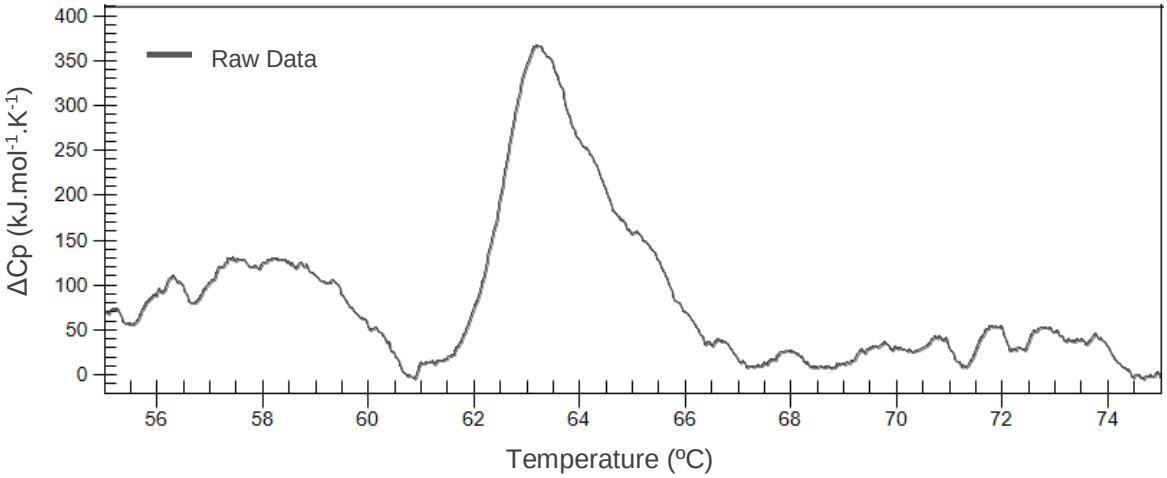

Figure 3.25. DSC thermogram of apo-α_3DIV-L21C peptide (0.5 mg.mL^{-1}) in 50 mM phosphate buffer at pH 7.6, in the presence of 0.1 mM TCEP. The data was visualised using the NanoAnalyse v3.10.0 software.

Previous studies of the incorporation of three heavy metal, such as Hg, Cd, and Pb, within the triscysteinyl site of the α_3DIV scaffold show an increase of the T_m values (18−24 °C) when the metal is coordinated, suggesting higher thermal stability for the metallated scaffolds [118]. Furthermore, the α_3DIV peptide displays a pH-dependent behaviour that impacts the determination of the thermodynamic parameters. In neutral pH (pH = 7) the α_3DIV peptide exhibit a midpoint transition at 64.4 ºC and in alkaline pH (pH = 8.2) exhibit at 60.2 ºC [118]. In the present case, a comparison between the apo- and Mo-peptide forms was not achieved and, consequently, a direct correlation, at this stage, of the effects of incorporation of a Mo atom, in the thermodynamic proprieties of the α_3DIV-L21C scaffold, it is inexact.

Nonetheless, this preliminary analysis demonstrates the role of the reducing agent in preventing the creation of several structural variants that difficult the analysis of the DSC data, due to oligomerization effects. Further DSC analysis of the apo-α_3DIV-L21C, in the presence of the reducing agent, must be made to enable a good correlation between the data from the α_3DIV and α_3DIV-L21C metallated and unmetallated systems.

3.5. Oxidation-state characterization: Reducing tests

Incubation studies were performed to assess the metal oxidation state when the Mo atom is coordinated in the tetracysteinyl environment of the α_3DIV-L21C scaffold. To test the reduction of the metal, three incubations were done using the reducing agents 1,4-dithiothreitol (DTT) and sodium ascorbate, under aerobic conditions, and sodium hydrosulphite (dithionite) in an anaerobic environment. The incubation test with ascorbate does not alter the UV-vis spectral profile of the Mo-peptide **(Fig.3.26)**, but the tests with 0.4 equivalents of DTT and 0.2 equivalents dithionite provided similar results **(Fig.3.27 and 3.28)**.

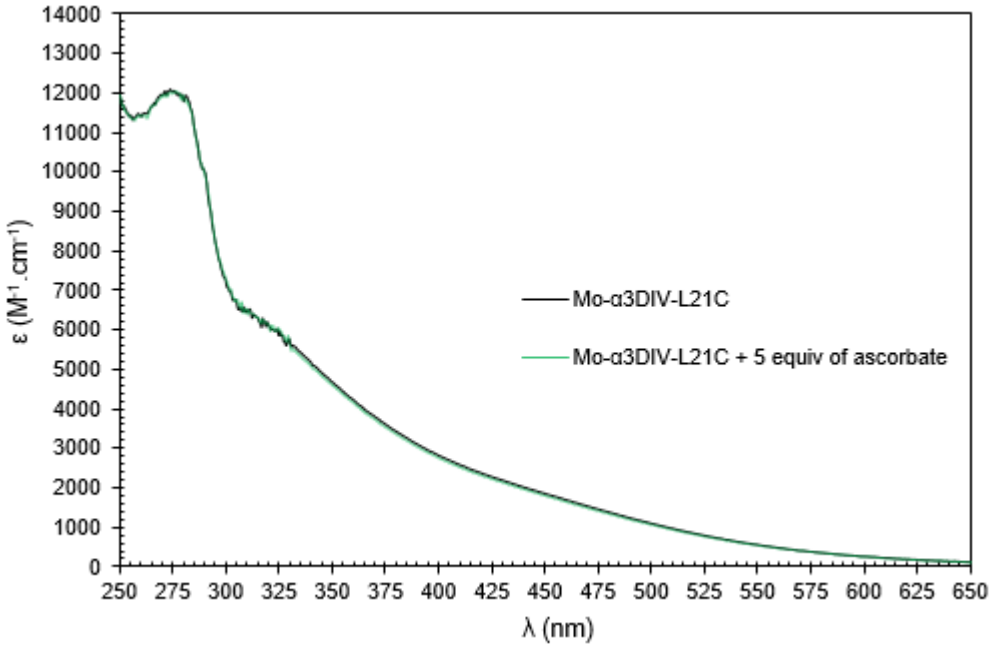

Figure 3.26. UV-visible spectra of the incubation test with 5 equivalents of sodium ascorbate, under aerobic conditions. The incubation was performed in 50mM Tris-HCl buffer at pH 7.6. Spectra were normalised to protein concentration.

An absorbance increase in the Mo-thiolate charge-transfer spectral region (300 – 340 nm) suggests a higher contribution of charge-transfer transitions. This increase may be a consequence of the metal reduction, from Mo(VI) to Mo(V), or additional coordination of the metal with a sulphur atom of an exogenous thiol compound [52,163,164]. The latter behaviour was also observed in the DTT-treated Mo-rubredoxin derivative, where the appearance of a UV-vis band at 336 nm (ε = 7.76 $mM^{-1}.cm^{-1}$) and at 460 nm (ε = 1.91 $mM^{-1}.cm^{-1}$) may suggest the coordination of sulphur from an exogenous thiol ligand in the Mo-centre [52].

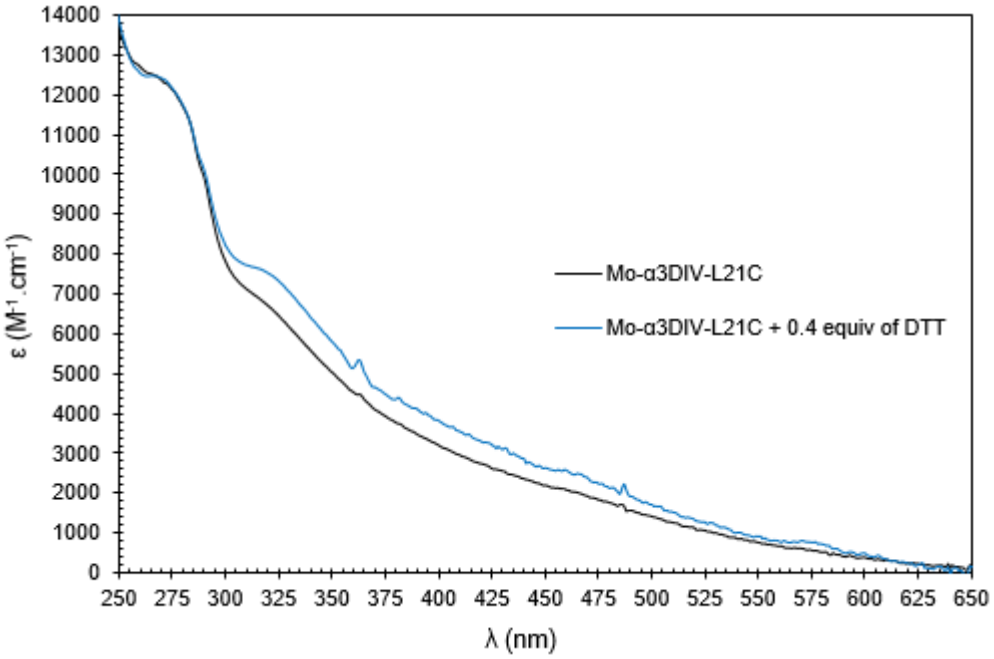

Figure 3.27. UV-visible spectra of the incubation test with 0.4 equivalents of DTT, under aerobic conditions. The incubation was performed in 50mM Tris-HCl buffer at pH 7.6. Spectra were normalised to protein concentration.

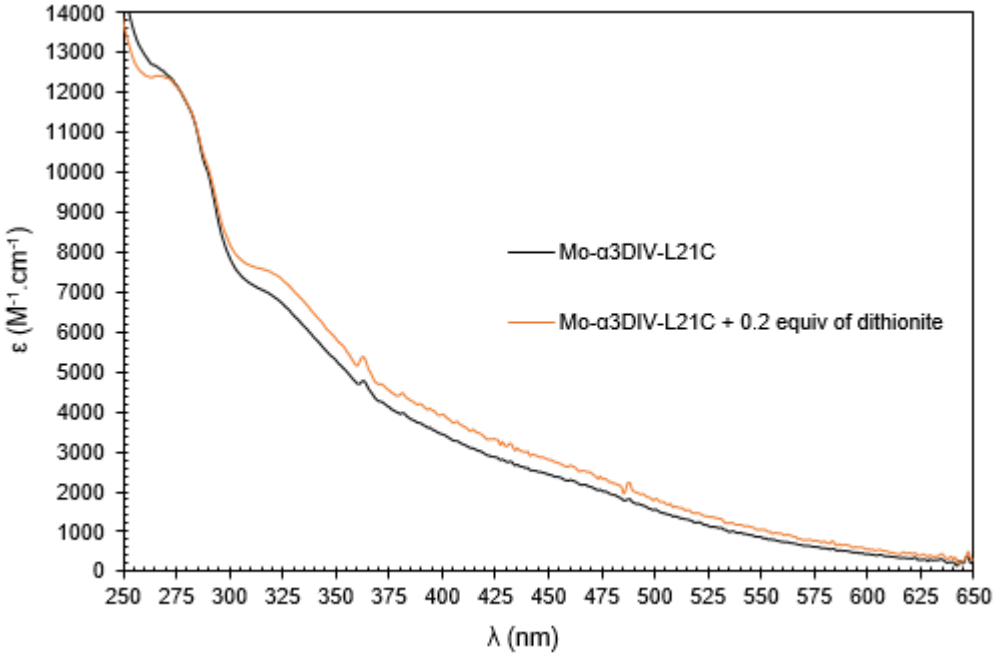

Figure 3.28. UV-visible spectra of the incubation test with 0.2 equivalents of sodium dithionite, under anaerobic conditions. The incubation was performed in 50mM Tris-HCl buffer at pH 7.6. Spectra were normalised to protein concentration.

By correlating these data with the electrochemical studies (in the next section), that estimated a midpoint potential of -406 mV vs. NHE at pH 7.6, these results suggest that DTT is not able to reduce the Mo atom since the reduction potential of DTT is -330 mV vs. NHE at pH 7 and, therefore, probably as in Rd the DTT is providing a transient additional coordination [165]. Contrarily, dithionite has a higher reducing power (-660 mV vs. NHE at pH = 7 [166]) than DTT, which indicate that the Mo-centre can only be reduced with dithionite. This interpretation is further supported by the fact that the UV-vis spectral profile of the Mo-α_3DIV-L21C scaffold remains identical when treated with 0.4 – 1.2 equivalents of DTT (data not shown). Conversely, the spectra of the dithionite-treated Mo-peptide starts to lose the intensity, in the Mo-thiolate charge-transfer region, when treated with more than 0.2 equivalents of dithionite (data not show). Ascorbate is a weaker reducing agent (282 mV vs. NHE [167]) so is not able to reduce the Mo-scaffold neither coordinate with the Mo atom.

Ultimately these results suggest that the Mo-centre can only be reduced by dithionite and not by DTT neither ascorbate. However, the DTT-treated Mo-α_3DIV-L21C peptide suggests plausible coordination of the sulphur atom of this exogenous thiol ligand with the Mo-centre, like observed in the DTT-treated Mo-Rd derivative [52]. Ultimately, the thiol-treated Mo-α_3DIV-L21C peptide may be proposed as a model for some periplasmatic nitrate reductases [168,169].

3.6. Electrochemical characterization: Cyclic Voltammetry (CV)

The electrochemical behaviour of the apo- and Mo-peptide forms, in TCEP-induced reducing conditions, was studied, through cyclic voltammetry (CV), to gain information on their redox properties. Preliminary electrochemical studies, in a thin-layer regime (limited diffusion, attained by the physically immobilization of the biomolecule with a membrane on the electrode surface), suggested that the Mo-α_3DIV-L21C scaffold exhibits a cathodic peak potential (E_{pc}) of -423 mV vs. NHE and an anodic peak potential (E_{pa}) of -389 mV vs. NHE. The voltammogram displays a quasi-reversible CV peak profile with a formal potential ($E^{0'}$) of -406 mV vs. NHE **(Fig. 3.29)**. This transition was assigned to the Mo(VI)/Mo(V) redox couple and, although slightly more positive, it is in agreement with the reduction potential determined for the Mo-substituted rubredoxin ($E^{0'}$ = -493 mV vs. NHE) [52]. Furthermore, some molybdoenzymes from the DMSOR family (Mo-*bis* PGD enzymes), such as the aldehyde oxidoreductase enzyme from *D. gigas*, also display a reduction potential of -415 mV and -539 mV vs. NHE for the Mo(VI)/Mo(V) and Mo(V)/Mo(IV) couples, respectively [170,171].

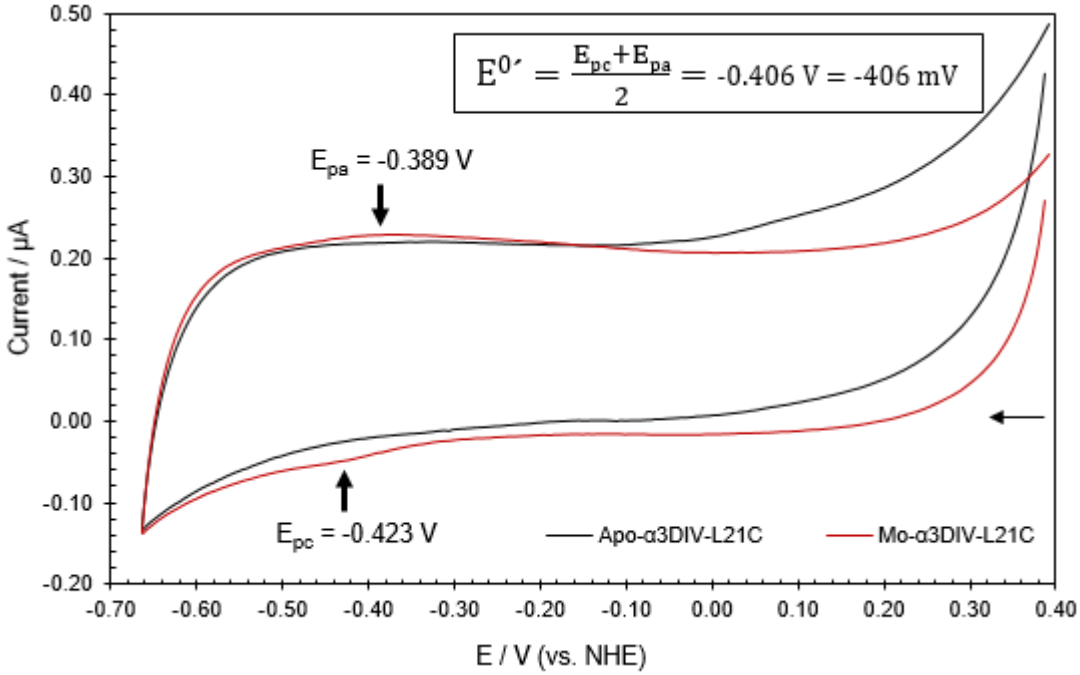

Figure 3.29. Normalised thin-layer cyclic voltammetry of the apo- and Mo-α_3DIV-L21C peptides (scan rate: 20 mV.s^{-1}; WE: pyrolytic carbon; RE: saturated calomel electrode (potentials converted to NHE reference scale); CE: platinum electrode; membrane cellulose 3.5 kDa cut-off; E_{oc} = -0.2 V; anaerobic chamber: $[O_2]_{max}$ = 3.5 ppm).

The redox pair peaks present a broad profile that may be the consequence of non-preferential protein orientation towards the electrode surface with the consequent low heterogeneous electronic constant rate (not calculated at this point) [172,173]. The α_3DIV-L21C scaffold presents a more negative superficial electrostatic charge, essentially in the metal-binding site region **(Fig. 3.30)**, which means that repulsion effects near the graphite electrode and the cellulose membrane (both also negative) may occur. This repulsive interaction may push away the negatively-charged Mo-Cys binding site in the opposite direction of the cellulose membrane, leading to a longer electronic pathway and consequently a low peak definition. The attempt to coat the electrode with a positive-charge electron transfer promoter (neomycin sulphate) was not successful in improving the voltammetric response and more assays should be performed in the future, such as using different electrode modifications.

Furthermore, the signal intensities for both processes are distinct. The current intensity (Ip_a) for the oxidation process (E_{pa} = -389 mV vs. NHE) was 0.0115 µA and for the reduction process (I_{pc}) (observed at E_{pc} = -423 mV vs. NHE) was 0.0221 µA. These results suggest that the molybdenum ion is initially in the +6 oxidation state within the α_3DIV-L21C scaffold. These results are further supported by a better peak definition in the reduction process, which indicates an easier metal reduction from the +6 to +5 oxidation state, than the opposite oxidation process. Further electrochemical studies are required to ensure an accurate determination of the $E^{0'}$ for

the Mo-α_3DIV-L21C peptide, namely using different techniques such as differential pulse voltammetry (DPV) or square-wave voltammetry (SWV).

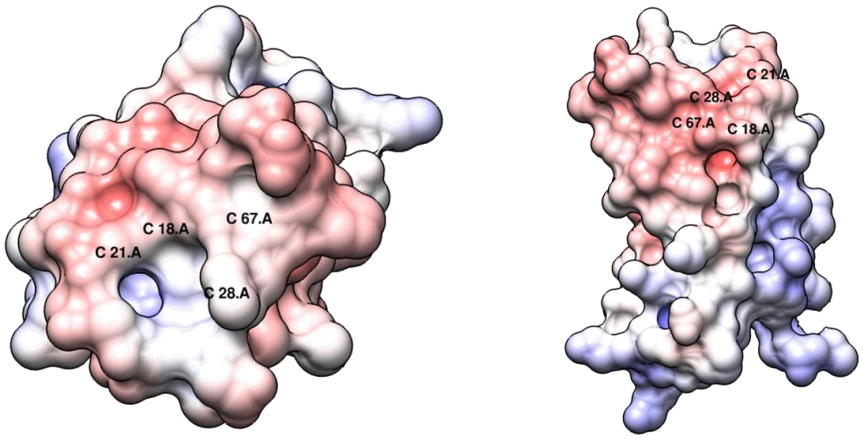

Figure 3.30. Surface electrostatic potential of the Mo-α_3DIV-L21C peptide. Negative potentials at red, neutral at white and positive at blue. The electrostatic potentials were calculated according to Coulomb's law and with Poisson-Boltzmann (PB) electrostatics calculations from Chimera 1.11.

4

Chapter 4. Conclusions

Over the past 30 years, the field of artificial enzymes is developing promptly. Accommodated in this area, *a de novo* protein design is a novel approach that exploits the construction of specific metal-binding sites using small-scaled, simple and stable synthetic peptide scaffolds, to mimic specific catalytic functions of complex metalloproteins and, ultimately, shed light on the dilemma of protein structure-function relationship.

The data reported confirmed the incorporation of a molybdenum atom within the rubredoxin-type centre of *a de novo* designed apo-α_3DIV-L21C three-helix bundle peptide. The metal incorporation in the tetracysteinyl active-site was assessed by the emerging of two broad absorption bands at 320 nm (ε_{320nm} = 7400 $M^{-1}.cm^{-1}$) and at 470 nm (ε_{470nm} = 2000 $M^{-1}.cm^{-1}$) upon the reconstitution procedure, which are specific of thiolate-Mo charge-transfer bands. The 1:1 peptide:metal ratio was estimated by metal and protein quantification. Moreover, CD studies in the visible region further corroborate the strong interaction between the peptide and the metal, by the appearance of a broad positive absorption band, with a maximum at 392 nm, that is absent in both CD spectra of the apo-peptide and TTM compound.

Furthermore, CD studies, in the far-UV region, under TCEP-induced reducing conditions, indicate a similar melting temperature for both apo- and Mo-α_3DIV-L21C peptides, at 60.0 ºC and 60.3 ºC respectively, and an equal α-helical structure conformation, suggesting that the Mo incorporation in the active-site do not have major repercussions in the secondary structure content. An enthalpy of folding (ΔH) of -100.6 $kJ.mol^{-1}$, for the apo-form, and of -80.9 $kJ.mol^{-1}$, for the Mo-form, attested the spontaneous folding process due to hydrophobic interactions, however, may suggest a slight destabilization imposed by the metal in the folding process.

Additionally, CD studies in the near-UV region reveal some deviations in the tertiary structure fingerprint for both apo- and Mo-peptides, with and without reducing agent, indicating small changes in the side-chain environment of the aromatic residues. The estimation of

thermodynamic parameters for the Mo-α_3DIV-L21C peptide, in the CD visible region, implying that the loss of the molybdenum atom in active-site occurs at higher temperatures (T_m = 73.6 ºC) and that the coordination of Mo within the metal-binding site is driven by a spontaneous process (ΔH = -125.9 kJ.mol^{-1}).

CD studies, under non-reducing conditions, reinforce the role of a reducing agent in promoting a slight destabilization of the tetracysteinyl environment. In the far-UV region, no stabilization plateau was achieved, and in the visible region, no regain in the visible signal upon temperature cooling was observed. These observations demonstrate that a reducing environment near the tetracysteinyl region prevents disulphide bridges formation and leads to a unique structural conformation that is slightly less stable. Without a reducing agent, the cysteine residues can covalently bind in a variety of arrangements, leading to several structural conformations, in the metal-binging site, that preserves the α-helical secondary structure and, ultimately, impose a more thermally-stable scaffold.

The thermal-stability of both apo- and Mo-forms were also evaluated by DSC analysis, under TCEP-induced reducing conditions. The data for the Mo-α_3DIV-L21C peptide fitted well to a reversible monomeric (one-peak) two-state model with a T_m of 66.1 ºC and a $\Delta H_{van't\ Hoff}/\Delta H_{cal}$ ratio of 1.09. The midpoint of the unfold transition in slightly different from the ones estimated from the CD analysis, but a $\Delta H_{vH}/\Delta H_{cal}$ ratio near 1 (one) suggest that the model fitted correctly the experimental data. The thermodynamic parameters for the apo-α_3DIV-L21C peptide were not estimated at this point, since the data shows a multiplicity of signals, from diverse structural conformations, even in slightly TCEP-induced reducing conditions.

Preliminary electrochemical analysis (using cyclic voltammetry in a thin-layer regime), suggest that the metal initial oxidation state is Mo(VI) within the tetracysteinyl active-site with a formal potential ($E^{0'}$) of -406 mV vs. NHE. The results suggest that the redox-active Mo-centre can undergo a one-electron transfer process (Mo(VI)/Mo(V)). Furthermore, incubations of the Mo-α_3DIV-L21C peptide with several reducing agents (ascorbate, DTT and dithionite) are in agreement with this hypothesis. Interestingly, an increment of the UV-vis spectral profile, in the thiolate-Mo charge-transfer region, upon incubation with DTT and dithionite may suggest additional coordination of the molybdenum atom with an exogenous thiol ligand, as observed in the Mo-substituted derivative from rubredoxin. [52]

Taking into consideration the assemble of results obtained, the reconstitution of the α_3DIV-L21C peptide with Mo can be considered an interesting structural model for the Mo-*bis* PDG enzymes, or DMSOR family, due to the nature of the ligands present in the first coordination sphere of Mo. At this moment, we speculate that the Mo-substituted scaffold harbours a Mo=O(OH)(–SCys)$_4$ centre since it displays spectroscopic properties similar to the ones in the active-site of the Mo-*bis* PDG enzymes.

4.1. Future Perspectives

In the future, further spectroscopic characterization and activity studies are envisaged in order to ensure that the novel Mo-α_3DIV-L21C peptide is a structural and functional analogue of some Mo-*bis* PGD enzymes. These spectroscopic studies will include electron paramagnetic resonance (EPR) spectroscopy and resonance Raman (RR) spectroscopy, that are essential to confirm the molybdenum oxidation state (in native and transient states) and define the redox process, within the tetracysteinyl environment, and to establish the first coordination sphere in the reconstituted Mo-peptide and in the thiol-treated Mo-peptide.

EPR is a suitable technique to follow the reduction of the oxidised Mo-α_3DIV-L21C scaffold with DTT and/or dithionite of the initial oxidation Mo(VI) state (EPR silent species) and the emergence of signals characteristics of the EPR active species Mo(V). Additionally, increasing the reduction time may attest if the Mo-tetracysteinyl centre can undergo a two-electron transfer reaction by the decreasing of the signal since the Mo(IV) species is EPR silent. [174]

Resonance Raman studies will add information on the first coordination sphere composition, assessed by the appearance of broad cysteinyl S-Mo(VI) charge transfer bands (at ~400 nm) and Mo-S stretching and bending vibrational modes (between ~300 – 400 cm^{-1}) [175]. Furthermore, the expansion of Mo coordination sphere with oxygen atoms and/or hydroxyl groups may also be evaluated by RR spectroscopy by the appearance of broad bands above 850 cm^{-1} typical of Mo=O symmetric stretching modes [176]. Ultimately, this expansion of Mo coordination number can be assessed and complemented by nuclear magnetic resonance (NMR) spectroscopy studies, using an active nuclei compound, such as the ^{19}F-active 2,2,2-tri-fluoroethanethiol (TFET), to confirm the binding of an exogenous thiol ligand in the active-site, resulting in a Mo=O(SR)(–SCys)$_4$ centre [177].

Magnetic circular dichroism (MCD) spectroscopy and additional electrochemical assays will complement the EPR studies. In addition, studies of the pH dependence behaviour of the Mo-α_3DIV-L21C scaffold and the binding affinity between the molybdenum and the peptide must be attained if possible.

Concluded the structural characterization studies, the capability of the metal active-site to undergo in a catalytic function must be inspected. The activity studies performed will depend on the metal first coordination sphere. For instances, with a Mo=O(OH)(–SCys)$_4$ moiety we can test the oxidation of arsenite to arsenate and/or the reduction dimethyl sulfoxide to dimethyl sulphide, to produce a model for the enzymes arsenite oxidase (*A. faecalis*) and dimethylsulfoxide reductase (*R. sphaeroides*), respectively. Diversely, the Mo=O(SR)(–SCys)$_4$ centre can be a model for the periplasmatic nitrate reductase (*E. coli*) or the polysulfide reductase (*T. thermophilus*) enzymes, by testing the reduction of nitrate to nitrite or the inorganic sulphur reduction to sulphide, respectively. Moreover, the possibility of developing a Mo=(SR)$_2$(–SCys)$_4$

moiety can further expand the models, such as for the oxidation of formate to carbon dioxide performed by the formate dehydrogenase (*R. capsulatus*).

5

Chapter 5. References

(1) Wackett, L. P.; Dodge, A. G.; Ellis, L. B. M. Microbial Genomics and the Periodic Table. *Applied and Environmental Microbiology*. **2004**, *70* (2), 647-655. https://doi.org/10.1128/AEM.70.2.647-655.2004.

(2) Daumann, L. J. Essential and Ubiquitous: The Emergence of Lanthanide Metallobiochemistry. *Angew. Chemie Int. Ed.* **2019**, *58* (37), 12795-12802. https://doi.org/10.1002/anie.201904090.

(3) Williams, R. J. P. Systems Biology of Evolution: The Involvement of Metal Ions. *BioMetals* **2007**, *20* (2), 107-112. https://doi.org/10.1007/s10534-007-9087-6.

(4) Monosson, E. *Evolution in a Toxic World: How Life Responds to Chemical Threats*; **2012**. https://doi.org/10.5822/978-1-61091-221-1.

(5) Lippard, S. J. The Interface of Inorganic Chemistry and Biology. *Journal of the American Chemical Society*. **2010**, *132* (42), 14689-14693. https://doi.org/10.1021/ja108523h.

(6) Lippard, S. J. The Inorganic Side of Chemical Biology. *Nature Chemical Biology*. **2006**, *2* (10), 504-507. https://doi.org/10.1038/nchembio1006-504.

(7) David, S. S.; Meggers, E. Inorganic Chemical Biology: From Small Metal Complexes in Biological Systems to Metalloproteins. *Current Opinion in Chemical Biology*. **2008**, *12* (2), 194-196. https://doi.org/10.1016/j.cbpa.2008.03.008.

(8) Andreini, C.; Bertini, I.; Cavallaro, G.; Holliday, G. L.; Thornton, J. M. Metal Ions in Biological Catalysis: From Enzyme Databases to General Principles. *J. Biol. Inorg. Chem.* **2008**, *13* (8), 1205-1218. https://doi.org/10.1007/s00775-008-0404-5.

(9) Holm, R. H.; Kennepohl, P.; Solomon, E. I. Structural and Functional Aspects of Metal Sites in Biology. *Chem. Rev.* **1996**, *96* (7), 2239-2314. https://doi.org/10.1021/cr9500390.

(10) Nanda, V.; Koder, R. L. Designing Artificial Enzymes by Intuition and Computation. *Nat. Chem.* **2010**, *2* (1), 15–24. https://doi.org/10.1038/nchem.473.

(11) Sharma, V.; Bachwani, M. Artificial Enzymes: A Review. *Curr. Enzym. Inhib.* **2011**, *7* (3), 178–189. https://doi.org/10.2174/157340811798807623.

(12) Motherwell, W. B.; Bingham, M. J.; Six, Y. Recent Progress in the Design and Synthesis of Artificial Enzymes. *Tetrahedron*. **2001**, *57* (22), 4663-4686. https://doi.org/10.1016/S0040-4020(01)00288-5.

(13) Breslow, R. Artificial Enzymes. *Science.* **1982**, *218* (4572), 532–537.

https://doi.org/10.1002/3527606645.

(14) Murakami, Y.; Kikuchi, J.; Hisaeda, Y.; Hayashida, O. Artificial Enzymes. *Chem. Rev.* **1996**, *96* (2), 721–758. https://doi.org/10.1021/cr9403704.

(15) Regan, L. Protein Design. *Curr. Opin. Biotechnol.* **1991**, *2* (4), 544–550. https://doi.org/10.1016/0958-1669(91)90079-K.

(16) Dill, K. A.; Ozkan, S. B.; Shell, M. S.; Weikl, T. R. The Protein Folding Problem. *Annu. Rev. Biophys.* **2008**, *37*, 289–316. https://doi.org/10.1146/annurev.biophys.37.092707.153558.

(17) Plegaria, J. S.; Pecoraro, V. L. Sculpting Metal-Binding Environments in de Novo Designed Three-Helix Bundles. *Isr. J. Chem.* **2015**, *55* (1), 85–95. https://doi.org/10.1002/ijch.201400146.

(18) Peacock, A. F. A. Incorporating Metals into de Novo Proteins. *Curr. Opin. Chem. Biol.* **2013**, *17* (6), 934–939. https://doi.org/10.1016/j.cbpa.2013.10.015.

(19) Doerr, A. J.; McLendon, G. L. Design, Folding, and Activities of Metal-Assembled Coiled Coil Proteins. *Inorg. Chem.* **2004**, *43* (25), 7916–7925. https://doi.org/10.1021/ic0490573.

(20) Lu, Y.; Berry, S. M.; Pfister, T. D. Engineering Novel Metalloproteins: Design of Metal-Binding Sites into Native Protein Scaffolds. *Chem. Rev.* **2001**, *101* (10), 3047–3080. https://doi.org/10.1021/cr0000574.

(21) Hong, J.; Kharenko, O. A.; Ogawa, M. Y. Incorporating Electron-Transfer Functionality into Synthetic Metalloproteins from the Bottom-Up. *Inorg. Chem.* **2006**, *45* (25), 9974–9984. https://doi.org/10.1021/ic060222j.

(22) Zastrow, M. L.; Pecoraro, V. L. Designing Functional Metalloproteins: From Structural to Catalytic Metal Sites. *Coord. Chem. Rev.* **2013**, *257* (17–18), 2565–2588. https://doi.org/10.1016/j.ccr.2013.02.007.

(23) Barker, P. D. Designing Redox Metalloproteins from Bottom-up and Top-down Perspectives. *Curr. Opin. Struct. Biol.* **2003**, *13* (4), 490–499. https://doi.org/10.1016/S0959-440X(03)00108-8.

(24) Yu, F.; Cangelosi, V. M.; Zastrow, M. L.; Tegoni, M.; Plegaria, J. S.; Tebo, A. G.; Mocny, C. S.; Ruckthong, L.; Qayyum, H.; Pecoraro, V. L. Protein Design: Toward Functional Metalloenzymes. *Chem. Rev.* **2014**, *114* (7), 3495–3578. https://doi.org/10.1021/cr400458x.

(25) Petrik, I. D.; Liu, J.; Lu, Y. Metalloenzyme Design and Engineering through Strategic Modifications of Native Protein Scaffolds. *Curr. Opin. Chem. Biol.* **2014**, *19* (1), 67–75. https://doi.org/10.1016/j.cbpa.2014.01.006.

(26) Pordea, A. Metal-Binding Promiscuity in Artificial Metalloenzyme Design. *Curr. Opin. Chem. Biol.* **2015**, *25*, 124–132. https://doi.org/10.1016/j.cbpa.2014.12.035.

(27) Kazlauskas, R. J. Enhancing Catalytic Promiscuity for Biocatalysis. *Curr. Opin. Chem. Biol.* **2005**, *9* (2), 195–201. https://doi.org/10.1016/j.cbpa.2005.02.008.

(28) Fruk, L.; Kuo, C. H.; Torres, E.; Niemeyer, C. M. Apoenzyme Reconstitution as a Chemical Tool for Structural Enzymology and Biotechnology. *Angew. Chemie - Int. Ed.* **2009**, *48* (9), 1550–1574. https://doi.org/10.1002/anie.200803098.

(29) Moura, I.; Pereira, A. S.; Tavares, P.; Moura, J. J. G. Simple and Complex Iron-Sulfur Proteins in Sulfate Reducing Bacteria. *Adv. Inorg. Chem.* **1999**, *47* (C), 361–419. https://doi.org/10.1016/S0898-8838(08)60083-5.

(30) Sieker, L. C.; Stenkamp, R. E.; Legall, J. Rubredoxin in Crystalline State. *Methods Enzymol.* **1994**, *243* (C), 203–216. https://doi.org/10.1016/0076-6879(94)43016-0.

(31) Swartz, P. D.; Beck, B. W.; Ichiye, T. Structural Origins of Redox Potentials in Fe-s Proteins:

Electrostatic Potentials of Crystal Structures. *Biophys. J.* **1996**, *71* (6), 2958–2969. https://doi.org/10.1016/S0006-3495(96)79533-4.

(32) Swartz, P. D.; Ichiye, T. Protein Contributions to Redox Potentials of Homologous Rubredoxins: An Energy Minimization Study. *Biophys. J.* **1997**, *73* (5), 2733–2741. https://doi.org/10.1016/S0006-3495(97)78302-4.

(33) Brown, R. S.; Sander, C.; Argos, P. The Primary Structure of Transcription Factor TFIIIA Has 12 Consecutive Repeats. *FEBS Lett.* **1985**, *186* (2), 271–274. https://doi.org/10.1016/0014-5793(85)80723-7.

(34) Miller, J.; McLachlan, A. D.; Klug, A. Repetitive Zinc-Binding Domains in the Protein Transcription Factor IIIA from Xenopus Oocytes. *J. Trace Elem. Exp. Med.* **2001**, *14* (2), 157–169. https://doi.org/10.1002/jtra.1022.

(35) Vignais, P. M.; Billoud, B. Occurrence, Classification, and Biological Function of Hydrogenases: An Overview. *Chem. Rev.* **2007**, *107* (10), 4206–4272. https://doi.org/10.1021/cr050196r.

(36) Cammack, R. Hydrogenase Sophistication. *Nature* **1999**, *397* (6716), 214–215. https://doi.org/10.1038/16601.

(37) Rosenzweig, A. C. Metallochaperones. *Chem. Biol.* **2002**, *9* (6), 673–677. https://doi.org/10.1016/s1074-5521(02)00156-4.

(38) Harrison, M. D.; Jones, C. E.; Dameron, C. T. Copper Chaperones: Function, Structure and Copper-Binding Properties. *J. Biol. Inorg. Chem.* **1999**, *4* (2), 145–153. https://doi.org/10.1007/s007750050297.

(39) Zaballa, M. E.; Abriata, L. A.; Donaire, A.; Vila, A. J. Flexibility of the Metal-Binding Region in Apo-Cupredoxins. *Proc. Natl. Acad. Sci. U. S. A.* **2012**, *109* (24), 9254–9259. https://doi.org/10.1073/pnas.1119460109.

(40) Solomon, E. I.; Szilagyi, R. K.; DeBeer George, S.; Basumallick, L. Electronic Structures of Metal Sites in Proteins and Models: Contributions to Function in Blue Copper Proteins. *Chem. Rev.* **2004**, *104* (2), 419–458. https://doi.org/10.1021/cr0206317.

(41) Tunney, J. M.; McMaster, J.; Garner, C. D. *Molybdenum and Tungsten Enzymes*; 2004; Vol. 8. https://doi.org/10.1016/B0-08-043748-6/08168-8.

(42) Vrajmasu, V. V.; Bominaar, E. L.; Meyer, J.; Münck, E. Mössbauer Study of Reduced Rubredoxin as Purified and in Whole Cells. Structural Correlation Analysis of Spin Hamiltonian Parameters. *Inorg. Chem.* **2002**, *41* (24), 6358–6371. https://doi.org/10.1021/ic020508y.

(43) Maher, M.; Cross, M.; Wilce, M. C. J.; Guss, J. M.; Wedd, A. G. Metal-Substituted Derivatives of the Rubredoxin from Clostridium Pasteurianum. *Acta Crystallogr. Sect. D Biol. Crystallogr.* **2004**, *60* (2), 298–303. https://doi.org/10.1107/S090744490302794X.

(44) Slater, J. W.; Shafaat, H. S. Nickel-Substituted Rubredoxin as a Minimal Enzyme Model for Hydrogenase. *J. Phys. Chem. Lett.* **2015**, *6* (18), 3731–3736. https://doi.org/10.1021/acs.jpclett.5b01750.

(45) Slater, J. W.; Marguet, S. C.; Monaco, H. A.; Shafaat, H. S. Going beyond Structure: Nickel-Substituted Rubredoxin as a Mechanistic Model for the [NiFe] Hydrogenases. *J. Am. Chem. Soc.* **2018**, *140* (32), 10250–10262. https://doi.org/10.1021/jacs.8b05194.

(46) Thapper, A.; Rizzi, A. C.; Brondino, C. D.; Wedd, A. G.; Pais, R. J.; Maiti, B. K.; Moura, I.; Pauleta, S. R.; Moura, J. J. G. Copper-Substituted Forms of the Wild Type and C42A Variant of Rubredoxin. *J. Inorg. Biochem.* **2013**, *127*, 232–237. https://doi.org/10.1016/j.jinorgbio.2013.06.003.

(47) Maiti, B. K.; Maia, L. B.; Moro, A. J.; Lima, J. C.; Cordas, C. M.; Moura, I.; Moura, J. J. G. Unusual Reduction Mechanism of Copper in Cysteine-Rich Environment. *Inorg. Chem.* **2018**, *57* (14), 8078–8088. https://doi.org/10.1021/acs.inorgchem.8b00121.

(48) Dauter, Z.; Wilson, K. S.; Sieker, L. C.; Moulis, J. M.; Meyer, J. Zinc- and Iron-Rubredoxins from Clostridium Pasteurianum at Atomic Resolution: A High-Precision Model of a ZnS4 Coordination Unit in a Protein. *Proc. Natl. Acad. Sci. U. S. A.* **1996**, *93* (17), 8836–8840. https://doi.org/10.1073/pnas.93.17.8836.

(49) Petillot, Y.; Forest, E.; Mathieu, I.; Meyer, J.; Moulis, J. M. Analysis, by Electrospray Ionization Mass Spectrometry, of Several Forms of Clostridium Pasteurianum Rubredoxin. *Biochem. J.* **1993**, *296* (3), 657–661. https://doi.org/10.1042/bj2960657.

(50) Archer, M.; Carvalho, A. L.; Teixeira, S.; Moura, I.; Moura, J. J. G.; Rusnak, F.; Romão, M. J. Structural Studies by X-Ray Diffraction on Metal Substituted Desulforedoxin, a Rubredoxin-Type Protein. *Protein Sci.* **1999**, *8* (7), 1536–1545. https://doi.org/10.1110/ps.8.7.1536.

(51) LeMaster, D. M.; Minnich, M.; Parsons, P. J.; Anderson, J. S.; Hernández, G. Tetrathiolate Coordination of Germanium(IV) in a Protein Active Site. *J. Inorg. Biochem.* **2006**, *100* (8), 1410–1412. https://doi.org/10.1016/j.jinorgbio.2006.03.014.

(52) Maiti, B. K.; Maia, L. B.; Silveira, C. M.; Todorovic, S.; Carreira, C.; Carepo, M. S. P.; Grazina, R.; Moura, I.; Pauleta, S. R.; Moura, J. J. G. Incorporation of Molybdenum in Rubredoxin: Models for Mononuclear Molybdenum Enzymes. *J. Biol. Inorg. Chem.* **2015**, *20* (5), 821–829. https://doi.org/10.1007/s00775-015-1268-0.

(53) Conrads, T.; Hemann, C.; George, G. N.; Pickering, I. J.; Prince, R. C.; Hille, R. The Active Site of Arsenite Oxidase from Alcaligenes Faecalis. *J. Am. Chem. Soc.* **2002**, *124* (38), 11276–11277. https://doi.org/10.1021/ja027684q.

(54) Mitchell, P. C. H. Coordination Compounds of Molybdenum. *Coord. Chem. Rev.* **1966**, *1* (3), 315–350. https://doi.org/10.1016/S0010-8545(00)80143-5.

(55) Zhang, Y.; Gladyshev, V. N. Molybdoproteomes and Evolution of Molybdenum Utilization. *J. Mol. Biol.* **2008**, *379* (4), 881–899. https://doi.org/10.1016/j.jmb.2008.03.051.

(56) Williams, R. J. P.; Fraústo da Silva, J. J. R. The Involvement of Molybdenum in Life. *Biochem. Biophys. Res. Commun.* **2002**, *292* (2), 293–299. https://doi.org/10.1006/bbrc.2002.6518.

(57) Wang, D. Redox Chemistry of Molybdenum in Natural Waters and Its Involvement in Biological Evolution. *Front. Microbiol.* **2012**, *3* (DEC), 1–7. https://doi.org/10.3389/fmicb.2012.00427.

(58) Mendel, R. R. Molybdenum: Biological Activity and Metabolism. *Dalt. Trans.* **2005**, No. 21, 3404–3409. https://doi.org/10.1039/b505527j.

(59) Sigel, A.; Sigel, H. *Metal Ions in Biological Systems, Volume 35: Iron Transport and Storage Microorganisms, Plants, and Animals*; 1998; Vol. 5. https://doi.org/10.1155/mbd.1998.262a.

(60) Basu, P.; Burgmayer, S. J. N. Recent Developments in the Study of Molybdoenzyme Models. *J. Biol. Inorg. Chem.* **2015**, *20* (2), 373–383. https://doi.org/10.1007/s00775-014-1228-0.

(61) Majumdar, A. Structural and Functional Models in Molybdenum and Tungsten Bioinorganic Chemistry: Description of Selected Model Complexes, Present Scenario and Possible Future Scopes. *Dalt. Trans.* **2014**, *43* (24), 8990–9003. https://doi.org/10.1039/c4dt00631c.

(62) Aguilar, M.; Kalakoutskii, K.; Cárdenas, J.; Fernández, E. Direct Transfer of Molybdopterin Cofactor to Aponitrate Reductase from a Carrier Protein in Chlamydomonas Reinhardtii. *FEBS Lett.* **1992**, *307* (2), 162–163. https://doi.org/10.1016/0014-5793(92)80758-9.

(63) Hagen, W. R. Cellular Uptake of Molybdenum and Tungsten. *Coordination Chemistry Reviews*. **2011**, *255* (9-10), 1117-1128. https://doi.org/10.1016/j.ccr.2011.02.009.

(64) Tejada-Jiménez, M.; Llamas, Á.; Sanz-Luque, E.; Galván, A.; Fernández, E. A High-Affinity Molybdate Transporter in Eukaryotes. *Proc. Natl. Acad. Sci. U. S. A.* **2007**, *104* (50), 20126-20130. https://doi.org/10.1073/pnas.0704646104.

(65) Biswas, K. C.; Woodards, N. A.; Xu, H.; Barton, L. L. Reduction of Molybdate by Sulfate-Reducing Bacteria. *BioMetals* **2009**, *22* (1), 131–139. https://doi.org/10.1007/s10534-008-9198-8.

(66) Hille, R.; Hall, J.; Basu, P. The Mononuclear Molybdenum Enzymes. *Chemical Reviews*. **2014**, *114* (7), 3963-4038. https://doi.org/10.1021/cr400443z.

(67) Rajapakshe, A.; Snyder, R. A.; Astashkin, A. V.; Bernardson, P.; Evans, D. J.; Young, C. G.; Evans, D. H.; Enemark, J. H. Insights into the Nature of Mo(V) Species in Solution: Modeling Catalytic Cycles for Molybdenum Enzymes. *Inorganica Chim. Acta* **2009**, *362* (12), 4603-4608. https://doi.org/10.1016/j.ica.2009.05.040.

(68) Hoffman, B. M.; Lukoyanov, D.; Yang, Z. Y.; Dean, D. R.; Seefeldt, L. C. Mechanism of Nitrogen Fixation by Nitrogenase: The next Stage. *Chemical Reviews*. **2014**, *114* (8), 4041-4062. https://doi.org/10.1021/cr400641x.

(69) Rees, D. C.; Tezcan, F. A.; Haynes, C. A.; Walton, M. Y.; Andrade, S.; Einsle, O.; Howard, J. B. Structural Basis of Biological Nitrogen Fixation. *Philosophical Transactions of the Royal Society A: Mathematical, Physical and Engineering Sciences*. **2005**, *363* (1829), 971-984. https://doi.org/10.1098/rsta.2004.1539.

(70) George, G. N.; Pickering, I. J.; Yu, E. Y.; Prince, R. C.; Bursakov, S. A.; Gavel, O. Y.; Moura, I.; Moura, J. J. G. A Novel Protein-Bound Copper - Molybdenum Cluster [12]. *Journal of the American Chemical Society*. **2000**, *122* (34), 8321-8322. https://doi.org/10.1021/ja000955h.

(71) Bursakov, S. A.; Gavel, O. Y.; Di Rocco, G.; Lampreia, J.; Calvete, J.; Pereira, A. S.; Moura, J. J. G.; Moura, I. Antagonists Mo and Cu in a Heterometallic Cluster Present on a Novel Protein (Orange Protein) Isolated from *Desulfovibrio Gigas*. In *Journal of Inorganic Biochemistry*; **2004**, *98*, 833-840. https://doi.org/10.1016/j.jinorgbio.2003.12.002.

(72) Rivas, M. G.; Carepo, M. S. P.; Mota, C. S.; Korbas, M.; Durand, M. C.; Lopes, A. T.; Brondino, C. D.; Pereira, A. S.; George, G. N.; Dolla, A.; et al. Molybdenum Induces the Expression of a Protein Containing a New Heterometallic Mo-Fe Cluster in *Desulfovibrio Alaskensis*. *Biochemistry* **2009**, *48* (5), 873-882. https://doi.org/10.1021/bi801773t.

(73) Brondino, C. D.; Romão, M. J.; Moura, I.; Moura, J. J. G. Molybdenum and Tungsten Enzymes: The Xanthine Oxidase Family. *Current Opinion in Chemical Biology*. **2006**, *10* (2), 109-114. https://doi.org/10.1016/j.cbpa.2006.01.034.

(74) Iobbi-Nivol, C.; Leimkühler, S. Molybdenum Enzymes, Their Maturation and Molybdenum Cofactor Biosynthesis in *Escherichia Coli*. *Biochimica et Biophysica Acta - Bioenergetics*. **2013**, *1827* (8-9), 1086-1101. https://doi.org/10.1016/j.bbabio.2012.11.007.

(75) Williams, B. R.; Fu, Y.; Yap, G. P. A.; Burgmayer, S. J. N. Structure and Reversible Pyran Formation in Molybdenum Pyranopterin Dithiolene Models of the Molybdenum Cofactor. *J. Am. Chem. Soc.* **2012**, *134* (48), 19584-19587. https://doi.org/10.1021/ja310018e.

(76) Sugimoto, H.; Tsukube, H. Chemical Analogues Relevant to Molybdenum and Tungsten Enzyme Reaction Centres toward Structural Dynamics and Reaction Diversity. *Chem. Soc. Rev.* **2008**, *37* (12), 2609-2619. https://doi.org/10.1039/b610235m.

(77) Rothery, R. A.; Stein, B.; Solomonson, M.; Kirk, M. L.; Weiner, J. H. Pyranopterin Conformation Defines the Function of Molybdenum and Tungsten Enzymes. *Proc. Natl. Acad. Sci. U. S. A.* **2012**, *109* (37), 14773-14778. https://doi.org/10.1073/pnas.1200671109.

(78) Donahue, J. P.; Goldsmith, C. R.; Nadiminti, U.; Holm, R. H. Synthesis, Structures, and Reactivity of Bis(Dithiolene)Molybdenum(IV,VI) Complexes Related to the Active Sites of Molybdoenzymes. *J. Am. Chem. Soc.* **1998**, *120* (49), 12869-12881. https://doi.org/10.1021/ja982914f.

(79) Majumdar, A.; Pal, K.; Sarkar, S. Necessity of Fine Tuning in Mo(Iv) Bis(Dithiolene) Complexes to Warrant Nitrate Reduction. *Dalt. Trans.* **2009**, *11*, 1927-1938. https://doi.org/10.1039/b815436h.

(80) Booyong Shim Lim; Holm, R. H. Bis(Dithiolene)Molybdenum Analogues Relevant to the DMSO Reductase Enzyme Family: Synthesis, Structures, and Oxygen Atom Transfer Reactions and Kinetics. *J. Am. Chem. Soc.* **2001**, *123* (9), 1920-1930. https://doi.org/10.1021/ja003546u.

(81) Wang, J. J.; Kryatova, O. P.; Rybak-Akimova, E. V.; Holm, R. H. Comparative Kinetics and Mechanism of Oxygen and Sulfur Atom Transfer Reactions Mediated by Bis(Dithiolene) Complexes of Molybdenum and Tungsten. *Inorg. Chem.* **2004**, *43* (25), 8092-8101. https://doi.org/10.1021/ic040087f.

(82) Sung, K. M.; Holm, R. H. Substitution and Oxidation Reactions of Bis(Dithiolene)Tungsten Complexes of Potential Relevance to Enzyme Sites. *Inorg. Chem.* **2001**, *40* (18), 4518-4525. https://doi.org/10.1021/ic010421x.

(83) Pushie, M. J.; George, G. N. Spectroscopic Studies of Molybdenum and Tungsten Enzymes. *Coordination Chemistry Reviews*. **2011**, *255* (9-10), 1055-1084. https://doi.org/10.1016/j.ccr.2011.01.056.

(84) Joshi, H. K.; Cooney, J. J. A.; Inscore, F. E.; Gruhn, N. E.; Lichtenberger, D. L.; Enemark, J. H. Investigation of Metal-Dithiolate Fold Angle Effects: Implications for Molybdenum and Tungsten Enzymes. *Proc. Natl. Acad. Sci. U. S. A.* **2003**, *100* (7), 3719-3724. https://doi.org/10.1073/pnas.0636832100.

(85) Wiebelhaus, N. J.; Cranswick, M. A.; Klein, E. L.; Lockett, L. T.; Lichtenberger, D. L.; Enemark, J. H. Metal-Sulfur Valence Orbital Interaction Energies in Metal-Dithiolene Complexes: Determination of Charge and Overlap Interaction Energies by Comparison of Core and Valence Ionization Energy Shifts. *Inorg. Chem.* **2011**, *50* (21), 11021-11031. https://doi.org/10.1021/ic201566n.

(86) Carepo, M. S. P.; Carreira, C.; Grazina, R.; Zakrzewska, M. E.; Dolla, A.; Aubert, C.; Pauleta, S. R.; Moura, J. J. G.; Moura, I. Orange Protein from *Desulfovibrio Alaskensis G20*: Insights into the Mo-Cu Cluster Protein-Assisted Synthesis. *J. Biol. Inorg. Chem.* **2016**, *21* (1), 53-62. https://doi.org/10.1007/s00775-015-1323-x.

(87) Carepo, M. S. P.; Pauleta, S. R.; Wedd, A. G.; Moura, J. J. G.; Moura, I. Mo–Cu Metal Cluster Formation and Binding in an Orange Protein Isolated from *Desulfovibrio Gigas*. *JBIC J. Biol. Inorg. Chem.* **2014**, *19* (4-5), 605-614. https://doi.org/10.1007/s00775-014-1107-8.

(88) Maiti, B. K.; Maia, L. B.; Pauleta, S. R.; Moura, I.; Moura, J. J. G. Protein-Assisted Formation of Molybdenum Heterometallic Clusters: Evidence for the Formation of S2MoS2-M-S2MoS2 Clusters with M = Fe, Co, Ni, Cu, or Cd within the Orange Protein. *Inorg. Chem.* **2017**, *56* (4), 2210-2220. https://doi.org/10.1021/acs.inorgchem.6b02906.

(89) Laurie, S. H. Thiomolybdates — Simple but Very Versatile Reagents. *Eur. J. Inorg. Chem.* **2000**, *2000* (12), 2443. https://doi.org/10.1002/1099-0682(200012)2000:12<2443::aid-ejic2443>3.3.co;2-9.

(90) Mellor, J. W. A Comprehensive Treatise on Inorganic and Theoretical Chemistry. *Arch. Radiol. Electrother.* **1922**. https://doi.org/10.1259/are.1922.0042.

(91) Müller, A.; Diemann, E.; Jostes, R.; Bögge, H. Transition Metal Thiometalates: Properties and Significance in Complex and Bioinorganic Chemistry. *Angew. Chemie Int. Ed. English* **1981**, *20* (11), 934–955. https://doi.org/10.1002/anie.198109341.

(92) Quagraine, E. K.; Reid, R. S. UV/Visible Spectrophotometric Studies of the Interactions of Thiomolybdates, Copper(II) and Other Ligands. *J. Inorg. Biochem.* **2001**, *85* (1), 53–60. https://doi.org/10.1016/S0162-0134(00)00223-3.

(93) Brewer, G. J.; Askari, F.; Lorincz, M. T.; Carlson, M.; Schilsky, M.; Kluin, K. J.; Hedera, P.; Moretti, P.; Fink, J. K.; Tankanow, R.; et al. Treatment of Wilson Disease With Ammonium Tetrathiomolybdate. *Arch. Neurol.* **2006**, *63* (4), 521. https://doi.org/10.1001/archneur.63.4.521.

(94) Perez, E. A.; Hillman, D. W.; Fishkin, P. A.; Krook, J. E.; Tan, W. W.; Kuriakose, P. A.; Alberts, S. R.; Dakhil, S. R. Phase II Trial of Dolastatin-10 in Patients with Advanced Breast Cancer. *Invest. New Drugs* **2005**, *23* (3), 257–261. https://doi.org/10.1007/s10637-005-6735-y.

(95) DeGrado, W. F.; Summa, C. M.; Pavone, V.; Nastri, F.; Lombardi, A. De Novo Design and Structural Characterization of Proteins and Metalloproteins. *Annu. Rev. Biochem.* **1999**, *68*, 779-819. https://doi.org/10.1146/annurev.biochem.68.1.779.

(96) Beasley, J. R.; Hecht, M. H. Protein Design: The Choice of de Novo Sequences. *Journal of Biological Chemistry*. **1997**, *272* (4), 2031-2034. https://doi.org/10.1074/jbc.272.4.2031.

(97) Blanco, F.; Ramírez-Alvarado, M.; Serrano, L. Formation and Stability of β-Hairpin Structures in Polypeptides. *Curr. Opin. Struct. Biol.* **1998**, *8* (1), 107-111. https://doi.org/10.1016/S0959-440X(98)80017-1.

(98) Baltzer, L. Functionalization of Designed Folded Polypeptides. *Curr. Opin. Struct. Biol.* **1998**, *8* (4), 466-470. https://doi.org/10.1016/S0959-440X(98)80124-3.

(99) Hill, R. B.; Raleigh, D. P.; Lombardi, A.; Degrado, W. F. De Novo Design of Helical Bundles as Models for Understanding Protein Folding and Function. *Acc. Chem. Res.* **2000**, *33* (11), 745-754. https://doi.org/10.1021/ar970004h.

(100) Kaplan, J.; DeGrado, W. F. De Novo Design of Catalytic Proteins. *Proc. Natl. Acad. Sci. U. S. A.* **2004**, *101* (32), 11566-11570. https://doi.org/10.1073/pnas.0404387101.

(101) Baltzer, L.; Nilsson, H.; Nilsson, J. De Novo Design of Proteins - What Are the Rules? *Chemical Reviews*. **2001**, *101* (10), 3153-3163. https://doi.org/10.1021/cr0000473.

(102) Bryson, J. W.; Betz, S. F.; Lu, H. S.; Suich, D. J.; Zhou, H. X.; O'Neil, K. T.; DeGrado, W. F. Protein Design: A Hierarchic Approach. *Science.* **1995**, *270* (5238), 935-941. https://doi.org/10.1126/science.270.5238.935.

(103) DeGrado, W. F.; Wasserman, Z. R.; Lear, J. D. Protein Design, a Minimalist Approach. *Science*. **1989**, *243* (4891), 622-628. https://doi.org/10.1126/science.2464850.

(104) Boyle, A. L.; Woolfson, D. N. De Novo Designed Peptides for Biological Applications. *Chemical Society Reviews*. **2011**, *40* (8), 4295-4306. https://doi.org/10.1039/c0cs00152j.

(105) Grayson, K. J.; Anderson, J. L. R. Designed for Life: Biocompatible de Novo Designed Proteins and Components. *Journal of the Royal Society Interface*. **2018**, *15* (145). https://doi.org/10.1098/rsif.2018.0472.

(106) Regan, L.; Degrado, W. F. Characterization of a Helical Protein Designed from First Principles. *Science.* **1988**, *241* (4868), 976-978. https://doi.org/10.1126/science.3043666.

(107) Raleigh, D. P.; DeGrado, W. F. A de Novo Designed Protein Shows a Thermally Induced Transition from a Native to a Molten Globule-like State. *Journal of the American Chemical Society*. **1992**, *114* (25), 10079-10081. https://doi.org/10.1021/ja00051a061.

(108) Blake Hill, R.; Degrado, W. F. Solution Structure of α_2D, a Nativelike de Novo Designed Protein. *J. Am. Chem. Soc.* **1998**, *120* (6), 1138-1145. https://doi.org/10.1021/ja9733649.

(109) Hill, R. B.; DeGrado, W. F. A Polar, Solvent-Exposed Residue Can Be Essential for Native Protein Structure. *Structure* **2000**, *8* (5), 471-479. https://doi.org/10.1016/S0969-2126(00)00130-1.

(110) Hill, R. B.; Bracken, C.; Degrado, W. F.; Palmer, A. G. Molecular Motions and Protein Folding: Characterization of the Backbone Dynamics and Folding Equilibrium of α 2_{α}D Using 13 C NMR Spin Relaxation. *J. Am. Chem. Soc.* **2000**, *122* (47), 11610-11619. https://doi.org/10.1021/ja001129b.

(111) Ho, S. P.; DeGrado, W. F. Design of a 4-Helix Bundle Protein: Synthesis of Peptides Which Self-Associate into a Helical Protein. *J. Am. Chem. Soc.* **1987**, *109* (22), 6751-6758. https://doi.org/10.1021/ja00256a032.

(112) Walsh, S. T. R.; Cheng, H.; Bryson, J. W.; Roder, H.; Degrado, W. F. Solution Structure and Dynamics of a de Novo Designed Three-Helix Bundle Protein. *Proc. Natl. Acad. Sci. U. S. A.* **1999**, 96 (10) 5489-5491. https://doi.org/10.1073/pnas.96.10.5486.

(113) Bryson, J. W.; Desjarlais, J. R.; Handel, T. M.; DeGrado, W. F. From Coiled Coils to Small Globular Proteins: Design of a Native-like Three-Helix Bundle. *Protein Sci.* **1998**, *7* (6), 1404-1414. https://doi.org/10.1002/pro.5560070617.

(114) Johansson, J. S.; Gibney, B. R.; Skalicky, J. J.; Wand, A. J.; Dutton, P. L. A Native-like Three-α-Helix Bundle Protein from Structure-Based Redesign: A Novel Maquette Scaffold. *J. Am. Chem. Soc.* **1998**, *120* (16), 3881-3886. https://doi.org/10.1021/ja973538m.

(115) Tebo, A. G.; Pecoraro, V. L. Artificial Metalloenzymes Derived from Three-Helix Bundles. *Current Opinion in Chemical Biology*. **2015**, *25*, 65-70. https://doi.org/10.1016/j.cbpa.2014.12.034.

(116) Cangelosi, V. M.; Deb, A.; Penner-Hahn, J. E.; Pecoraro, V. L. A de Novo Designed Metalloenzyme for the Hydration of CO_2. *Angew. Chemie - Int. Ed.* **2014**, *53* (30), 7900-7903. https://doi.org/10.1002/anie.201404925.

(117) Manuscript, A. Realization of a Designed Three-Helix Bundle Capable of Binding Heavy Metals. **2012**, *50* (9), 2049–2053. https://doi.org/10.1002/anie.201006413.Realization.

(118) Plegaria, J. S.; Dzul, S. P.; Zuiderweg, E. R. P.; Stemmler, T. L.; Pecoraro, V. L. Apoprotein Structure and Metal Binding Characterization of a de Novo Designed Peptide, α_3DIV, That Sequesters Toxic Heavy Metals. *Biochemistry* **2015**, *54* (18), 2858-2873. https://doi.org/10.1021/acs.biochem.5b00064.

(119) Chakraborty, S.; Yudenfreundkravitz, J.; Thulstrup, P. W.; Hemmingsen, L.; Degrado, W. F.; Pecoraro, V. L. Design of a Three-Helix Bundle Capable of Binding Heavy Metals in a Triscysteine Environment. *Angew. Chemie - Int. Ed.* **2011**, *50* (9), 2049-2053. https://doi.org/10.1002/anie.201006413.

(120) Lunt, M. W.; Snow, C. D. Computational Design of Ligand Binding Proteins. *Methods Mol. Biol.* **2016**, *1414*, 375 pp. https://doi.org/10.1007/978-1-4939-3569-7.

(121) Lu, Y.; Valentine, J. S. Engineering Metal-Binding Sites in Proteins. *Curr. Opin. Struct. Biol.* **1997**, *7* (4), 49-500. https://doi.org/10.1016/S0959-440X(97)80112-1.

(122) Perrin, B. S.; Ichiye, T. Characterizing the Effects of the Protein Environment on the Reduction Potentials of Metalloproteins. *J. Biol. Inorg. Chem.* **2013**, *18* (1), 103-110.

https://doi.org/10.1007/s00775-012-0955-3.

(123) Nanda, V.; Rosenblatt, M. M.; Osyczka, A.; Kono, H.; Getahun, Z.; Dutton, P. L.; Saven, J. G.; DeGrado, W. F. De Novo Design of a Redox-Active Minimal Rubredoxin Mimic. *J. Am. Chem. Soc.* **2005**, *127* (16), 5804-5805. https://doi.org/10.1021/ja050553f.

(124) Tebo, A. G.; Pinter, T. B. J.; García-Serres, R.; Speelman, A. L.; Tard, C.; Sénéque, O.; Blondin, G.; Latour, J. M.; Penner-Hahn, J.; Lehnert, N.; et al. Development of a Rubredoxin-Type Center Embedded in a de Dovo -Designed Three-Helix Bundle. *Biochemistry* **2018**, *57* (16), 2308-2316. https://doi.org/10.1021/acs.biochem.8b00091.

(125) Tebo, A. G.; Hemmingsen, L.; Pecoraro, V. L. Variable Primary Coordination Environments of Cd(II) Binding to Three Helix Bundles Provide a Pathway for Rapid Metal Exchange. *Metallomics* **2015**, *7* (12), 1555-1561. https://doi.org/10.1039/c5mt00228a.

(126) LOWRY, O. H.; ROSEBROUGH, N. J.; FARR, A. L.; RANDALL, R. J. Protein Measurement with the Folin Phenol Reagent. *J. Biol. Chem.* **1951**, *193* (1), 265-75.

(127) Kelly, S. M.; Jess, T. J.; Price, N. C. How to Study Proteins by Circular Dichroism. *Biochimica et Biophysica Acta - Proteins and Proteomics*. **2005**, *1751* (2), 119-139. https://doi.org/10.1016/j.bbapap.2005.06.005.

(128) Whitmore, L.; Wallace, B. A. Protein Secondary Structure Analyses from Circular Dichroism Spectroscopy: Methods and Reference Databases. *Biopolymers* **2008**, *89* (5), 392-400. https://doi.org/10.1002/bip.20853.

(129) Kelly, S.; Price, N. The Use of Circular Dichroism in the Investigation of Protein Structure and Function. *Curr. Protein Pept. Sci.* **2005**, *1* (4), 349-384. https://doi.org/10.2174/1389203003381315.

(130) Greenfield, N. J. Using Circular Dichroism Spectra to Estimate Protein Secondary Structure. *Nat. Protoc.* **2007**, *1* (6), 2876-2890. https://doi.org/10.1038/nprot.2006.202.

(131) Greenfield, N. J. Using Circular Dichroism Collected as a Function of Temperature to Determine the Thermodynamics of Protein Unfolding and Binding Interactions. *Nat. Protoc.* **2007**, *1* (6), 2527-2535. https://doi.org/10.1038/nprot.2006.204.

(132) Woody, R. W.; Dunker, A. K. Aromatic and Cystine Side-Chain Circular Dichroism in Proteins. In *Circular Dichroism and the Conformational Analysis of Biomolecules*; **1996**, *Chaper 4*, 109-157. https://doi.org/10.1007/978-1-4757-2508-7_4.

(133) Greenfield, N. J. Applications of Circular Dichroism in Protein and Peptide Analysis. *TrAC - Trends Anal. Chem.* **1999**, *18* (4), 236-244. https://doi.org/10.1016/S0165-9936(98)00112-5.

(134) Pessoa, J. C.; Correia, I.; Gonçalves, G.; Tomaz, I. Circular Dichroism in Coordination Compounds. *J. Argentine Chem. Soc.* **2009**, *97* (1), 151-165.

(135) Chiu, M.; Prenner, E. Differential Scanning Calorimetry: An Invaluable Tool for a Detailed Thermodynamic Characterization of Macromolecules and Their Interactions. In *Journal of Pharmacy and Bioallied Sciences*; **2011**, *3* (1), 39-59. https://doi.org/10.4103/0975-7406.76463.

(136) Garbett, N. C.; Brock, G. N. Differential Scanning Calorimetry as a Complementary Diagnostic Tool for the Evaluation of Biological Samples. *Biochim. Biophys. Acta - Gen. Subj.* **2016**, *1860* (5), 981-989. https://doi.org/10.1016/j.bbagen.2015.10.004.

(137) Eftink, M. R. Use of Multiple Spectroscopic Methods to Monitor Equilibrium Unfolding of Proteins. *Methods Enzymol.* **1995**, *259*, 487-512. https://doi.org/10.1016/0076-6879(95)59058-7.

(138) Johnson, C. M. Differential Scanning Calorimetry as a Tool for Protein Folding and Stability. *Archives of Biochemistry and Biophysics*. **2013**, *531* (1-2), 100-9. https://doi.org/10.1016/j.abb.2012.09.008.

(139) Saboury, A.; Moosavi-Movahedi, A. Clarification of Calorimetric and van 't Hoff Enthalpies for Evaluation of Protein Transition States. *Biochem. Educ.* **1994**, *22* (4), 210-211. https://doi.org/10.1016/0307-4412(94)90013-2.

(140) Lawendel, J. S. Ultra-Violet Absorption Spectra of L-Asorbic Acid in Aqueous Solutions [6]. *Nature*. **1957**, *180*, 434-435. https://doi.org/10.1038/180434a0.

(141) Anderson, L. B.; Reilley, C. N. Thin-Layer Electrochemistry: Steady-State Methods of Studying Rate Processes. *J. Electroanal. Chem.* **1965**, *10* (4), 295-305. https://doi.org/10.1016/0022-0728(65)85063-X

(142) Teixeira, L. R.; Dantas, J. M.; Salgueiro, C. A.; Cordas, C. M. Thermodynamic and Kinetic Properties of the Outer Membrane Cytochrome OmcF, a Key Protein for Extracellular Electron Transfer in *Geobacter Sulfurreducens*. *Biochim. Biophys. Acta - Bioenerg.* **2018**, *1859* (10), 1132-1137. https://doi.org/10.1016/j.bbabio.2018.07.007.

(143) Ramos, S.; Almeida, R. M.; Cordas, C. M.; Moura, J. J. G.; Pauleta, S. R.; Moura, I. Insights into the Recognition and Electron Transfer Steps in Nitric Oxide Reductase from *Marinobacter Hydrocarbonoclasticus*. *J. Inorg. Biochem.* **2017**, *177,* 402-411. https://doi.org/10.1016/j.jinorgbio.2017.09.001.

(144) Léger, C.; Bertrand, P. Direct Electrochemistry of Redox Enzymes as a Tool for Mechanistic Studies. *Chemical Reviews*. **2008**, *108* (7), 2379-2438. https://doi.org/10.1021/cr0680742.

(145) Cordas, C. M.; Campaniço, M.; Baptista, R.; Maia, L. B.; Moura, I.; Moura, J. J. G. Direct Electrochemical Reduction of Carbon Dioxide by a Molybdenum-Containing Formate Dehydrogenase. *J. Inorg. Biochem.* **2019**, *196*, 110694. https://doi.org/10.1016/j.jinorgbio.2019.110694.

(146) Waterhouse, A.; Bertoni, M.; Bienert, S.; Studer, G.; Tauriello, G.; Gumienny, R.; Heer, F. T.; De Beer, T. A. P.; Rempfer, C.; Bordoli, L.; et al. SWISS-MODEL: Homology Modelling of Protein Structures and Complexes. *Nucleic Acids Res.* **2018**, *46* (W1), W296-W303. https://doi.org/10.1093/nar/gky427.

(147) Benkert, P.; Biasini, M.; Schwede, T. Toward the Estimation of the Absolute Quality of Individual Protein Structure Models. *Bioinformatics* **2011**, *27* (3), 343-350. https://doi.org/10.1093/bioinformatics/btq662.

(148) Chen, C. J.; Lin, Y. H.; Huang, Y. C.; Liu, M. Y. Crystal Structure of Rubredoxin from *Desulfovibrio Gigas* to Ultra-High 0.68 Å Resolution. *Biochem. Biophys. Res. Commun.* **2006**, *349* (1), 79-90. https://doi.org/10.1016/j.bbrc.2006.07.205.

(149) Akmal, A.; Muñoz, V. The Nature of the Free Energy Barriers to Two-State Folding. *Proteins Struct. Funct. Genet.* **2004**, *57* (1), 142-152. https://doi.org/10.1002/prot.20172.

(150) Naganathan, A. N.; Doshi, U.; Muñoz, V. Protein Folding Kinetics: Barrier Effects in Chemical and Thermal Denaturation Experiments. *J. Am. Chem. Soc.* **2007**, *129* (17), 5673-5682. https://doi.org/10.1021/ja0689740.

(151) Kuppuraj, G.; Dudev, M.; Lim, C. Factors Governing Metal-Ligand Distances and Coordination Geometries of Metal Complexes. *J. Phys. Chem. B* **2009**, *113* (9), 2952-2960. https://doi.org/10.1021/jp807972e.

(152) Ohtaki, H.; Radnai, T. Structure and Dynamics of Hydrated Ions. *Chem. Rev.* **1993**, *112* (49), 15801-15806. https://doi.org/10.1021/cr00019a014.

(153) Elia, M. Artificial Metalloproteins as Models for Molybdoenzymes, Master's Thesis, Alma Mater

Studiorum Università di Bologna Scuola di Farmacia, Biotecnologie e Scienze Motorie, **2018**.

(154) Strickland, E. H.; Beychok, S. Aromatic Contributions to Circular Dichroism Spectra of Protein. *Crit. Rev. Biochem. Mol. Biol.* **1974**, *2* (1), 113-175. https://doi.org/10.3109/10409237409105445.

(155) Förster, T. Electronic Absorption Spectra and Geometry of Organic Molecules. *Zeitschrift für Phys. Chemie* **1970**. https://doi.org/10.1524/zpch.1970.72.1_3.167a.

(156) SUZUKI, H. Chapter 6 - Effect of Environment upon Electronic Absorption Spectra. In *Electronic Absorption Spectra and Geometry of Organic Molecules*; SUZUKI, H., Ed.; Academic Press, **1967**; pp 93–118. https://doi.org/https://doi.org/10.1016/B978-0-12-395557-9.50009-4.

(157) Perrin, J. H.; Hart, P. A. Small Molecule-macromolecule Interactions as Studied by Optical Rotatory Dispersion-circular Dichroism. *Journal of Pharmaceutical Sciences*. **1970**, *59* (4), 431-448. https://doi.org/10.1002/jps.2600590402.

(158) Bonomi, F.; Iametti, S.; Mazzini, S.; Fessas, D.; Kurtz, D. M. Thermal Stability of *Clostridium Pasteurianum* Rubredoxin: Deconvoluting the Contributions of the Metal Site and the Protein. *Protein Sci.* **2000**, *9* (12), 2413-2426. https://doi.org/10.1110/ps.9.12.2413.

(159) Bonomi, F.; Burden, A. E.; Eidsness, M. K.; Fessas, D.; Iametti, S.; Kurtz, D. M.; Mazzini, S.; Scott, R. A.; Zeng, Q. Thermal Stability of the [Fe(SCys)4] Site in *Clostridium Pastearianum* Rubredoxin: Contributions of the Local Environment and Cys Ligand Protonation. *J. Biol. Inorg. Chem.* **2002**, *7* (4-5), 427-436. https://doi.org/10.1007/s00775-001-0314-2.

(160) Bruylants, G.; Wouters, J.; Michaux, C. Differential Scanning Calorimetry in Life Science: Thermodynamics, Stability, Molecular Recognition and Application in Drug Design. *Curr. Med. Chem.* **2005**, *12* (17), 2011-2020. https://doi.org/10.2174/0929867054546564.

(161) Ibarra-Molero, B.; Naganathan, A. N.; Sanchez-Ruiz, J. M.; Muñoz, V. Modern Analysis of Protein Folding by Differential Scanning Calorimetry. In *Methods in Enzymology*; **2016**, *597*, 281-318. https://doi.org/10.1016/bs.mie.2015.08.027.

(162) Han, J. C.; Han, G. Y. A Procedure for Quantitative Determination of Tris(2-Carboxyethyl)Phosphine, an Odorless Reducing Agent More Stable and Effective than Dithiothreitol. *Anal. Biochem.* **1994**, *220* (1), 5-10. https://doi.org/10.1006/abio.1994.1290.

(163) Bray, R. C.; Adams, B.; Smith, A. T.; Bennett, B.; Bailey, S. Reversible Dissociation of Thiolate Ligands from Molybdenum in an Enzyme of the Dimethyl Sulfoxide Reductase Family. *Biochemistry* **2000**, *39* (37), 11258-11269. https://doi.org/10.1021/bi0000521.

(164) Klein, E. L.; Raitsimring, A. M.; Astashkin, A. V.; Rajapakshe, A.; Johnson-Winters, K.; Arnold, A. R.; Potapov, A.; Goldfarb, D.; Enemark, J. H. Identity of the Exchangeable Sulfur-Containing Ligand at the Mo(V) Center of R160Q Human Sulfite Oxidase. *Inorg. Chem.* **2012**, *51* (3), 1408-1418. https://doi.org/10.1021/ic201643t.

(165) O'Neil, M. J. The Merck Index: An Encyclopedia of Chemicals, Drugs, and Biologicals. 13th Edition. *Drug Dev. Res.* **2006**. https://doi.org/10.1002/ddr.20159.

(166) MAYHEW, S. G. The Redox Potential of Dithionite and SO^{-2} from Equilibrium Reactions with Flavodoxins, Methyl Viologen and Hydrogen plus Hydrogenase. *Eur. J. Biochem.* **1978**, *85* (2), 535-547. https://doi.org/10.1111/j.1432-1033.1978.tb12269.x.

(167) Warren, J. J.; Mayer, J. M. Tuning of the Thermochemical and Kinetic Properties of Ascorbate by Its Local Environment: Solution Chemistry and Biochemical Implications. *J. Am. Chem. Soc.* **2010**, *132* (22), 7784-7793. https://doi.org/10.1021/ja102337n.

(168) Arnoux, P.; Sabaty, M.; Alric, J.; Frangioni, B.; Guigliarelli, B.; Adriano, J. M.; Pignol, D. Structural

and Redox Plasticity in the Heterodimeric Periplasmic Nitrate Reductase. *Nat. Struct. Biol.* **2003**, *10*, 928-934. https://doi.org/10.1038/nsb994.

(169) Jepson, B. J. N.; Mohan, S.; Clarke, T. A.; Gates, A. J.; Cole, J. A.; Butler, C. S.; Butt, J. N.; Hemmings, A. M.; Richardson, D. J. Spectropotentiometric and Structural Analysis of the Periplasmic Nitrate Reductase from *Escherichia Coli*. *J. Biol. Chem.* **2007**, *282* (9), 6425-6437. https://doi.org/10.1074/jbc.M607353200.

(170) Cammack, R.; Barber, M. J.; Bray, R. C. Oxidation Reduction Potentials of Molybdenum, Flavin and Iron Sulphur Centres in Milk Xanthine Oxidase. *Biochem. J.* **1976**, *157* (2), 469-478. https://doi.org/10.1042/bj1570469.

(171) Moura, J. J. G.; Xavier, A. V.; Cammack, R.; Hall, D. O.; Bruschi, M.; Le Gall, J. Oxidation Reduction Studies of the Mo-(2Fe-2S) Protein from *Desulfovibrio Gigas*. *Biochem. J.* **1978**, *173* (2), 419-425. https://doi.org/10.1042/bj1730419.

(172) Muhammad, H.; Tahiri, I. A.; Muhammad, M.; Masood, Z.; Versiani, M. A.; Khaliq, O.; Latif, M.; Hanif, M. A Comprehensive Heterogeneous Electron Transfer Rate Constant Evaluation of Dissolved Oxygen in DMSO at Glassy Carbon Electrode Measured by Different Electrochemical Methods. *J. Electroanal. Chem.* **2016**, *775,* 157-162. https://doi.org/10.1016/j.jelechem.2016.05.049.

(173) Elliott, S. J.; Hoke, K. R.; Heffron, K.; Palak, M.; Rothery, R. A.; Weiner, J. H.; Armstrong, F. A. Voltammetric Studies of the Catalytic Mechanism of the Respiratory Nitrate Reductase from Escherichia Coli: How Nitrate Reduction and Inhibition Depend on the Oxidation State of the Active Site. *Biochemistry* **2004**, *43* (3), 799-807. https://doi.org/10.1021/bi035869j.

(174) Brondino, C. D.; Rivas, M. G.; Romão, M. J.; Moura, J. J. G.; Moura, I. Structural and Electron Paramagnetic Resonance (EPR) Studies of Mononuclear Molybdenum Enzymes from Sulfate-Reducing Bacteria. *Acc. Chem. Res.* **2006**, *39* (10), 788-796. https://doi.org/10.1021/ar050104k.

(175) Izumi, Y.; Glaser, T.; Rose, K.; McMaster, J.; Basu, P.; Enemark, J. H.; Hedman, B.; Hodgson, K. O.; Solomon, E. I. Ligand K-Edge and Metal L-Edge X-Ray Absorption Spectroscopy and Density Functional Calculations of Oxomolybdenum Complexes with Thiolate and Related Ligands: Implications for Sulfite Oxidase. *J. Am. Chem. Soc.* **1999**, *121* (43), 10035-10046. https://doi.org/10.1021/ja9903678.

(176) Garton, S. D.; Garrett, R. M.; Rajagopalan, K. V.; Johnson, M. K. Resonance Raman Characterization of the Molybdenum Center in Sulfite Oxidase: Identification of Mo=O Stretching Modes. *J. Am. Chem. Soc.* **1997**, *119* (10), 2590-2591. https://doi.org/10.1021/ja963931c.

(177) Caradonna, J. P.; Harlan, E. W.; Holm, R. H. Thiol as an Electron Donor in Molybdenum Oxo-Transferase Analogue Reaction Systems: Observations by 19F NMR Spectroscopy and Biological Implications. *J. Am. Chem. Soc.* **1986**, *108* (24), 7856-7858. https://doi.org/10.1021/ja00284a073.